

CRYOGENIC TWO-PHASE FLOW AND PHASE-CHANGE HEAT TRANSFER IN
MICROGRAVITY

By

CHENG-FENG TAI

A DISSERTATION PRESENTED TO THE GRADUATE SCHOOL
OF THE UNIVERSITY OF FLORIDA IN PARTIAL FULFILLMENT
OF THE REQUIREMENTS FOR THE DEGREE OF
DOCTOR OF PHILOSOPHY

UNIVERSITY OF FLORIDA

2008

© 2008 Cheng-Feng Tai

To my wife Xiaoling, daughter Grace and my parents.

ACKNOWLEDGMENTS

I would like to express my sincere gratitude to Dr. Jacob Nan-Chu Chung for providing me the opportunity to perform this research. I can not thank him enough for being so patient and understanding for years, imparting me a lot of knowledge and giving me the best advice.

I would like to thank Drs. S. Balachandar, W. E. Lear Jr., S. A. Sherif, and G. Ihas for agreeing to serve on my dissertation committee. I thank my research group members for helping with academic aspects while providing memorable company for the past years.

Finally I thank my family members who have been behind me every step of the way providing their unconditional support.

TABLE OF CONTENTS

	<u>page</u>
ACKNOWLEDGMENTS	4
LIST OF TABLES	8
LIST OF FIGURES	9
ABSTRACT.....	15
CHAPTER	
1 INTRODUCTION	17
1.1 Overview.....	17
1.2 Role of Cryogenics in Space Exploration.....	17
1.3 All Cryogenic Systems Must Be Chilled Down.....	18
1.4 Background of a Chardown Process.....	19
1.5 Objectives of the Research	19
1.6 Scope and Structure	20
2 PHYSICAL BACKGROUND AND LITERATURE REVIEW.....	22
2.1 Boiling Curve and Chardown Process.....	22
2.2 Two-Phase Flow Patterns and Heat Transfer Regimes	22
2.3 Two-Phase Flow in Microgravity	24
2.3.1 Isothermal Two-Phase Flows in Microgravity	24
2.3.2 Two-Phase Flow and Heat Transfer in Microgravity.....	25
3 PROBLEM DEFINITION AND GOVERNING EQUATIONS	29
3.1 Modeling Cryogenic Chardown in Microgravity	29
3.2 Geometry, Computational Domain and Initial, Boundary Conditions	30
3.3 Assumptions	31
3.4 Governing Equations	32
3.4.1 Interfacial Conditions	33
3.4.2 Non-dimensionalization	34
4 SOLUTION METHOD	40
4.1 Introduction.....	40
4.2 Fractional Step Method within the Finite Volume Framework.....	41
4.3 Cartesian Grid Method for a Complex Geometry	44
4.4 Sharp Interface Method with Cut-Cell Approach (SIMCC).....	46
4.4.1 Interfacial Tracking	47
4.4.2 Merging Procedure	48

4.4.3 Flux and Stress Computations in the Interfacial Region	49
4.4.4 Moving Interface Algorithm.....	51
4.4.4.1 Advancing the Interface	51
4.4.4.2 Updating the Cells.....	53
4.5 Issues of Phase Change Computation in Cartesian Grid Methods	53
4.6 Heat Flux Computation at the Interface.....	56
4.7 Phase Change Algorithm.....	58
4.8 Global Conservation of Mass	62
5 VALIDATION OF CODE	73
5.1 Introduction.....	73
5.2 Group 1, Solver of Governing Equations and the SIMCC with the Fixed Interface.....	73
5.2.1 The Fictitious Interface for Evaluating the SIMCC	73
5.2.2 Couette Flow, Fully Developed Channel Flow and Cavity Flow	76
5.2.2.1 The Couette Flow	77
5.2.2.2 The Fully Developed Channel Flow	77
5.2.2.3 The Cavity Flow.....	78
5.2.3 The Fully Developed Pipe Flow with a Constant Wall Heat Flux	79
5.2.4 Flow over a Sphere with Heat Transfer.....	80
5.3 Group 2, Validation for Moving Interface Algorithm.....	81
5.3.1 Static Droplet Simulation	82
5.3.2 Deformed Rising Bubble and Droplet.....	83
5.4 Group 3, Validation for Accurate Mass Transfer at the Interface	85
5.4.1 A Stationary Droplet in a Quiescent Environment with a Constant Mass Transfer Rate.....	85
5.4.2 One Dimensional Phase Change Problem.....	87
5.5 Summary.....	89
6 LIQUID-GAS TWO-PHASE FLOWS IN A PIPE WITHOUT PHASE CHANGE	102
6.1 Introduction.....	102
6.2 Isothermal Liquid-Gas Two-Phase Flows in a Pipe	103
6.2.1 Effect of the Reynolds Number.....	104
6.2.2 Effect of the Weber Number	108
6.2.3 Two-Phase Flow Pressure Drop	111
6.3 Grid Refinement Study	111
6.4 Liquid-Gas Two-Phase Flows in a Pipe with Heat Transfer	112
6.4.1 Low Surface Tension Case.....	113
6.4.2 High Surface Tension Case	116
6.5 Summary.....	118
7 LIQUID-GAS TWO-PHASE FLOWS IN A PIPE WITH PHASE CHANGE	131
7.1 Introduction.....	131
7.2 R-508B Refrigerant with Constant Wall Temperature.....	132
7.3 Constant Wall Temperature Case with Liquid Nitrogen	134

7.3.1 Flow Field with the Constant Wall Temperature Case	135
7.3.2 The Mass Transfer at Interface with Constant Wall Temperature	138
7.3.3 The Transient Phase Change Process with Constant Wall Temperature	139
7.3.4 The Comparison of Nusselt Number with Phase Change Process and Constant Wall Temperature	140
7.4 Wall Chillover Process by Liquid Nitrogen.....	142
7.4.1 Flow Patterns during Chillover Process	142
7.4.2 The Wall and Liquid-Gas Interface Conditions during Chillover Process.....	142
7.4.3 The Time-Dependent Development during Chillover Process.....	144
7.5 Wall Chillover Process by Liquid Hydrogen.....	144
7.6 Summary.....	147
8 SUMMARY AND FUTURE WORK.....	165
8.1 Summary.....	165
8.2 Future Work.....	165
LIST OF REFERENCES.....	167
BIOGRAPHICAL SKETCH	175

LIST OF TABLES

<u>Table</u>		<u>page</u>
4-1	Comparison of the key issues for different numerical methods for the heat flux computation.....	65
4-2	Comparison of exact and numerical results for the flow over sphere case.....	65
5-1	The error of Nusselt number by different grid resolutions in flow over a sphere case.....	90
5-2	The fluid properties of liquid and gas phases for the one dimensional phase change problem.	90
7-1	Dimensionless parameters for the nitrogen case with constant wall temperature.	149
7-2	The maximum velocity for the nitrogen case with wall chilldown and the reference cases at time=1.5.	149
7-3	The mass flow rate for the nitrogen case with wall chilldown and the reference cases at time=1.5.	149

LIST OF FIGURES

<u>Figure</u>	<u>page</u>
2-1 Typical boiling curve.....	27
2-2 Flow regimes and heat transfer regimes in a heated channel.....	27
2-3 Flow regimes under microgravity.....	27
2-4 Effect of the gravity on flow regimes.....	28
3-1 A simple cryogenic system.....	38
3-2 Inverted annular flow.....	38
3-3 Idealized inverted annular flow.....	38
3-4 Conjugate heat transfer.....	38
3-5 The initial shape of liquid core.....	39
4-1 Non-staggered grid system.....	65
4-2 Example of mixed structured and unstructured grid in SIMCC.....	65
4-3 Example of mixed structured and unstructured grid.....	66
4-4 Marker points of an oblique ellipse.....	66
4-5 Intersection points of an oblique ellipse.....	66
4-6 Illustration of the interfacial cells and cut-and-absorption procedures in the SIMCC in local situation.....	67
4-7 Cut-cells of different objects.....	67
4-8 Example of cut-cells of different grids.....	67
4-9 Illustration of the interfacial variables and notation.....	68
4-10 Illustration of interfacial advancing process.....	68
4-11 Illustration of updating cell procedure.....	68
4-12 Two probing points for second order gradient.....	69
4-13 Illustration of geometry of test domain.....	69

4-14	The assumptive temperature distribution.....	69
4-15	The new interface because of phase change.	70
4-16	The new interface because of balance of force.	70
4-17	The flow chart for the phase change algorithm.	71
4-18	The global conservation of mass in gas phase.....	71
4-19	Interim interface construction, the initial interface.....	72
4-20	Interim interface construction, the new interface.	72
4-21	Re-structuring of markers, the original makers.	72
4-22	Re-structuring of markers, the new markers.....	72
5-1	The continuous stress condition at marker points for the fictitious interface.....	90
5-2	The algorithm for second order gradient.	90
5-3	Eight points method for second order gradient of velocity.....	91
5-4	Geometry of the Couette flow, cavity flow and fully developed channel with the immersed fictitious interface.....	91
5-5	Error in interfacial velocity at all the interfacial marker points (163 points) and error in mass and momentum fluxes of each cut-cell (148 cut-cells) in the Couette flow with radius of fictitious interface $R=0.1$	92
5-6	Pressure contour, U velocity profile, and error in mass and momentum fluxes of each cut-cell (92 cut-cells) of fully developed channel flow with radius of fictitious interface $R=0.05$ and $Re=100$	93
5-7	Streamline plots and U velocity profile at $R=0.5$ with different fictitious interface radii of cavity flow with $Re=100$	94
5-8	The temperature distribution of fully developed pipe flow with constant heat flux case.....	94
5-9	The heat flux at wall of fully developed pipe flow with constant heat flux case.	95
5-10	The temperature profile of fully developed pipe flow with constant heat flux case at $X=0.481235$ along radial direction.	95
5-11	The temperature distributions of fully developed pipe flow with constant heat flux case with different fictitious interfaces.	95

5-12	The temperature profile of fully developed pipe flow with constant heat flux case with a fictitious interface ($R=0.3$) at $X=0.481235$ along radial direction.....	96
5-13	Grid and geometry of flow over a sphere with heat transfer.	96
5-14	The pressure contour, the stream line and temperature contour of flow over a sphere with $Re=1$, $Pe=1$	96
5-15	Schematic of stationary droplet problem.	97
5-16	The maximum induced interfacial velocity of stationary droplet problem.....	97
5-17	Convergent histories of the interfacial condition and the governing equations of stationary droplet problem.	97
5-18	Pressure contour for the stationary droplet.	98
5-19	The shape and streamline plot for a bubble with $Re=10$ and $We=8$	98
5-20	The aspect ratio plot for a bubble with $Re=10.0$ and $We= 2.0-8.0$	98
5-21	The streamline and shape plot for a droplet with $Re=10$ and $We=2$	99
5-22	Geometry of static droplet with a constant mass transfer rate problem.....	99
5-23	Velocity distribution of static droplet with a constant mass transfer rate problem along radial direction at $X=5$	100
5-24	Streamline plot near the interface of static droplet with a constant mass transfer rate problem.	100
5-25	Illustration of one dimensional phase change problem.....	100
5-26	The location of interface and temperature distribution, contour for one dimensional phase change problem.....	101
6-1	Streamline of the isothermal case at time=6.0 with $Re= 2000$ and $We=500$	120
6-2	The pressure contours/distributions at time=6.0 with $Re=2000$ and $We=500$	120
6-2	Continued.....	121
6-3	The pressure distributions along the centerline based on different Reynolds numbers at time=6.0.	122
6-4	The U velocity profile at time=6.0 with $Re=2000$ and $We=500$	122
6-5	Shapes of liquid cores with different Reynolds numbers at time=6.0.	122

6-6	The pressure contours at time=6.0 with Re=500 and We= 2.63.....	123
6-7	Pressure distribution and the curvature of interface at time=6.0 with Re=500 and We=2.63.....	123
6-8	Streamline plot at time=6.0 with Re=500 and We=2.63.	124
6-9	U velocity profile at time=6.0 with Re=500 and We=2.63.	124
6-10	Shapes of the interface by different Weber numbers at time=6.0.....	124
6-11	The development of interface with Re=500 and We=2.63 at different time steps.	125
6-12	The ratio of averaged local friction coefficient in the two-phase zone to the fully developed single-phase gas flow friction coefficient.....	125
6-13	The computed interfaces by three different grid resolutions.	125
6-14	The pressure contours, pressure and curvature distribution, streamline plot and the contour of U component contour of the case with Re=500, Pe=6500 and We=500 at time=5.5.	126
6-15	The temperature contours of two-phase plug flow and the interfacial temperature at different time steps with Re=500, Pe=6500 and We=500.....	127
6-16	The Nusselt number at the solid wall at different time steps with Re=500, Pe=6500 and We=500.....	127
6-17	The comparison of interfacial temperature and Nusselt number at wall for different Reynolds number with Pe=6500 and We=500 at time=5.5.....	128
6-18	The shapes of the liquid slug at three different time steps for the case of Re=500, Pe=6500 and We=2.63.....	128
6-19	The temperature contour of two phase plug flow and the interfacial temperature with Re=500, Pe=6500 and We=2.63at different time steps.	129
6-20	The Nusselt number at the solid wall Re=500, Pe=6500 and We=2.63 at different time steps.	129
7-1	The U contours for the refrigerant R-508B case at different time steps.....	149
7-2	The local maximum U in the gas phase for the refrigerant R-508B case at different time steps.	150
7-3	The interfaces for the refrigerant R-508B case at different time steps.....	150
7-4	The streamlines in the gas phase for the refrigerant R-508B case at time=4.0	151

7-5	The V contours for refrigerant R-508B case at different time steps.....	151
7-6	The temperature contours for refrigerant R-508B case at different time steps.....	152
7-7	The Nusselt numbers along solid wall for the refrigerant R-508B case at different time steps.	152
7-8	The total mass flow rate of gas phase for the refrigerant R-508B case at different time steps.	153
7-9	The vector and the streamline plots for Case 2 in the nitrogen case with constant wall temperature at time=1.5.	153
7-10	The U contours for the nitrogen case with constant wall temperature at time=1.5.	154
7-11	The V contours for nitrogen case with constant wall temperature at time=1.5.	155
7-12	Maximum velocity for the nitrogen case with constant wall temperature of three cases.	155
7-13	The temperature contours for nitrogen case with constant wall temperature at time=1.5.	156
7-14	The interfaces of three cases for the nitrogen case with constant wall temperature at time=1.5.	156
7-15	The interfaces of three different grid lengths.....	157
7-16	The temperature gradient of three cases along the interface at time=1.5 and the locations of markers for the nitrogen case with constant wall temperature.....	157
7-17	The mass flow rate for the nitrogen case with constant wall temperature at time=1.5....	157
7-18	The history of temperature gradient along the interface of Case 2 in the nitrogen case with constant wall temperature.	158
7-19	The history of mass flow rate of Case 2 for nitrogen case with constant wall temperature.	158
7-20	The Nusselt number at wall for the nitrogen case with constant wall temperature at time=1.5.	159
7-21	The comparison of Nusselt number by the current method and Hammouda et al.'s correlation.	159
7-22	The U, V and temperature contours of Case 1 in the nitrogen case with wall chilldown at time=1.5.	160
7-23	The wall temperature contours for the nitrogen case with wall chilldown at time=1.5...160	

7-24	The temperature at solid-gas interface for the nitrogen case with wall chilldown at time=1.5	161
7-25	The temperature gradients along the interface of reference for the nitrogen case with wall chilldown at time=1.5	161
7-26	The temperature history of Case 1 in the nitrogen case with wall chilldown at time=1.5.	161
7-27	Temperature gradients along the interface of Case 1 in the nitrogen case with wall chilldown at time=1.5	162
7-28	The mass flow rates for the nitrogen case with wall chilldown and reference case.	162
7-29	U contours of two cases at time=0.4.....	162
7-30	V contours of two cases at time=0.4.....	163
7-31	Temperature contours of two cases at time=0.4.	163
7-32	Temperature at solid-gas interface for the hydrogen and nitrogen cases at time=0.4.	164
7-33	Nusselt number distributions on the pipe wall for the hydrogen and nitrogen cases for both cases at time=0.4.....	164

Abstract of Dissertation Presented to the Graduate School
of the University of Florida in Partial Fulfillment of the
Requirements for the Degree of Doctor of Philosophy

CRYOGENIC TWO-PHASE FLOW AND PHASE-CHANGE HEAT TRANSFER IN
MICROGRAVITY

By

Cheng-Feng Tai

August 2008

Chair: Jacob Nan-Chu Chung
Major: Aerospace Engineering

The applications of cryogenic flow and heat transfer are found in many different types of industries, whether it be the liquid fuel for propulsion or the cryogenic cooling in medical applications. It is very common to find the transportation of cryogenic flow under microgravity in space missions. For example, the liquid oxygen and hydrogen are used to power launch vehicles and helium is used for pressurizing the fuel tank. During the transportation process in pipes, because of high temperature and heat flux from the pipe wall, the cryogenic flow is always in a two-phase condition. As a result, the physics of cryogenic two-phase flow and heat transfer is an important topic for research.

In this research, numerical simulation is employed to study fluid flow and heat transfer. The Sharp Interface Method (SIM) with a Cut-cell approach (SIMCC) is adopted to handle the two-phase flow and heat transfer computation. In SIMCC, the background grid is Cartesian and explicit true interfaces are immersed into the computational domain to divide the entire domain into different sub-domains/ phases. In SIMCC, each phase comes with its own governing equations and the interfacial conditions act as the bridge to connect the information between the two phases. The Cut-cell approach is applied to handle nonrectangular cells cut by the interfaces

and boundaries in SIMCC. With the Cut-cell approach, the conservative properties can be maintained better near the interface.

This research will focus on developing the numerical techniques to simulate the two-phase flow and phase change phenomena for one of the major flow patterns in film boiling, the inverted annular flow.

CHAPTER 1 INTRODUCTION

1.1 Overview

The cryogenic fluids have wide application in the industry. They can be used as liquid fuel like liquid hydrogen and oxygen in the aerospace industry (Filina and Weisend 1996), as coolant like liquid nitrogen and helium in medical applications (Jha 2006). In some special cases, for example, cryogenic fluids are used in spacecrafts not only at low temperatures but also under low gravity. Liquid oxygen and hydrogen are used to power launch vehicles and helium is used for pressurizing fuel tanks (Hands 1986). For this case, the transport and storage of cryogenic fluids under microgravity is regarded as an important element of the space mission. General information about the storage of cryogenic fluids can be found in some papers (Panzarella and Kassemi 2003, Khemis et al. 2004, Plachta et al. 2006).

1.2 Role of Cryogenics in Space Exploration

To explore the space to other planets such as Mars (Mueller and Durrant 1999) is one of all human being's challenges. Therefore, the effective, affordable, and reliable supply of cryogenic fluids in space mission is very important (Cancelli et al. 2005, Heydenreich 1998, Graue et al. 2000). The efficient and safe utilization of cryogenic fluids in thermal management, power and propulsion, and life support systems of a spacecraft during space missions involves the transport, handling, and storage of these fluids in reduced gravity. The uncertainties about the flow pattern and heat transfer characteristics pose a severe design concern. Therefore, the design of cryogenic fluid storage and transfer system is very important and spawns researches in several areas: for example, design of the vessel (Harvey 1974, Bednar 1986), the piping and draining system (Momenthy 1964, Epstein 1965), insulation (Riede and Wang 1960) and safety devices. Moreover, the thermo-fluid dynamics of two-phase systems in reduced gravity encompasses a

wide range of complex phenomena that are not understood sufficiently for engineering design to proceed.

1.3 All Cryogenic Systems Must Be Chilled Down

When any cryogenic system is initially started, which includes rocket thrusters, turbo engines, reciprocating engines, pumps, valves, and pipelines; it must go through a transient chilldown period prior to a steady operation. Chilldown is the process of introducing the cryogenic liquid into the system, and allowing the hardware to cool down to several hundred degrees below the ambient temperature. The chilldown process is anything but routine and requires highly skilled technicians to chill down a cryogenic system in a safe and efficient manner.

The reason that the highly transient chilldown process is extremely complex is because when a cryogenic liquid is introduced into a system that has reached equilibrium with the ambient, voracious evaporation occurs and a very high velocity gas mist traverses through the system. As the system cools, slugs of liquid, entrained in the gas, flow through the system in a two-phase film boiling mode. As the system cools further, a liquid quenching front flows through the system and is accompanied by nucleate boiling and two-phase flow. The rate of heat transfer in the nucleate boiling regime is very high and the system begins to cool down very rapidly. As the system rapidly cools down, the two-phase flow passes through several flow regime transitions to single-phase liquid flow (Burke et al. 1960, Graham et al. 1961, Steward et al. 1970, Bronson et al. 1962). The inherent danger during chilldown is that two-phase flows are inherently unstable and can experience extreme flow and pressure fluctuations. The hardware may be subject to extreme stresses due to thermal contraction and may not be able to sustain extreme pressure fluctuations from the cryogen.

Efficiency of the chilldown process is also a significant concern since the cryogen used to chill down the system can no longer be used for propulsion or power generation. Therefore, chilldown must be accomplished with a minimum consumption of cryogen. As a result, it is important to fully understand the thermo-fluid dynamics associated with the chilldown process and develop predictive models that reliably predict the flow patterns, pressure loss, heat transfer rates, and temperature history of the system.

1.4 Background of a Chilldown Process

Due to the low boiling points, boiling and two-phase flows are encountered in most cryogenic operations. The complexity of the problem results from the intricate interaction of the fluid dynamics and heat transfer, especially when phase-change (boiling and condensation) is involved. Because of the large stratification in densities between the liquid and gas phases, the reduced gravity condition in space would strongly change the terrestrial flow patterns and accordingly affect the momentum and energy transport characteristics. Boiling and two-phase flow behave quite differently when the gravity levels are varied. The proposed research will focus on addressing specific fundamental and engineering issues related to the microgravity two-phase flow and boiling heat transfer of cryogenic fluids. The outcome of the research will provide fundamental understanding on the transport physics of cryogenic boiling and two-phase flows in reduced gravity.

1.5 Objectives of the Research

The main scientific objective is to seek a fundamental understanding through numerical simulations on the boiling regimes, two-phase flow patterns, and heat transfer characteristics for convective boiling in pipes under reduced gravity with relevance to the transport and handling of cryogenic fluids in microgravity. The engineering objective is to address issues that are related to

the design of systems associated with the transport and handling of cryogenic fluids, for example, pressure drop information through pipes and heat transfer coefficients.

1.6 Scope and Structure

In this research, the main objective is to investigate the transportation of cryogenic fluids in microgravity with the phase change phenomena especially the flow pattern and the amount of flow rate of liquid and vapor during the transportation. The experiments about the cryogenic fluids under microgravity are not easy to be performed on the earth. In this research, numerical tools will be adopted instead of experiments. The scope of this dissertation will be:

- To investigate the rate of vaporization (mass loss of cryogenic liquid) based on different driving mechanism and the boundary conditions.
- To study the flow types based on different driving mechanism and the boundary conditions or fluid properties.
- To develop the necessary numerical techniques for phase change computation.

The final goal is to develop a reliable numerical package which can accurately simulate the cryogenic fluid in microgravity and helps the aerospace engineers to design the most reliable cryogenic transportation system in space mission or related industries.

There will be eight chapters in this dissertation. In the first two chapters, the materials about heat transfer and phase-change characteristics of cryogenic flow, impact of microgravity effect and chilldown processes are reviewed. In Chapter 3, the physical model, governing equations and interfacial conditions are listed. In Chapter 4, the numerical techniques about the solver of governing equations, moving interface algorithm, the Sharp Interface Method with Cut-cell approach (SIMCC), and phase change computation will be introduced. In Chapter 5, a series of test cases are done to ensure that the current code is accurate and reliable. Chapter 6 focuses on simulation of the liquid-gas two-phase flow in a pipe without phase change. Chapter 7 is about the phase change and chilldown process simulation of the liquid-gas two-phase flow in a

pipe. In the last chapter, the summarization of current work and the possible future work will be addressed.

CHAPTER 2 PHYSICAL BACKGROUND AND LITERATURE REVIEW

2.1 Boiling Curve and Chillover Process

A typical boiling curve, Figure 2-1, shows the relationship between the heat flux (vertical axis) that the heater supplies to the boiling fluid and the heater surface temperature (horizontal axis). Based on Figure 2-1, a chillover (quenching) process usually starts above point E and then goes towards point D in the film boiling regime as the wall temperature decreases. Point D is called the Leidenfrost point (Carey 1992) which signifies the minimum heater temperature required for the film boiling. For film boiling process, the wall is so hot that liquid will vaporize before reaching the heater surface and that causes the heater to be always in contact with gas. When cooling beyond the Leidenfrost point, if a constant heat flux heater were used, then the boiling would shift from film to nucleate boiling (somewhere between points A and B) directly with a substantial decrease in the wall temperature because the transition boiling is an unstable process.

2.2 Two-Phase Flow Patterns and Heat Transfer Regimes

In a cryogenic chillover process, the wall temperature is always higher than the saturation temperature of the transported liquid. Therefore, the cryogenic chillover process in a pipe is associated with a standard two-phase flow. In this process, the types of flow and heat transfer can not be determined separately as the dominant heat transfer mechanism is dictated by the flow pattern. The heat transfer also affects the flow pattern development. For the two-phase flow regime, there are several possible factors that can influence it, such as the flow rate, the orientation of pipe, the fluid properties and the heat flux at the wall of pipe (Yuan et al. 2007). In Carey's work (1992), he showed the different two-phase flow types in a horizontal pipe. The flow types may be bubbly flow, plug flow, stratified flow, wavy flow, slug flow or annular flow.

In Dziubinski et al's work (2004), they showed the flow regimes of a two-phase flow in a vertical tube and the possible flow types are bubbly flow, slug flow, churn flow, annular flow and mist flow. The main difference between the horizontal and vertical flows is the effect of gravity that causes the horizontal flow to become non-symmetrical to the centerline of the pipe.

With regard to the chilldown process in the film boiling regime, depending on the local quality and other thermohydraulic parameters, the flow regime can be either dispersed flow, annular flow, or inverted annular flow. The corresponding heat transfer regime will be dispersed flow film boiling, annular flow film boiling, or inverted annular film boiling, respectively. As the wall temperature decreases below a certain degree, the liquid phase is able to contact the wall of the pipe. The leading liquid-wall contact point which is often referred to as the quenching front or sputtering region is characterized by a violent boiling process with a significant wall temperature decrease. The quenching front will propagate downstream with the flow. The heat transfer mechanism at the quenching front is the transition boiling, which is more effective than the film boiling heat transfer due to partial liquid wetting of the wall surface. This re-establishment of liquid-wall contact is called rewetting phenomenon and has been a research interest for several decades.

Nucleate boiling heat transfer dominates after the quenching front. For a vertical pipe, the flow regime can be annular flow, slug flow or bubbly flow. While for a horizontal pipe, the flow regime is generally stratified flow. As the wall temperature decreases further, the nucleate boiling process gradually reverts back to pure convection until the wall temperature reaches the thermal equilibrium with the wall, which denotes the end of the chilldown process. Figure 2-2 illustrates the flow patterns and corresponding heat transfer regimes.

2.3 Two-Phase Flow in Microgravity

In this research, the main purpose is to simulate the cryogenic chilldown process under reduced gravity in space to obtain the design parameters for the related equipment. The condition of low gravity has a significant impact on the two-phase flow model. It is the most important factor for determining the gas/liquid interfacial dynamics. The entire flow field will now be controlled by the convection, pressure gradient and viscous effects only. There will be some contributions from the surface-tension induced forces and the presence of the solid wall. When the dynamics is changed, the flow regime will also be changed. Figure 2-3 is the possible flow patterns under microgravity. Figure 2-4 is an example to show the distinctively different flow patterns in a horizontal pipe between terrestrial and microgravity conditions.

For annular flow film boiling, the effect of gravity is assessed based on the ratio of Gr/Re^3 , where Gr is the Grashof number and Re is the Reynolds number. The gravity effect is measured by the natural convection contribution, which is characterized by the Gr , while the forced convective film boiling is scaled by the Reynolds number. According to Gebhart et al.'s work (1988), if the velocity of gas is greater than 10 cm/s, then the Gr/Re^3 is less than 0.2. Natural convection is negligible for Gr/Re^3 less than 0.225.

2.3.1 Isothermal Two-Phase Flows in Microgravity

In order to investigate the impact of gravity quantitatively, some detailed experiments under simulated microgravity conditions have been performed on an aircraft (Rezkallah and Zhao 1995, Colin et al. 1991) and on the ground in a drop tower (Mishima and Hibiki 1996) because it is too expensive to do it in space. The first report on microgravity isothermal flow pattern for a large range of liquid to gas ratios was provided by Dukler et al. (1988). In their research, they showed the flow patterns are different between the 1-g and the μ -g conditions.

Flow patterns under microgravity can be broadly classified into three types: the bubbly, the slug and the annular flow.

In the beginning, experiments could only be performed in a pipe with a very small radius. Therefore, this experimental data may not be accurate enough. In the following studies, the researchers tried to perform the experiment with larger pipes and various fluids to determine the flow patterns (Janicot 1988, Colin et al. 1991, Zhao and Rezkallah 1993).

In other's researches (Zhao and Rezkallah 1995, Rezkallah 1996), the flow patterns were classified into three regions based on the dynamics of a flow: a surface tension region (bubbly and slug flow), an inertia region (annular flow) and the transitional region (frothy slug-annular flow).

There are several possible factors that may influence the flow patterns under microgravity such as the pressure drop (Zhao and Rezkallah 1995), surface tension (Rezkallah 1996), flow rate, pipe diameter and viscosity (Bousman et al. 1996). In Rezkallah's work (1996), he showed the flow patterns based on different Weber numbers and there are two transition lines which divide the flow into three regions. When the Weber number of the gas phase becomes larger; the flow tends to become annular; otherwise bubbly flow and slug flow are observed.

In Bousman et al.'s work (1996), they showed the flow patterns based on different superficial velocities of liquid and gas phases.

When the superficial velocity of the liquid phase is larger, the flow patterns are bubbly flows and move to annular flows when the superficial velocity of gas phase is larger.

2.3.2 Two-Phase Flow and Heat Transfer in Microgravity

In general, there is little heat transfer data for cryogenic flow boiling in reduced gravity. Only two reports were found. Adham-Khodaparast et al. (1995) investigated the flow film boiling during quenching of R-113 on a hot flat surface. They used microsensors to record

instantaneous heat flux and heater surface temperature during the film boiling on board a KC-135 aircraft. Antar and Collins (1997) reported flow visualizations and measurements for flow film boiling of liquid nitrogen in tubes on board KC-135 aircraft. They were particularly interested in the gas/liquid flow pattern and the thermal characteristics. They identified a new gas/liquid flow pattern that is unique to low gravity: a sputtering leading core followed by a liquid filament annular flow pattern. This new flow pattern is composed of a long and connected liquid column that is flowing in the center of the pipe surrounded by a thick gas layer. The gas annulus that separates the liquid filament from the wall is much thicker than that observed in the terrestrial experiment. They attributed the filamentary flow to the lack of difference in the speed of gas and liquid phases. On the heat transfer side, they reported that the quench process is delayed in low gravity and the pipe wall cooling rate was diminished under microgravity conditions.

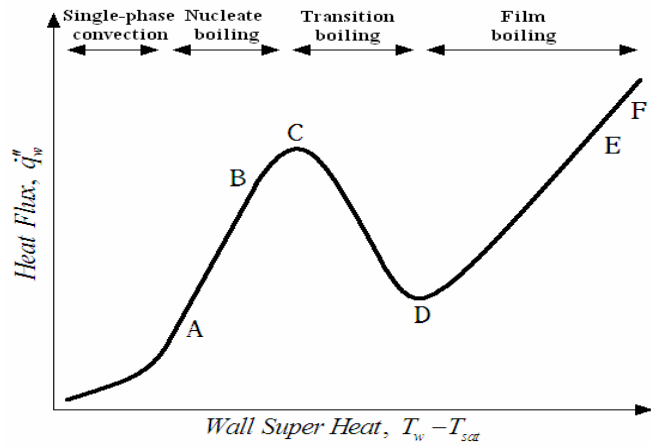


Figure 2-1. Typical boiling curve.

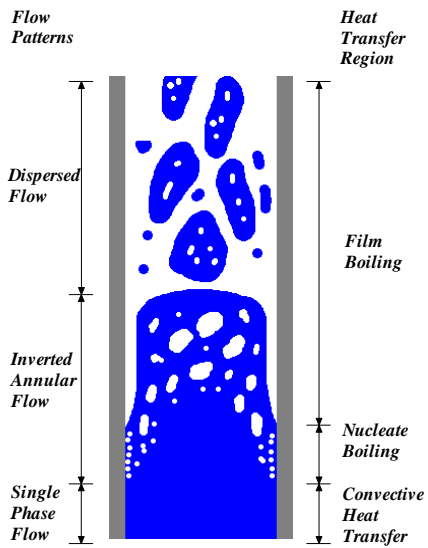


Figure 2-2. Flow regimes and heat transfer regimes in a heated channel.

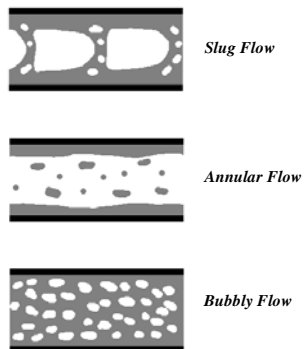


Figure 2-3. Flow regimes under microgravity.

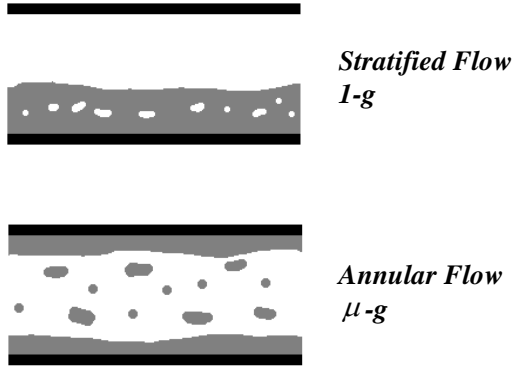


Figure 2-4. Effect of the gravity on flow regimes.

CHAPTER 3 PROBLEM DEFINITION AND GOVERNING EQUATIONS

3.1 Modeling Cryogenic Chillover in Microgravity

According to the literature review presented in the previous chapter, for most part of the cryogenic chillover process in microgravity, the two-phase flow is in the inverted annular flow regime with film boiling. Based on the general boiling curve shown in Figure 2-1, initially the state of boiling is located around point F due to a large temperature difference between the wall (room temperature ~ 300 K) and the saturation temperature of the cryogenic fluid (~ 77 K for liquid nitrogen and ~ 20 K for liquid hydrogen) when the cryogen first enters the pipe. The schematic of a representative cryogenic flow system is given in Figure 3-1. As the wall is cooled down by the cryogenic two-phase flow, the boiling state will move from point F towards point E and then approach point D when the wall is cooled down further. It is noted that the route from point E to point D is followed for the current quenching process, instead of the route from point E to point C, because the wall temperature is reduced during the quenching process by the heat transfer and can not be changed independently.

During the initial stage, a quenching front would form that is followed by an inverted annular flow pattern with gas phase next to the pipe wall and a liquid core in the center (Antar and Collins 1997). As the liquid vaporizes, the radius of the liquid core would decrease as it travels downstream. Figure 3-2 illustrates the proposed physical model of the cryogenic two-phase film boiling in microgravity, a continuous inverted annular flow.

There are several research publications about the inverted annular flow (Yadigaroglu 1978, Ishii and Jarlais 1987, Aritomi et al. 1990, Nelson and Unal 1992, Hammouda et al. 1997). However, the heat fluxes in their researches were set at constant values or different from this research. In this research, the temperature of the wall will vary and also the strength of heat flux will change accordingly.

The physical phenomena inside the tank and other devices downstream of the pipe exit will not be included in the current simulation. Only the flow in the pipe will be considered in this

research. In the absence of gravity, it is reasonable to assume that the inverted annular flow is axisymmetric. Figure 3-3 shows the schematic for the idealized continuous inverted annular flow that will be used as the physical model in the current numerical simulation.

To complete the entire conjugate heat transfer path, the two-phase flow inside the pipe must be connected to the heat source, the pipe wall. Figure 3-4 shows the heat transfer network of this conjugate heat transfer. The outer surface of the wall is assumed to be perfectly insulated. Therefore, on the outside of wall, the insulated boundary condition will be assigned.

3.2 Geometry, Computational Domain and Initial, Boundary Conditions

Since, this is an axisymmetric computation, a rectangular domain with a width of 0.5 (pipe radius) is used to simulate the circular pipe. The length of the domain will depend on the problems. The minimum grid spacing is 0.01. The initial shape of the liquid core is a quart-circle with radius 0.38 plus a straight line 0.03 as shown in Figure 3-5. Initially, the pipe is filled with the stationary gas and at the entrance. A quart-circle interface is used to divide the domain into different phases. The temperatures of wall and gas phase are assigned the same initially ($=1.0$) and the temperature of liquid core is set the same as the temperature at inlet ($=0.0$). The boundary conditions for this problem can be divided into two parts:

Liquid and gas phases inside the pipe: In the real application such as space mission, the mass flow rate should be most important concern in order to keep the enough thrust so that the mass flow rate in this research at the inlet is assigned as constant by an uniform velocity ($=1.0$). In the incompressible flow, the total mass flow rate at outlet should be equal to the mass flow rate at inlet and plus the mass flow rate generated from the liquid-gas interface due to the phase change. By this idea, the total mass flow rate at outlet can be obtained. In this research, the device at the downstream is not specified so that there are not exact boundary conditions at the outlet. In numerical simulation, the extrapolation strategy is usually used for the undetermined boundary condition. In this research, the second order extrapolation is applied for the velocity boundary condition at outlet and this velocity profile will be corrected by the total mass flow rate.

By this strategy, the velocity profile at the outlet should be reasonable and the conservation of mass is kept.

In this research, the pressure at inlet of pipe is assigned as constant ($=1.0$). In Navier-Stokes equations, this constant does not mean anything but a reference value and it can be any value. In the incompressible pipe flow computation, the most important thing is the pressure drop and this pressure drop should be balanced by the shear stress from wall. In this research, the exact pressure at the outlet is unknown so that the second order extrapolation is assigned to get a reasonable estimation value for pressure from the nearby locations.

In the incompressible pipe flow, there are two velocity and two pressure boundary conditions at the inlet and outlet. In numerical simulation, if the exact/real boundary conditions are known, the numerical boundary conditions can be assigned based on this exact boundary conditions or at least one condition must be flexible. In this research, the flexible boundary condition is the pressure at the outlet. By this flexible pressure boundary condition at outlet, the correct pressure drop can be obtained to balance the shear stress from the wall. Since it is an asymmetric pipe flow computation, the symmetric condition is assigned at the centerline and non-slip condition is assigned at the wall.

The temperature boundary conditions in this research are assigned constant at the inlet ($=0.0$) and second order extrapolation at downstream, symmetric condition at the centerline. For the temperature at wall, it depends on different cases and governed by interfacial condition.

Solid wall: The boundary conditions for the left and upper sides are the insulated boundary conditions and second order extrapolation for temperature at right side.

3.3 Assumptions

In this section, the assumptions in this research are made as following:

- The flow and heat transfer are axisymmetric in a 2D cylindrical coordinates system.
- The flows are incompressible for both liquid and vapor phases. In most cryogenic transport systems, the flow rate may not be very large (Mach number < 0.3) and in this

research the temperature differences will be limited to moderate values such that the compressibility should be negligible.

- A single-component inverted annular two-phase flow under film boiling is taking place in a circular pipe with no body force in a gravity-free environment.
- Viscous dissipation is neglected due to low velocities.
- Constant properties in the liquid and gas phases.
- Fluids in both phases are Newtonian fluids.
- Thermal equilibrium at the liquid-gas interface and thermal non-equilibrium for the gas phase.
- The gas phase is transparent for thermal radiation, the wall is a grey body, and thermal radiation is a surface phenomenon for the liquid phase.

3.4 Governing Equations

In this research, the Sharp Interface Method (SIM) will be adopted to treat the moving interface. In the SIM, the interface is a true surface with zero volume, so the governing equations of each phase are solved separately and transport fluxes are matched between the two phases at the interface. In the cryogenic two-phase flow, the mass, momentum and energy equations in the liquid and gas phases are developed separately. Based on the above assumptions, the governing equations are listed below:

- Liquid-phase equations:

$$\begin{aligned}\bar{\nabla} \cdot \bar{u}_l &= 0 \\ \rho_l \left[\frac{\partial \bar{u}_l}{\partial t} + \bar{\nabla} \cdot (\bar{u}_l \bar{u}_l) \right] &= -\bar{\nabla} p_l + \mu_l \nabla^2 \bar{u}_l \\ \rho_l c_{pl} \left[\frac{\partial T_l}{\partial t} + \bar{\nabla} \cdot (\bar{u}_l T_l) \right] &= k_l \nabla^2 T_l\end{aligned}\tag{3-1}$$

- Gas-phase equations:

$$\begin{aligned}\bar{\nabla} \cdot \bar{u}_g &= 0 \\ \left[\frac{\partial(\rho_g \bar{u}_g)}{\partial t} + \bar{\nabla} \cdot (\rho_g \bar{u}_g \bar{u}_g) \right] &= -\bar{\nabla} p_g + \bar{\nabla} \cdot (\mu_g \bar{\nabla} \bar{u}_g) \\ \left[\frac{\partial(\rho_g c_{pg} T_g)}{\partial t} + \bar{\nabla} \cdot (\rho_g c_{pg} \bar{u}_g T_g) \right] &= \bar{\nabla} \cdot (k_g \bar{\nabla} T_g)\end{aligned}\quad (3-2)$$

- Solid-phase equation:

$$\rho_w c_{pw} \frac{\partial T_w}{\partial t} = \bar{\nabla} \cdot (k_w \bar{\nabla} T_w) \quad (3-3)$$

where subscripts 'l', 'g' and 'w' denote the liquid, gas and solid phases, respectively; \bar{u} is the velocity vector, T is the temperature, ρ is the density, μ is the dynamic viscosity, c_p is the specific heat, k is the thermal conductivity.

3.4.1 Interfacial Conditions

Force balance in the normal direction at the liquid-gas interface:

$$p_l - p_g = \sigma \mathcal{K} + \rho_g (\bar{u}_g - \bar{u}_{\text{int}})^2 - \rho_l (\bar{u}_l - \bar{u}_{\text{int}})^2 + (\bar{\tau}_l \cdot \bar{n}) \cdot \bar{n} - (\bar{\tau}_g \cdot \bar{n}) \cdot \bar{n} \quad (3-4)$$

where $\bar{\tau}_l$ and $\bar{\tau}_g$ represent the viscous stress tensors in the liquid and gas phases, respectively; σ is the surface tension coefficient; \mathcal{K} is the curvature of the interface; p_l and p_g are the pressures in the liquid and gas phase, respectively.

Mass flux continuity at the liquid-gas interface:

$$\dot{m}'' = \rho_l (\bar{u}_l - \bar{u}_{\text{int}}) \cdot \bar{n} = \rho_g (\bar{u}_g - \bar{u}_{\text{int}}) \cdot \bar{n} \quad (3-5)$$

where \dot{m}'' is the interfacial mass flux, \bar{n} is the unit normal vector at the interface; \bar{u}_{int} , \bar{u}_l and \bar{u}_g are the velocities of interface, liquid and gas phases, respectively. In a two-phase flow, energy must be conservative and the temperature is the same for both phases at the interface under the thermal equilibrium condition.

Interfacial energy conservation condition at the liquid-gas interface:

$$\lambda \dot{m}'' = -\left(k_l (\bar{\nabla} T_l) - k_g (\bar{\nabla} T_g) - \dot{q}_{\text{rad}}'' \right) \cdot \bar{n} = \lambda \rho_l (\bar{u}_l - \bar{u}_{\text{int}}) \cdot \bar{n} \quad (3-6)$$

Interfacial temperature condition at the liquid-gas interface:

$$T_l = T_g = T_{\text{int}} \quad (3-7)$$

where λ is the latent heat of vaporization. \dot{q}_{rad}'' is the thermal radiation heat flux received by the liquid surface from the wall.

Thermal radiation at the liquid-gas interface:

Based on the simplifying assumption stated above and also the fact that the liquid phase is entirely enclosed by the pipe wall, the thermal radiation heat flux received on the surface of the liquid phase is as follows:

$$\dot{q}_{rad}'' = \frac{\sigma(T_w^4 - T_{sat}^4)}{\frac{1}{\varepsilon_l} + \frac{(1 - \varepsilon_w)}{\varepsilon_w} \left(\frac{R_l}{R_{wi}}\right)} \quad (3-8)$$

where ε_w and ε_l are the emissivities of solid wall and liquid phase, respectively. R_{wi} and R_l are the radii of the inner surface of pipe and liquid core, respectively and $\sigma = 5.6697 \times 10^{-8}$ is the Stefan-Boltzmann coefficient.

Continuous heat flux at solid-gas interface:

$$k_w \frac{\partial T_w}{\partial r} = k_g \frac{\partial T_g}{\partial r} + \dot{q}_{rad,w}'' \quad \text{at } r = R_{wi} \quad (3-9)$$

Thermal radiation at the solid-gas interface:

$$\dot{q}_{rad,w}'' = \frac{\sigma(T_w^4 - T_{sat}^4)}{\frac{1}{\varepsilon_l} \left(\frac{R_{wi}}{R_l}\right) + \frac{1}{\varepsilon_w} - 1} \quad (3-10)$$

Continuous temperature at solid-gas interface:

$$T_w = T_g \quad \text{at } r = R_{wi} \quad (3-11)$$

Insulation on the outer surface of pipe:

$$\frac{\partial T_w}{\partial r} = 0 \quad \text{at } r = R_{wo} \quad (3-12)$$

where R_{wo} is the radius of outer surface of the pipe.

3.4.2 Non-dimensionalization

In this work, all the computational quantities are non-dimensional. The governing equations of each phase and the interfacial conditions must be non-dimensionalized first. The reference scales are characteristic length L and velocity U and the characteristic time is L/U .

The characteristic length in this research is the diameter of the pipe, and characteristic velocity is the inlet velocity. The characteristic temperature scale is $\Delta T = T_\infty - T_{sat}$. T_∞ is the ambient temperature and wall initial temperature. T_{sat} is the fluid saturation temperature. Based on these reference scales, the dimensionless variables are defined as

$$\bar{x}^* = \bar{x}/L, \quad t^* = tU/L, \quad \rho^* = \rho/\rho_{ref}, \quad \mu^* = \mu/\mu_{ref}, \quad \sigma^* = \sigma/\sigma_{ref}, \quad k^* = k/k_{ref},$$

$$c_p^* = c_p/c_{p-ref}, \quad \bar{u}^* = \bar{u}/U, \quad p^* = p/(\rho_{ref}U^2), \quad T^* = (T - T_{sat})/(T_\infty - T_{sat})$$

where the fluid properties of the liquid phase at the inlet are used as references.

After the non-dimensionalization procedure, the original governing equations and the interfacial conditions can be written as follows (the asterisks for dimensionless quantities are dropped from this point on for convenience):

- Liquid-phase equations:

$$\bar{\nabla} \cdot \bar{u} = 0$$

$$\frac{\partial \bar{u}}{\partial t} + \bar{\nabla} \cdot (\bar{u}\bar{u}) = -\bar{\nabla} p + \frac{1}{Re} \nabla^2 \bar{u} \quad (3-13)$$

$$\frac{\partial T}{\partial t} + \bar{\nabla} \cdot (\bar{u}T) = \frac{1}{Pe} \nabla^2 T$$

- Gas-phase equations:

$$\bar{\nabla} \cdot \bar{u} = 0$$

$$\left[\frac{\partial \left(\frac{\rho_g}{\rho_l} \bar{u} \right)}{\partial t} + \bar{\nabla} \cdot \left(\frac{\rho_g}{\rho_l} \bar{u}\bar{u} \right) \right] = -\bar{\nabla} p + \frac{1}{Re} \bar{\nabla} \cdot \left(\frac{\mu_g}{\mu_l} \bar{\nabla} \bar{u} \right) \quad (3-14)$$

$$\left[\frac{\partial \left(\frac{\rho_g c_{pg}}{\rho_l c_{pl}} T \right)}{\partial t} + \bar{\nabla} \cdot \left(\frac{\rho_g c_{pg}}{\rho_l c_{pl}} \bar{u}T \right) \right] = \frac{1}{Pe} \bar{\nabla} \cdot \left(\frac{k_g}{k_l} \bar{\nabla} T \right)$$

- Solid-phase equation:

$$\left(\frac{\rho_w}{\rho_l}\right)\frac{\partial T}{\partial t} = \left(\frac{k_w c_{pl}}{k_l c_{pw}}\right)\frac{1}{Pe}\bar{\nabla}\cdot(\bar{\nabla}T) \quad (3-15)$$

where the dimensionless parameter Re is the Reynolds number and Pe is Peclet number.

$$Re = \frac{\rho_l UL}{\mu_l}, \quad Pe = \frac{\rho_l c_{pl} UL}{k_l}$$

- Interfacial conditions:

Force balance in the normal direction at the liquid-gas interface:

$$p_l - p_g = \frac{\kappa}{We} + \rho_g (\bar{u}_g - \bar{u}_{int})^2 - \rho_l (\bar{u}_l - \bar{u}_{int})^2 + \frac{1}{Re} \left(\left(\frac{\partial u_n}{\partial n} \right)_l - \left(\frac{\mu_g}{\mu_l} \right) \left(\frac{\partial u_n}{\partial n} \right)_g \right) \quad (3-16)$$

Mass flux continuity at the liquid-gas interface:

$$\dot{m}'' = \rho_l (\bar{u}_l - \bar{u}_{int}) \cdot \bar{n} = \rho_g (\bar{u}_g - \bar{u}_{int}) \cdot \bar{n} \quad (3-17)$$

Interfacial energy conservation condition at the liquid-gas interface:

$$(u_n)_{int} - (u_n)_g = \frac{Ja}{Pe} \frac{\rho_l}{\rho_g} \left[\left(\frac{k_l}{k_g} \right) \frac{\partial T_l}{\partial n} - \left(\frac{\partial T_g}{\partial n} \right) \right] - \frac{\dot{q}_{rad}'' L}{k_l \Delta T} \quad (3-18)$$

where $\Delta T = (T_\infty - T_{sat})$ and the dimensionless parameter We is the Weber number and Ja is the Jakob number.

$$We = \frac{\rho_l U^2 L}{\sigma}, \quad Ja = \frac{k_g c_{pl} \Delta T}{k_l \lambda}$$

Interfacial temperature condition at the liquid-gas interface:

$$T_l = T_g = T_{int} \quad (3-19)$$

Continuous heat flux at solid-gas interface:

$$k_w \frac{\partial T}{\partial r} = k_g \frac{\partial T}{\partial r} + \frac{\dot{q}_{rad,w}'' L}{k_l \Delta T} \quad \text{at } r = R_{wi} / L \quad (3-20)$$

Continuous temperature at solid-gas interface:

$$T_w = T_g \quad \text{at } r = R_{wi} / L \quad (3-21)$$

Insulation on the outer surface of pipe:

$$\frac{\partial T}{\partial r} = 0 \quad \text{at } r = R_{wo} / L \quad (3-22)$$

In this research, the heat flux by the thermal radiation $\dot{q}_{rad,w}''$, \dot{q}_{rad}'' are computed with dimension and converted to the dimensionless quantity during computation and the conversion factor is $\frac{L}{k_l \Delta T}$.

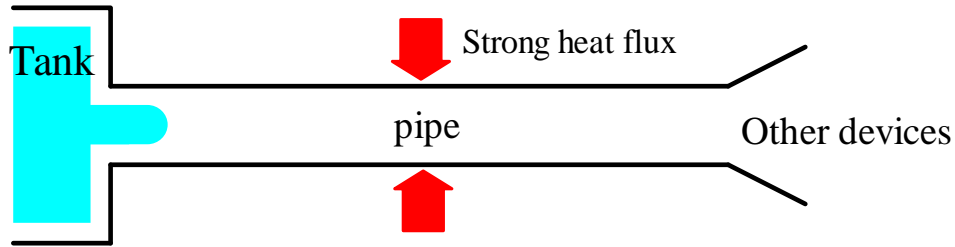


Figure 3-1. A simple cryogenic system.

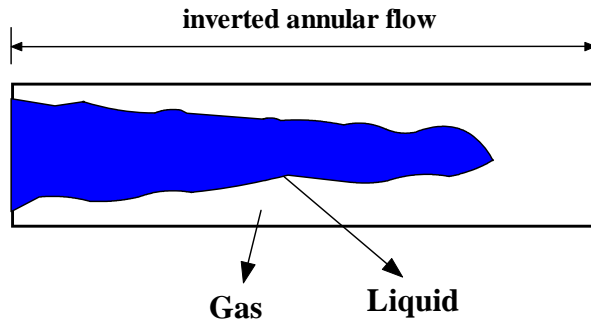


Figure 3-2. Inverted annular flow.

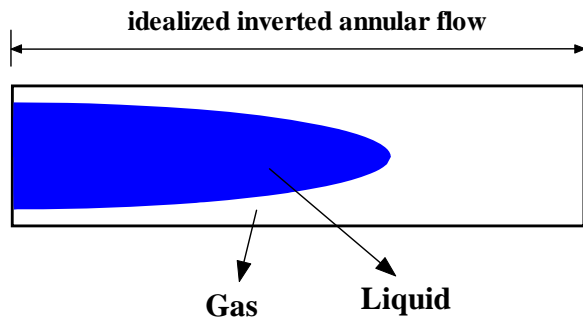


Figure 3-3. Idealized inverted annular flow.

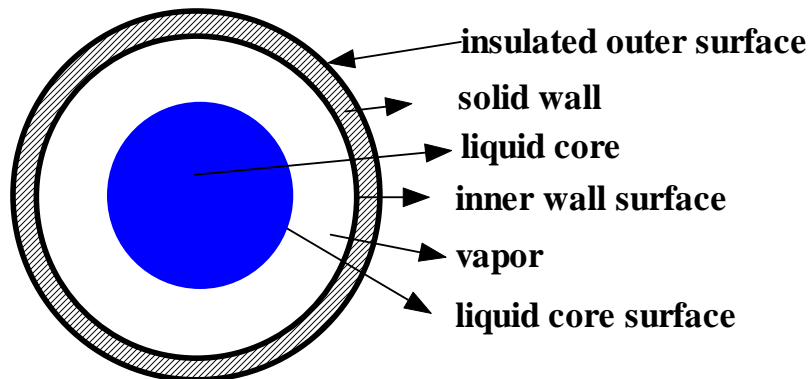


Figure 3-4. Conjugate heat transfer.

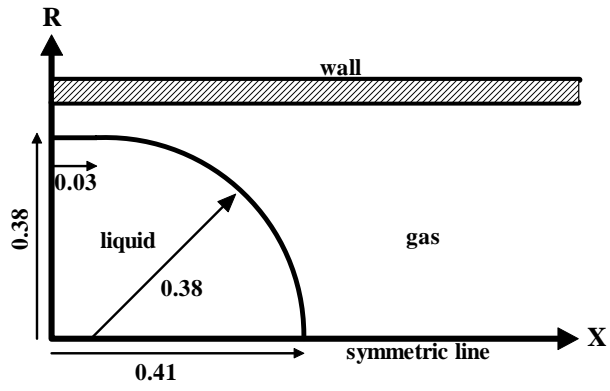


Figure 3-5. The initial shape of liquid core.

CHAPTER 4 SOLUTION METHOD

4.1 Introduction

In earlier numerical simulations about the chilldown process, scholars have used simplified models to solve the chilldown process, such as the one-dimension model (Chi 1965), the homogeneous model (Cross et al. 2002), the two-fluid model (Ishii 1975, Ardron 1980, Ishii and Mishima 1984), the three-fluid model (Alipchenkov et al. 2004) and the pseudo-steady model (Liao et al. 2006). Also, different important correlations are developed such as the correlation for saturated boiling (Chen 1966), subcooled boiling (Gungor and Winterton 1986) and pool boiling (Steiner 1986). By these simplified modeling works, the complex governing equations and interfacial conditions can be simplified and desired results can be obtained very fast and easily. However, these modeling works need the correlations by the experiments to simplify the governing equations so they can not be applied in broad applications. Also, because of simplification, the modeling work cannot give all the necessary and real-time information about the chilldown process such as the flow patterns, and may be not very accurate for some important characteristics. Therefore, direct numerical simulation is adopted in this research. By directly solving the general governing equations, the interfacial conditions and proper initial/boundary conditions, the computation can be unsteady and all the flow characteristics can be captured. All the information can be saved and give a great help in different engineering aspects.

As illustrated in Chapter 3, the complex problem of two-phase flow and conjugate heat transfer with phase change does not allow any possibility of an analytical solution. In this chapter, the numerical simulation method that has been adopted for seeking the solutions is presented. The central infrastructure of this method is based on the concept of a sharp interface

that truly separates the liquid phase from the gas phase. In other words, the interface is a true surface without any volume association. The key elements of the Sharp Interface Method (SIM) are listed as follows:

- Fixed Cartesian Grid – The computational framework is built on an Eulerian-Cartesian grid. With this underlying fixed grid system, a so-called Cut-cell approach is used to treat the interfaces and boundaries that do not align with the fixed Cartesian grid.
- Lagrangian Moving Sharp Interface Algorithm – To track the moving vaporization front, separate marker points(Nichols 1971) are used to identify the phase-change interface. These points that are connected by piece-wise polynomials are employed to capture the deformation and movement of the sharp interface through the translation of these markers over the underlying Eulerian fixed grid.
- Fractional Step Method – For each phase domain, the fractional step method is used to numerically integrate the governing equations in that phase. The overall solution is obtained by matching the mass, momentum and heat fluxes from both phases at the sharp interface.

4.2 Fractional Step Method within the Finite Volume Framework

In order to best enforce the conservation laws and to treat the discontinuity at the interface, the finite volume method (Versteeg and Malalasekera 1995) is used to discretize the governing equations. By the finite volume framework, the governing equations listed in the previous chapter will be integrated over a finite control volume which is called a unit cell as shown in Figure 4-1. The integral forms of governing equations for an incompressible flow with constant properties are given below.

Continuity equation:

$$\int_{cs} \vec{u} \cdot \vec{n} dS = 0 \quad (4-1)$$

Momentum equation:

$$\int_{cv} \frac{\partial \vec{u}}{\partial t} dV + \int_{cs} \vec{u} (\vec{u} \cdot \vec{n}) dS = - \int_{cs} p \vec{n} dS + \frac{1}{Re} \int_{cs} \vec{\nabla} \vec{u} \cdot \vec{n} dS \quad (4-2)$$

Energy equation:

$$\int_{cv} \frac{\partial T}{\partial t} dV + \int_{cs} T (\vec{u} \cdot \vec{n}) dS = \frac{1}{Pe} \int_{cs} \vec{\nabla} T \cdot \vec{n} dS \quad (4-3)$$

where cv and cs represent the control volume and the surface of the control volume, respectively. \vec{n} is the outward normal vector from the control volume surface, \vec{u} is the velocity vector, p is the pressure and T is the temperature.

In this research, a cell-centered collocated (non-staggered) approach (Ferziger and Peric 1996) on the Cartesian grid system is adopted, the primary variables (velocity, pressure and temperature) are defined at the cell centers and the primary variables needed at the cell faces will be evaluated by interpolation from respective variables at the cell centers as shown in Figure 4-1.

A second order accurate two-step fractional step method (Chorin 1968, Kim and Moin 1985, Zang et al. 1994) is used for advancing the solutions of the integral unsteady governing equations in time. In this approach, the solution procedure is advanced from time step “n” to “n+1” through an intermediate diffusion-convection step where the momentum equation without the pressure gradient terms is first solved and advanced in a half time step. The intermediate diffusion-convection momentum equation can be discretized as

$$\int_{cv} \frac{\vec{u}^* - \vec{u}^n}{\Delta t} dV = -\frac{1}{2} \int_{cs} \left[3\vec{u}^n (\vec{U}^n \cdot \vec{n}) - \vec{u}^{n-1} (\vec{U}^{n-1} \cdot \vec{n}) \right] dS + \frac{1}{2Re} \int_{cs} (\vec{\nabla} \vec{u}^* + \vec{\nabla} \vec{u}^n) \cdot \vec{n} dS \quad (4-4)$$

where \vec{u}^* is the intermediate velocity at the cell center and \vec{U} is the velocity at center of the cell face. The cell surface velocity is used to evaluate the fluxes going in or out of a control volume.

After the \vec{u}^* is determined, \vec{U}^* , the intermediate velocity at the center of cell face, is calculated by interpolating between the respective cell-center velocities. The first term on the right hand side is the convective term. A second order accurate Adams-Bashforth scheme (Bashforth and Adams 1883) is used to discretize the convective term. The second term is the diffusive term that

is discretized by the implicit Crank-Nicolson scheme (Crank and Nicolson 1947). This eliminates the potential viscous instability that could be quite severe in the simulation of viscous flows. Once the intermediate velocity is obtained, the pressure is obtained by the correction step:

$$\int_{cv} \frac{\bar{u}^{n+1} - \bar{u}^*}{\Delta t} dV = - \int_{cv} \bar{\nabla} p^{n+1} dV \quad (4-5)$$

In this pressure correction step, the final velocity \bar{u}^{n+1} must satisfy the integral mass conservative equation. The integral mass conservative equation can be rewritten as the following form:

$$\int_{cs} (\bar{U}^{n+1} \cdot \bar{n}) dS = 0 \quad (4-6)$$

Therefore, the integral pressure correction equation can be expressed as

$$\int_{cs} (\bar{\nabla} p^{n+1}) \cdot \bar{n} dS = \int_{cs} (\bar{U}^* \cdot \bar{n}) dS \quad (4-7)$$

Once the pressure is obtained, the intermediate velocity can be corrected and updated to obtain the final velocity by

$$\begin{aligned} \bar{u}^{n+1} &= \bar{u}^* - \Delta t \left(\bar{\nabla} p^{n+1} \right)_{cell\ center} \\ \bar{U}^{n+1} &= \bar{U}^* - \Delta t \left(\bar{\nabla} p^{n+1} \right)_{cell\ face} \end{aligned} \quad (4-8)$$

The energy equation is solved by similar procedure but the predict-correct procedure is not required because the energy equation in this research is a standard convection-diffusion equation.

The discretized energy equation is similar to Equation 4-4 and can be discretized as (Francois 2002)

$$\begin{aligned} \int_{cv} \frac{T^{n+1} - T^n}{\Delta t} dV &= - \frac{1}{2} \int_{cs} \left[3T^n (\bar{U}^n \cdot \bar{n}) - T^{n-1} (\bar{U}^{n-1} \cdot \bar{n}) \right] dS \\ &+ \frac{1}{2Pe} \int_{cs} (\bar{\nabla} T^{n+1} + \bar{\nabla} T^n) \cdot \bar{n} dS \end{aligned} \quad (4-9)$$

For the incompressible flow with non-constant properties, the fractional step method can work also and just needs to include the flow properties into each procedure (Ferziger and Peric 1996).

4.3 Cartesian Grid Method for a Complex Geometry

In the early development of computational multiphase flow, some researchers adopted the curvilinear grid system (Ryskin and Leal 1984, Dandy and Leal 1989, Raymond and Rosant 2000, Lai et al. 2003). This approach is simple but not easy to apply. In order to describe the deformation of an interface between different phases, a very powerful grid generation is required and also, the grid has to be updated frequently to obtain the convergent solution and therefore it is very computationally intensive. In recent multiphase computational approaches, several Cartesian grid methods are broadly used such as the Sharp Interface Method (SIM) (Udaykumar et al. 2001, Ye et al. 2001), the Immersed Boundary Method (IBM) (Peskin 1977, Singh and Shyy 2007), the Front Tracking Method (Qian et al. 1998, Al-Rawahi and Tryggvason 2004), the Volume of Fluid (VOF) Method (Hirt and Nichols 1981, Pilliod and Puckett 2004), the Level Set Method (Ni et al. 2003, Tanguy and Berlemont 2005) the coupled Level Set and Volume of Fluid Method (Son 2003, Sussman 2003) and the Phase Field Method (Badalassi et al. 2003, Sun and Beckermann 2007). Based on the computational framework, Sharp Interface Method, Front Tracking Method and Immersed Boundary Method are classified under the mixed Eulerian-Lagrangian category and Level Set Method, Volume of Fluid Method and Phase Field Method are in the Eulerian category (Shyy et al. 1996).

In this research, the Sharp Interface Method (SIM), a branch of the mixed Eulerian-Lagrangian Cartesian grid method, is adopted to handle the complex geometries. In the SIM, the Cartesian grid is designed as a background mesh, and the explicit interfaces are used to describe the shapes of the objects on the background grid. The interfacial dynamics associated with the

moving/fixed boundaries need to be considered simultaneously. In the mixed Eulerian-Lagrangian approach the interface is constructed by a sequence of marker points. With these marker points, the shape and location of the interface are determined by designated interpolation procedures, while the overall fluid flow is computed based on the fixed Cartesian grid. In the SIM, the interface is treated explicitly with zero thickness, in accordance with the continuum mechanics model. The primary variables at the interface are computed via the interfacial conditions

The SIM defines the relations between the background grid and the interfaces. Because of the non-Cartesian interfaces, some cells containing the interface will be cut and form the non-rectangular cut-cells. Special methods are needed to handle these cut cells. In this research, a Cut-cell approach (Ye et al. 2001, Ye et al. 2004, Tai and Shyy 2005) is employed to treat the interface and boundary cells. In the Cut-cell approach, each segment of the cut-cell is merged into a neighboring cell or assigned the identity of the original Cartesian cell. Hence, even though the underlying grid is Cartesian, the cut cells are reconstructed to become the non-rectangular cells and the cut-sides will form the interface. After the reconstruction, the entire grid is filled with the rectangular grid and non-rectangular grid. In this research, the shapes of the cut cells include triangle, trapezoid and pentagon. The SIM with the Cut-cell approach (SIMCC) can handle the sharp discontinuity resulting from the interface formation, and can achieve higher accuracy (Ye et al. 2004, Tai and Shyy 2005). Among the Eulerian-Lagrangian approaches, the SIMCC is the one with the best accuracy, especially for a solid boundary.

Figure 4-2 is an example of grid system handled by SIMCC. In Figure 4-2, the cells far away from the object are still rectangular shapes and only the cells near the interface are

modified to be non-rectangular shapes. It must be emphasized that the total number of cells will not change during the computation.

4.4 Sharp Interface Method with Cut-Cell Approach (SIMCC)

The SIMCC is adopted to solve the complex geometry in this research. For SIMCC, the underlying grid is a Cartesian grid which is cut by the explicit interfaces to form the cut-cells. The entire domain will be filled with these cut and regular cells. Most cells still keep the original shapes. The SIMCC utilizing the Cartesian grid and Cut-cell approach can be used to solve fluid flow and heat transfer problems involving multiphase and/or complex geometry with a high accuracy. Due to the algorithm and data management requirements the SIMCC is computationally intensive. Using SIMCC, the interface is constructed by a sequence of straight lines in the computational domain. Because the number of cells in SIMCC does not change during the computation, the matrix of coefficients of SIMCC is very similar to the curvilinear grid system. Only the coefficients of cut-cells have to be modified so that the convergent speed and characteristics are very close to the curvilinear system and so it converges much faster than the unstructured grid system.

For a complete set of SIMCC, there are four main procedures; the interfacial tracking, the merging procedure, the flux computations in the interfacial region and the moving interface algorithm for advancing the interface. For the interfacial tracking, the information of the interface should be input and reproduced and also the intersections between the interface and background grid must be located. These intersections will be the cut-points and used for the next step, the merging procedure. Because of the interface, some cells are cut and can not maintain the rectangular shape anymore and therefore have to be treated specially. Using a merging technique, the fragments of cells can be merged by neighboring cells or larger fragments to form cut-cells. This means the cells around the interface have to be reconstructed. For the third

procedure, the cut-cells around the interface may be in the form of a triangle, trapezoid or pentagon. A special interpolation scheme with higher order accuracy is required to handle the complicated cut-cells to get the accurate primary variables or derivatives at the center of a cell face. The original Cartesian grid will become a mixed grid which includes most rectangular and some non-rectangular grid. Figure 4-3 is an example of the mixed type grid.

For a fixed interface problem such as flow over a sphere, the above three techniques are enough. If the interface is not fixed but moving, the moving interface algorithm will be necessary. In the moving interface algorithm, there will be two functions to perform:

- To advance the interface based on the force balance in the normal direction at interface.
- To refresh the cell because of change of phase.

By these four techniques, the SIMCC can be used to solve the moving interface problem.

4.4.1 Interfacial Tracking

During this procedure, marker points are used to describe the initial position of the interface. As shown in Figure 4-4(A), a sequence of marker points is given initially. In this oblique ellipse case, there are 50 initial markers. These markers must be represented by a polynomial curve fitting method; also, the distance between two adjacent markers have to be adjusted based on the curve fitting method. For this research study, a quadratic curve fitting (Chapra and Canale 2002) is used so that the distance between two neighboring markers can not be too long and is set to $dx/2$ to maintain the shape of the object. After the curve fitting, a new sequence of markers with an equal distance from each other is obtained as shown in Figure 4-4(B). The number of markers is increased to 68.

The location of markers are stored as function of the arc length and represented by a sequence of quadratic functions. The intersections of the interface and the background grid are

shown in Figure 4-5. These intersections represent the cut points of the cut-cells. With this information, the normal vector of cut-side can be calculated.

Besides the marker points, all the primary values at interface are stored by the quadratic curve fitting also and can be represented by

$$\phi = a_{\phi}s^2 + b_{\phi}s + c_{\phi} \quad (4-10)$$

The coefficients in Equation 4-10 can be obtained by any three points which construct a section of quadratic curve. Any quantities located at this quadratic curve can be obtained by Equation 4-10.

4.4.2 Merging Procedure

In this study, the interface is represented by a series of piecewise quadratic curves. The governing equations will then be solved in regions separated by the interface, and the communication between these regions is facilitated by the interfacial conditions. Figure 4-6 illustrates the formation of interfacial cells where cells 1 to 4 are cut by an interface. According to the present Cut-cell approach, the segments of an interfacial cell not containing the original cell center are merged by their neighboring cells; the segments containing the original cell center are given the same index as the original cell. For example, in Figure 4-6, the upper segment of cell 3 is merged into cell 5 to form a new trapezoid cell. The fraction of cell 3 with cell center becomes a new independent trapezoid cell. The main segment of cell 1 that contains the original cell center will merge the small segments of cells 4 and 2 to form a new triangular cell. The remaining segment of cell 4 containing its original cell center now becomes an independent pentagonal cell. With these cut-and-merging procedures, the interfacial cells are reorganized along with their neighboring cells to form new cells with triangular, trapezoidal, and pentagonal shapes in a 2D domain. Figure 4-6 shows an example of the cut-cells after reconstruction.

Basically, when the area of a segment is less than 0.5 area of a normal cell, it will be merged.

After this procedure, each newly defined cell maintains a unique index and cell center to support the needed data structure. Of course, in a 3D domain, the situation will be more complicated, and will not be discussed here.

Figure 4-7 are two examples of cut-cells of different objects. The objects here are an airfoil (NACA0012) and a star shape. Figure 4-8 is another example to illustrate that the cut-cells of the different grid sizes. In Figure 4-8(A), the grid size is 0.025 and 4-8(B) is 0.1. In this case, the number of cut-cells of a fine grid is larger than that in a coarse grid. It can be seen that the object is represented more accurately in a fine grid than a coarse grid.

4.4.3 Flux and Stress Computations in the Interfacial Region

In Figure 4-9, it represents a Cartesian grid with nine cells cut by an interface. The solid squares mean the centers of cells. Because of the interface, the original $ACDF$ cell with the cell center 1 will absorb the fragment from another cell to form a trapezoidal $BCDE$. The original grid line \overline{AF} is replaced by a section of interface \overline{BE} and the original faces \overline{DF} and \overline{AC} are extended to become \overline{DE} and \overline{BC} .

In the finite volume framework, the fluxes (first order derivative) at cell faces and the primitive variables at face centers must be known for the surface integration purpose. Therefore, how to obtain the highly accurate fluxes and primitive variables is very important in SIMCC.

To consider a flux f across a cell face \overline{BC} in Figure 4-9, one can construct a second-order accurate integration procedure as follows:

$$\int_{BC} f dy = \int_{BA} f dy + \int_{AC} f dy \approx f_{BA}(y_A - y_B) + f_{AC}(y_C - y_A) \quad (4-11)$$

where f_{BA} and f_{AC} are computed at the centers of segments \overline{BA} and \overline{AC} , respectively. Getting the value of f_{AC} is straightforward. If f_{AC} is the flow variable ϕ , a linear interpolation can be used, yielding a second-order accuracy. The relation can be expressed as

$$\phi_{CA} = \phi_1 \lambda_1 + \phi_3 (1 - \lambda_1) \quad (4-12)$$

$$\lambda_1 = \frac{x_1 - x_{AC}}{x_1 - x_3} \quad (4-13)$$

If f_{AC} represents the normal gradient of flow variable ϕ , it can be approximated by the following central difference scheme as

$$\left(\frac{\partial \phi}{\partial x} \right)_{AC} = \frac{\phi_1 - \phi_3}{x_1 - x_3} \quad (4-14)$$

Equations 4-12 to 4-14 can not be used to estimate f_{BA} , because the neighboring cell centers are located in a region on the other side of the interface. Also, the center of segment \overline{AB} is not located on the straight line connecting the two cell centers. In order to maintain a second-order accuracy, a two-dimensional polynomial interpolating function is adopted in the computation of ϕ for such kind of small segments. An appropriate functional form for ϕ that is linear in X direction and quadratic in Y direction is given as

$$\phi = c_1 xy^2 + c_2 y^2 + c_3 xy + c_4 y + c_5 x + c_6 \quad (4-15)$$

the six coefficients, c_1 to c_6 , can be obtained from ϕ values at the six points (1 to 6) in Figure 4-9 ; thus the variable ϕ at the center of \overline{AB} can be expressed as

$$\phi_{AB} = c_1 x_{AB} y_{AB}^2 + c_2 y_B^2 + c_3 x_{AB} y_{AB} + c_4 y_{AB} + c_5 x_{AB} + c_6 \quad (4-16)$$

The normal gradient $\left(\frac{\partial \phi}{\partial x} \right)_{AB}$, which is often needed while computing the interfacial condition, can be obtained by

$$\left(\frac{\partial\phi}{\partial x}\right)_{AB} = c_1 y_{AB}^2 + c_3 y_{AB} + c_5 \quad (4-17)$$

Similar approach is used to compute the flow variables or their normal gradients on the remaining segments.

Once the primary variables and the derivatives at the cut side are determined, the coefficients of matrix for the cut-cells can be modified based on this information and the matrix solver will be called to obtain the solution. It must be emphasized that Equation 4-17 is only for \overline{AB} in this case. Here, the y terms are up to second order while the terms in x are linear. That means this interpolation polynomial is “quadratic” in Y direction and “linear” in X direction. For a more complicated case, a higher power polynomial may be needed but the order will not exceed two in either x or y .

4.4.4 Moving Interface Algorithm

For the fixed interface problems, the techniques discussed from Section 4.4.1 to 4.4.3 constitute all the elements required to obtain the solutions. However, for most problems in multiphase flows, the interface is not fixed and therefore a moving interface algorithm is necessary. The moving interface algorithm in this research includes two functions. The first one is to advance the interface (Ryskin and Leal 1984) and the second one is to update the cells because of change of phase (Udaykumar et al. 1997).

4.4.4.1 Advancing the Interface

In the unsteady multiphase computation, the interface will advance to satisfy the interfacial dynamics in each time step. In SIMCC, a “push and pull” strategy is used to determine the new location of an interface and also to satisfy the force balance at the interface. The forces acting at the interface can be resolved into the normal and tangential components. In multiphase flow computation, the order of magnitude of the normal force is much larger than that of the

tangential force and therefore the displacement of interface is governed basically by the normal forces at the interface. In this “push and pull” strategy, only the normal component of force balance is considered on the interface and the new location of interface will be determined by a series of iterations. In each iteration, the residual of the force balance in the normal direction will be computed and the displacement of marker points is assumed proportional to this residual:

$$\begin{aligned} X_{new}^{n+1} &= X_{new}^n + \beta \cdot \Pi^{n+1} \cdot n_x \\ Y_{new}^{n+1} &= Y_{new}^n + \beta \cdot \Pi^{n+1} \cdot n_y \end{aligned} \quad (4-18)$$

where (X, Y) is the coordinates of marker points, (n_x, n_y) is the components of normal vector in the X and Y direction, respectively. Π is the residual of the force balance in the normal direction and β is a relaxation factor and it is an empirical value normally in the range of 0.1-0.001 in this research.

Figure 4-10 is an illustration for this interfacial advancing process. In Figure 4-10, a marker point A_0 is located at the initial interface and the residual of force balance in the normal direction Π_1 will be computed. Based on the location of A_0 and the value of Π_1 , the marker point A_0 will be pushed to A_1 . In this moment, the residual of force balance in the normal direction will be checked. If the new residual Π_2 is still large, the marker point A_1 will be pushed to A_2 . Once the residual is small enough, i.e., the force balance in the normal direction achieves convergence, the interaction will be stopped and the normal component of interfacial velocity can be determined by

$$\begin{aligned} (u_n)_{x_int_new} &= (X_{new} - X_{old}) / \Delta t \\ (u_n)_{y_int_new} &= (Y_{new} - Y_{old}) / \Delta t \end{aligned} \quad (4-19)$$

In this iterative procedure, the residual of the force balance in the normal direction is required to be less than 1.0E-3. The normal component of the interfacial velocity will be the

velocity boundary condition during the computation. This algorithm is only for the problems without phase change. Once there is phase change, Equation 4-19 must be modified to include the effect from phase change.

4.4.4.2 Updating the Cells

After the interface is adjusted, some cells will change their phases. In Figure 4-11, the phase of cell center A is different from cell centers a, b, c and d initially. Once the interface advances to the new location, the phase of cell center A will change. In this case, the fluid properties of cell center A will change also such as the discontinuous primary variable of pressure. In this research, the new primary variables at the cell center A can be obtained by following steps:

- Select a point B on the new interface such that the line connecting A and B is normal to the interface. Point B is located at the interface and therefore, the primary variables of point B can be determined by interfacial conditions.
- In this normal direction, find another point C such that the distance between B and C is $1.5\Delta x$.
- Find four cell centers a, b, c and d and point C is surrounded by them. To use cell centers a, b, c and d and the bilinear interpolation method to find the primary variables at point C.
- Use linear interpolation to obtain the primary variables at cell center A using the primary variables at points B and C.
- Update the fluid properties of cell center A.

4.5 Issues of Phase Change Computation in Cartesian Grid Methods

In this research, the phase change phenomenon is one of the key elements. In a cryogenic two-phase flow, the temperature at pipe wall or tank is much higher than the saturation temperature so that the phase change phenomenon at liquid-gas interface is inevitable. The phase change phenomenon is very common in engineering applications. For the phase change computation, the most important issue is to obtain the accurate mass transfer rate generated from

the interface due to the vaporization and this will rely on the accurate heat flux computation near the interface.

In recent Cartesian grid methods, except the Sharp Interface Method, most of them adopt the continuum surface force model (CSF) (Brackbill et al. 1992, Shyy and Narayanan 1999) to include the surface tension in the momentum equation. By CSF, the surface tension can be modeled as a source term in the momentum equation (Sussman et al. 1994, Lörst ad and Fuchs 2004, Zhang et al. 2006). In addition, the continuity and energy equations may need to be modified by adding extra source terms to include the effect of discontinuity such as mass transfer rate at interface. The fluid properties of different phase are described by a so-called indicator or Heaviside function (Dhir 2001). Therefore, only one set of governing equation is solved and there will be a smeared band of the solution across the interface. The resolution of primary variables must be poor near the interface.

In Juric and Tryggvason's (1998) and Shin and Juric's (2002) work, they used the Front Tracking Method to simulate the film boiling phenomena. In their researches, the interfacial velocity u_{int} is obtained by the following equations:

$$u_{\text{int}} \cdot \bar{n} = \frac{(\dot{m}'' + (\rho u)_f \cdot \bar{n})}{\rho_f} \quad (4-20)$$

where $\rho_f = \frac{\rho_l + \rho_g}{2}$ and u_f can be treated as an average of the velocity of liquid and gas phases near the interface.

Then, the interface is advanced by following equation.

$$\frac{dx}{dt} \cdot \bar{n} = \left(u_f + \frac{\dot{m}''}{\rho_f} \right) \cdot \bar{n} \quad (4-21)$$

Also, this interfacial velocity will be used to form the source term in the continuity equation:

$$\nabla \cdot \mathbf{u} = f(u_{\text{int}}) \quad (4-22)$$

This set of equations looks safe in mathematic but in fact, it is very dangerous in real physics. The trouble will come from the interpolation for u_f . Once phase change is very strong such as large Jakob number or large density ratio, the velocity jump at interface will be very large. With large velocity jump, u_f will be inaccurate and the error may be very huge. For example, if $u_l=1.0$ and $u_g=100$, u_f will be close to 50.5 by the interpolation and this will cause huge error. Therefore, this set of equations can be applied only when the phase change is very weak or low density ratio otherwise, the conservation of mass will be very inaccurate.

In some researches about phase change by Level Set Method such as Morgan's (2005), Son and Dhir's (1998) and Son's work (2001), in order to include the volume change at liquid-gas interface, they modified the continuity equation as

$$\nabla \cdot \bar{\mathbf{u}} = f(\nabla H) \quad (4-23)$$

where H is a smooth step Heaviside function. By this Heaviside function, the fluid properties near the interface will be treated as continuous with 3 grid space distance. Obviously, once the density jump is small, this modified continuity equation may be able to handle the mass flux generated from the liquid-gas interface. However, once density jump is very large, the conservation of mass will be inaccurate. In the general condition, the density jump between liquid and gas is on the order about 1000.

In Front Tracking and Level Set Method, there are always the errors of mass because the variables and properties are treated as continuous across the interface and this does violate the real physics. In real situation, the properties of fluids are not continuous across the interface. If there is no phase change, the pressure should be discontinuous across the interface. With phase change, both pressure and velocity should not be continuous across the interface.

To simulate the phase change phenomenon, the most important thing is to obtain accurate heat fluxes across the interface. These accurate heat fluxes will be transferred to be used as latent heat of vaporization for the liquid. In numerical simulations, in order to acquire the accurate heat flux at the interface, the temperature distribution must be very accurate and grid must be very fine near the interface. Also, some information about the interface must be explicit such as the normal direction unit vector and the length of the interface. Generally speaking, in order to evaluate the heat flux accurately, three conditions must be satisfied: an accurate temperature distribution near the interface, an accurate numerical method to find the temperature derivative at the interface and enough information about the interface.

In the Cartesian grid method, only SIMCC can satisfy these three conditions. In SIMCC, there is no smeared band near the interface and the interface is an explicit true surface. Table 4-1 lists the key issues for the heat flux computation in some popular Cartesian grid methods.

Based on Table 4-1, the SIMCC is the only method that can obtain the heat flux at interface accurately. In SIMCC, the governing equations of each phase are solved separately and there is no smeared band that distorts the actual temperature profile. Therefore, the accurate normal direction can be obtained easily and also it is easy to calculate the area of the surface of interface. This information will be very useful for evaluating the latent heat supply for the phase change. Based on these advantages of the SIMCC, therefore, SIMCC is selected to be the numerical scheme in this research.

4.6 Heat Flux Computation at the Interface

In order to evaluate the heat flux accurately, the following conditions must be satisfied:

- Accurate temperature fields near the interface.
- Accurate information of the interface.
- Accurate numerical method to find the temperature derivative at the interface.

In SIMCC, the first condition can be satisfied easily. The interface is treated as a true surface and there is no smeared band at the interface. Because the interface exists explicitly in SIMCC, the information such as the location of the interface and the unit normal vector at the interface can be obtained easily and therefore, the second condition is also satisfied. Figure 4-12 illustrates the numerical technique to evaluate the heat flux in this research.

For each marker point, two probing points are selected. These two marker points are located in the direction of the normal vector of the interface with an equal distance. The distance from the marker point to the nearest probing point is determined by the code. The rule is that any nearest probing point can be surrounded by four cell centers in the same phase. As shown in Figure 4-12, probing point 1 is surrounding by cell centers 1, 2, 3 and 4 and probing point 2 is surrounding by cell centers 4, 5, 6 and 7. Once the four points are selected, the second order accurate bilinear interpolation method can be used to obtain the temperature at probing points 1 and 2. In a cryogenic flow, because the temperature of the pipe is always higher than the saturation temperature, the temperature at the interface should be equal the saturation temperature. This type of interfacial condition is also called the Dirichlet type and the value should be a fluid property. By the temperatures at the interface and at the two probing points, Taylor expansion can be used to obtain the second order accurate temperature gradient:

$$\frac{\partial T_{\text{int}}}{\partial n} = \frac{4T_{\text{probe}_1} - 3T_{\text{int}} - T_{\text{probe}_2}}{2\Delta x} + O(\Delta x^2) \quad (4-24)$$

All the techniques in this section including those for obtaining temperatures at cell centers and the bilinear interpolation method are of second order accuracy. It can be expected that the temperature gradient at the interface can achieve at least second order accuracy also.

Here, the accuracy of the current probing point method for heat flux and latent heat computation will be evaluated by a sample test case. The geometry of this test case is a rectangle

with dimensions of 5×10 and a fictitious interface, a half-circle with a radius $R=0.5$ is placed on the bottom with the center at $(5, 0)$. The coordinate system is axisymmetric. The heat flux and latent heat at the surface of this object will be tested based on two sets of grids and assumed temperature profiles. Figure 4-13 is an illustration of the geometry of this test case.

The two selected grids are 64×64 and 128×128 . Two sets of assumed temperature profiles are: $T = r$ and $T = r^2$ with the original point $(5,0)$. Figure 4-14 is the assumed temperature distribution.

In this test case, there will be several exact solutions which can be used for validation:

- The area of this sphere should be: $A = 4\pi r^2 = \pi = 3.1415926$
- The temperature gradient of each temperature distribution is : $\partial T / \partial r = 1$ at $R=0.5$
- The latent heat can be computed by $\int \dot{q}'' dA dt$

If thermal conductivity is assumed as 1.0 and time step is also 1.0, there will be the exact solution of latent heat in one time step:

$$\lambda = q \times A \times \Delta t = 1 \times \pi \times 1 = \pi \quad (4-25)$$

Table 4-2 lists the computed result and corresponding error.

By Table 4-2, it shows that the current method for latent heat computation is reliably accurate at least for a quadratic temperature profile and the profile can be improved when the grid size becomes smaller.

4.7 Phase Change Algorithm

In this research, because of the large temperature difference, the phase change phenomenon is inevitable so that the mass flow rate at the interface can not be zero. In order to truly satisfy the conservation of mass at the interface, a “discontinuous” model is adopted.

In SIMCC, the normal component of interfacial velocity is determined by the interfacial displacement over Δt and the contribution of normal component of interfacial velocity should come from both normal force balance condition and phase change:

$$(u_n)_{\text{int}} = \frac{\Delta x_{\text{force_balance}} + \Delta x_{\text{phase_change}}}{\Delta t} \quad (4-26)$$

where $\Delta x_{\text{phase_change}}$ is the contribution comes from the phase change and the normal component of interfacial velocity can be expressed as

$$(u_n)_{\text{int}} = (u_n)_{\text{force_balance}} + (u_n)_{\text{phase_change}} \quad (4-27)$$

By conservation of mass at interface and Equation 4-27, the normal component of the velocity near the interface of each phase can be obtained and they will be the velocity boundary condition for each phase. This is the so-called “discontinuous” model in this research. In this model, the velocities of each phase come from the conservation of mass at the interface and are discontinuous at the interface. Therefore the conservation of mass at the interface can be enforced.

Based on this idea, a phase change algorithm is developed in this research that includes the following steps:

- Computation of heat flux at the interface locally.
- Computation of the corresponding mass transfer rate.
- Integration of the mass transfer rate by time and surface area to obtain the total latent heat and then divided by the unit latent heat to obtain the amount of vaporization.
- Adjust the interface based on the amount of vaporization.

Heat flux computation with second order accuracy has already been addressed in the previous section; the rest of the steps will be discussed here.

The local total heat flux can be expressed as

$$\dot{q}'' = k_g \frac{\partial T_g}{\partial n} - k_l \frac{\partial T_l}{\partial n} + \dot{q}_{rad}'' \quad (4-28)$$

Then the net heat passes the interface locally in one Δt for one ΔA should be:

$$e = \dot{q}'' \Delta A \Delta t \quad (4-29)$$

This amount of energy should be transferred to be the latent heat locally, the local mass transfer can be obtained by

$$m_{transfer} = e / \lambda \quad (4-30)$$

When the local mass transfer is counted, the interface will be adjusted by this local mass transfer. During the adjustment procedure, the reference coordinate should be fixed at the interface and the normal and tangential directions are two axis of this coordinate. Then, the new interface can be redefined as

$$\begin{aligned} X_{phase_chang} &= X_o + \beta \cdot n_x \\ Y_{phase_chang} &= Y_o + \beta \cdot n_y \end{aligned} \quad (4-31)$$

where β is the local mass transfer coefficient and can be calculated by the local mass transfer.

Figure 4-15 shows algorithm of this step.

Now, a new interface based on the phase change is defined. The next step is to call the isothermal moving interface algorithm. Because of the imbalance of force in the normal direction, the new interface will be adjusted again to achieve balance of force in the normal direction and it is the final interface of each time step.

$$\begin{aligned} X_{new} &= X_{phase_change} + \beta \cdot \Pi \cdot n_x \\ Y_{new} &= Y_{phase_change} + \beta \cdot \Pi \cdot n_y \end{aligned} \quad (4-32)$$

The idea behind this equation is the same as the isothermal case. The difference is that in Equation 4-32 an initial displacement due to the phase change has already been counted before the iteration starts. Figure 4-16 shows the algorithm of this step.

In each time step, the total displacement of interface should be the difference between the original interface and the final new interface. Therefore, the new normal component of interfacial velocity can be obtained by

$$\begin{aligned}(u_n)_{x_int_new} &= (X_{new} - X_{old}) / \Delta t \\ (u_n)_{y_int_new} &= (Y_{new} - Y_{old}) / \Delta t\end{aligned}\tag{4-33}$$

where $(u_n)_{x_int_new}$ and $(u_n)_{y_int_new}$ represent the X and Y component of normal component of interfacial velocity for next time step.

In SIMCC, if there is no phase change, the normal component of interfacial velocity will be the velocity boundary condition of each phase and this is the same as continuous model. However, because of phase change, the interfacial velocity must be modified to satisfy the conservative law. In this research, the velocity boundary at interface will be corrected by the mass conservation as

$$\begin{aligned}(u_n)_l &= \frac{(\rho_l (u_n)_{int}) + \dot{m}''}{\rho_l} \\ (u_n)_g &= \frac{(\rho_g (u_n)_{int}) + \dot{m}''}{\rho_g}\end{aligned}\tag{4-34}$$

The two discontinuous normal components of interfacial velocities will be used to be the velocity boundary of each phase and this so-called “discontinuous” model in this research.

In Equation 4-34, it is very clear that if there is no phase change, it will reduce to

$$(u_n)_g = (u_n)_{int_g} = (u_n)_{int} = (u_n)_{int_l} = (u_n)_l\tag{4-35}$$

Therefore, the continuous model is a special case of the discontinuous model when there is no phase change. Figure 4-17 is the detailed flow chart of this step.

4.8 Global Conservation of Mass

The major difference between the current SIM and others' work is that SIM can better preserve the global conservation of mass. During numerical simulation, it is inevitable that the errors of mass will be generated by improper initial conditions or the inherent numerical errors especially in internal flows. In order to preserve the global conservation of mass, a set of conservative strategies is applied.

For the gas phase, a correction of mass flow rate is applied at the outlet of the pipe. As shown in Figure 4-18, the inlet mass flow for the gas phase has contributions from two parts, the mass flow through the inlet and the mass flow generated at the interface. Therefore, the total mass flow rate into the gas phase should be:

$$\dot{m}''_{in} = \dot{m}''_{inlet} + \dot{m}''_{interface} = \int \rho u_{inlet} dA_{inlet} + \int \rho u_{int} dA_{int} = \dot{m}''_{out} \quad (4-36)$$

The mass flow which leaves the outlet is controlled by the boundary condition. If the boundary condition is unknown, usually, it can be done by higher order extrapolation or fully developed assumption once the pipe is long enough but this computed leaving mass flow rate may not equal to the mass flow rate entering the domain. Also, the errors of mass can be caused by an accumulation of numerical errors over the thousands of iterations that need to be done. Even if the mass flow rate at outlet is not accurate at beginning, an estimated value of mass flow at outlet can still be obtained:

$$\dot{m}''_{out_guess} = \int \rho u_{out_bc} dA_{out} \quad (4-37)$$

By the idea of conservation of mass, the entering mass flow rate should equal the mass flow rate at the outlet if the flow is incompressible and there is no other mass source. Therefore, the velocity difference can be added at outlet:

$$u_{out} = u_{out_bc} + (\dot{m}''_{out} - \dot{m}''_{out_guess}) / (\rho A_{out}) \quad (4-38)$$

Finally, this u_{out} can be used to be the velocity boundary condition and the conservation of mass in the gas phase can be preserved.

The following provides the details of the conservation of mass scheme for the inflow of liquid phase. In Figure 4-19, the forward shaded region represents the liquid cylindrical core shape at the time step “ t ” that is the initial condition for the next time step. When advancing to the next time step “ $t + \Delta t$ ”, the total entering mass is known, Δm , which enters the pipe during the time step is equal to the velocity at the inlet multiplied by the time step size, Δt . The interim liquid core is composed of two parts as shown in Figure 4-20 by a forward slashed region and a backward slashed region. The forward slashed region in Figure 4-20 is made identical to that in Figure 4-19 except that it is moved downstream while the backward slashed region is the added mass Δm . So the total mass of the two parts will be the mass of liquid core at the time step “ $t + \Delta t$ ”. Even though the mass is conserved but the interface shape has not been updated, so it must be re-computed based on the interfacial conditions before we complete the “ $t + \Delta t$ ” step. In summary, by this strategy, the conservation of mass is strictly enforced and also, the phase interface is updated that follows the forced balance. The details on updating interface locations are based on the marker points and their movement as discussed next.

During the generation of the interim interface as shown in Figure 4-20, the locations of the markers have to be adjusted accordingly. In the current algorithm, the total number of markers will not change for the interim interface. As shown in Figure 4-21, the marker points 0, 1, and 3 represent all the markers on the old interface as. During the construction of the interim interface, as stated above, because of the added mass, the markers will have to move so that point 1 will move to 1', 2 to 2' and 3 to 3' in Figure 4-22, respectively. One important rule implemented here is that Point 0 that is anchored at the inlet for the old interface will become 0' for the interim

interface will not move with the old liquid core, so $0'$ remains at the inlet. As a result, the distance between $0'$ and $1'$ is larger than others that calls for re-structure and update the marker system with the a new set before proceeding with the determination of the final interface for time step " $t + \Delta t$ ".

Table 4-1. Comparison of the key issues for different numerical methods for the heat flux computation.

	VOF	Level Set	IBT	Front Tracking	SIMCC
Explicit interface	N	N	Y	Y	Y
Accurate near the interface	N	N	N	N	Y
Fine grid near the interface	N	N	N	N	N

Table 4-2. Comparison of exact and numerical results for the flow over sphere case.

	Grid 64x64	Grid 128x128
Area/ error	3.14/ 8.12E-4	3.14/ 1.93E-4
Latent heat /error, $T = r$	3.21/ 2.08E-2	3.19/ 1.38E-2
Latent heat /error, $T = r^2$	3.29/ 4.64E-2	3.22/ 2.57E-2

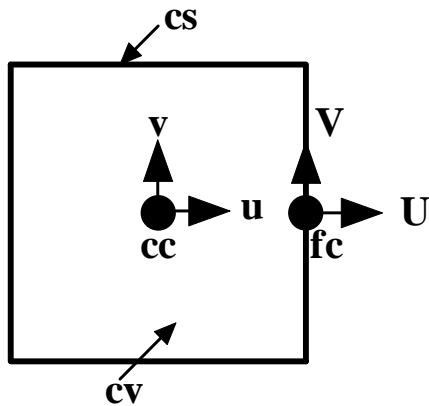


Figure 4-1. Non-staggered grid system.

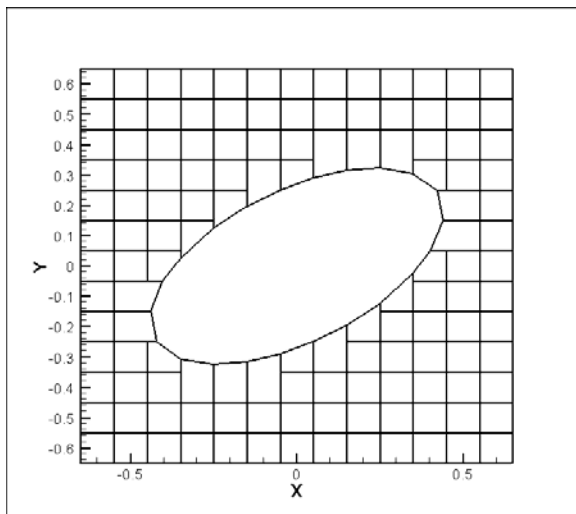


Figure 4-2. Example of mixed structured and unstructured grid in SIMCC.

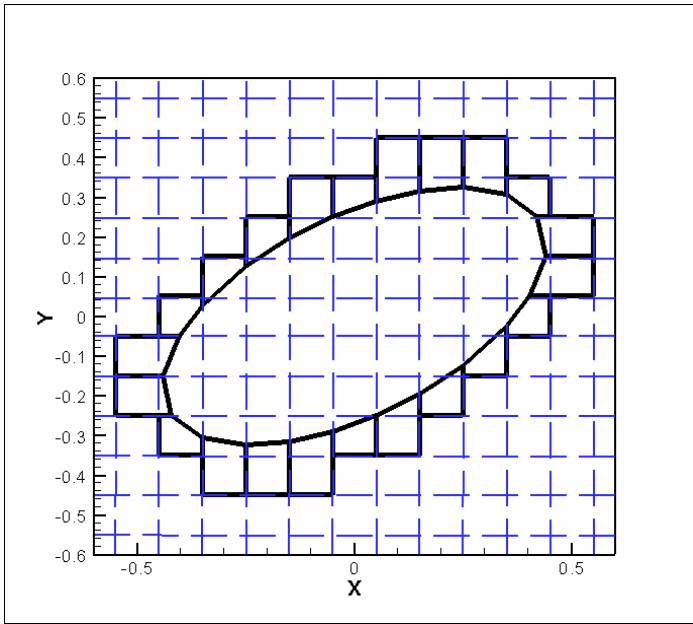


Figure 4-3. Example of mixed structured and unstructured grid.

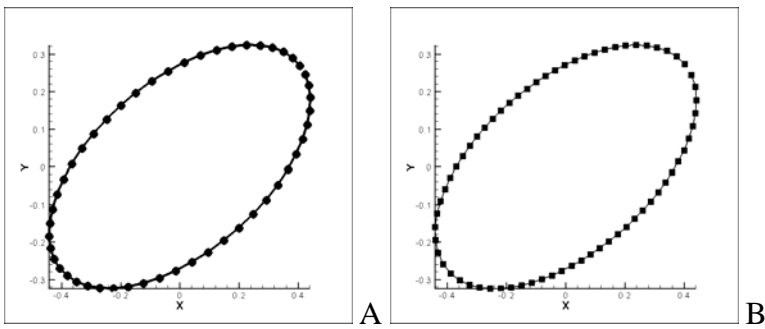


Figure 4-4. Marker points of an oblique ellipse. A) initial ,B) after curve fitting.

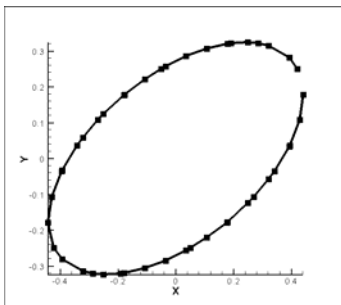


Figure 4-5. Intersection points of an oblique ellipse.

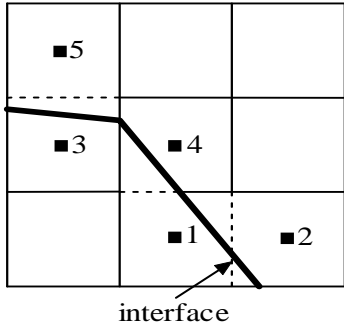


Figure 4-6. Illustration of the interfacial cells and cut-and-absorption procedures in the SIMCC in local situation.

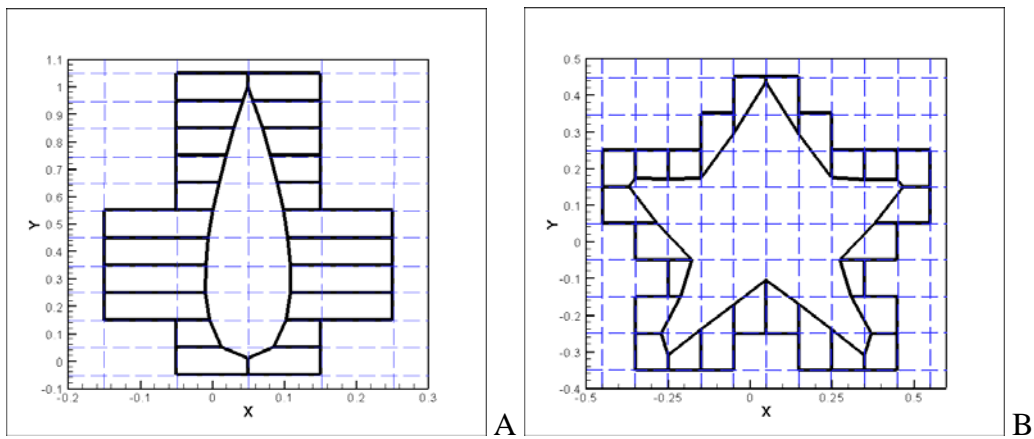


Figure 4-7. Cut-cells of different objects. A) NACA0012, B) Star shape.

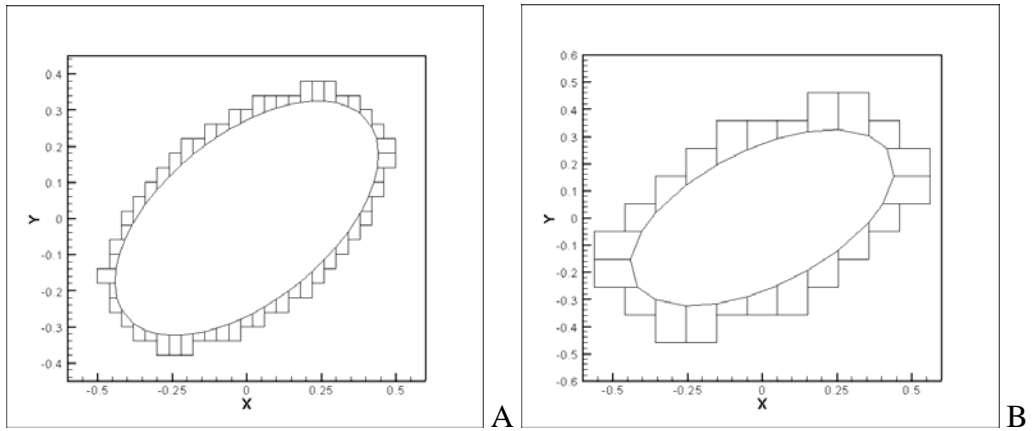


Figure 4-8. Example of cut-cells of different grids. A) $dx=0.025$, B) $dx=0.1$.

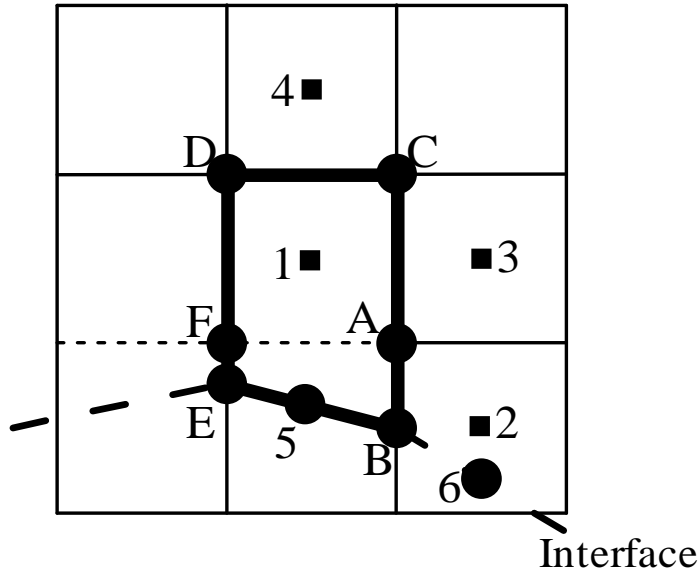


Figure 4-9. Illustration of the interfacial variables and notation.

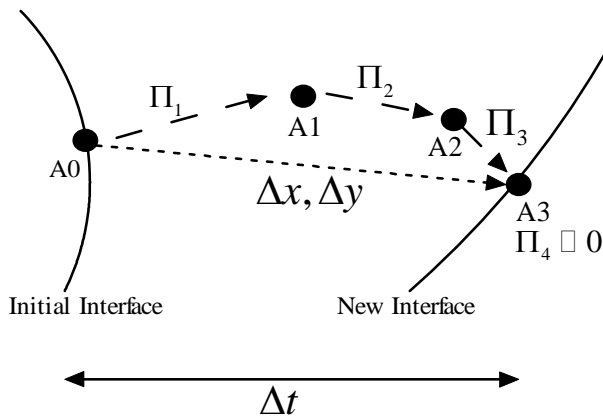


Figure 4-10. Illustration of interfacial advancing process.

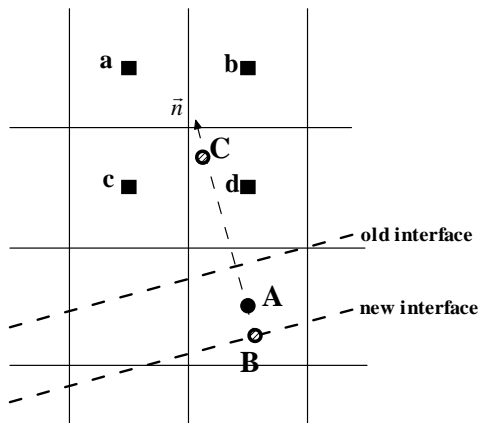


Figure 4-11. Illustration of updating cell procedure.

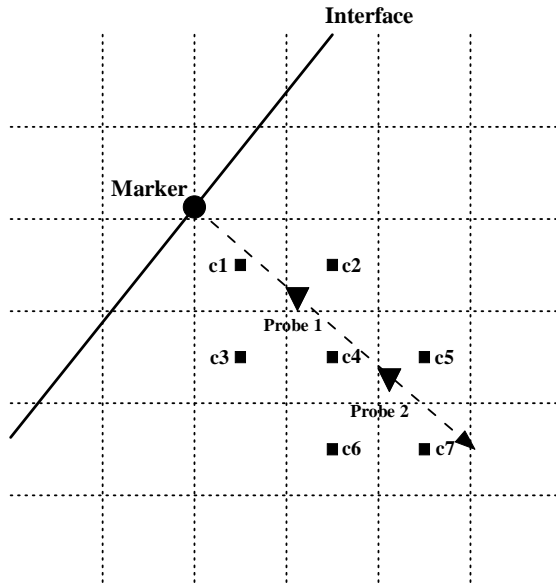


Figure 4-12. Two probing points for second order gradient.

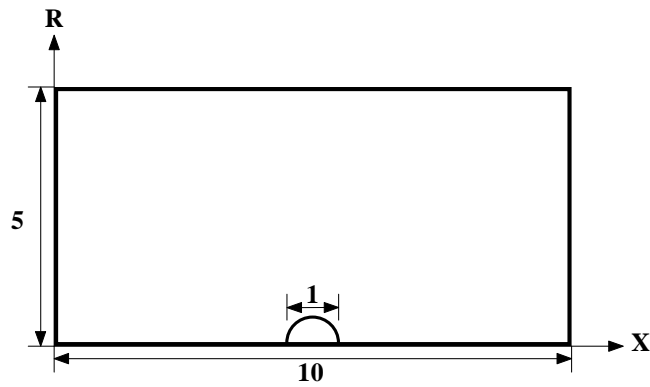


Figure 4-13. Illustration of geometry of test domain.

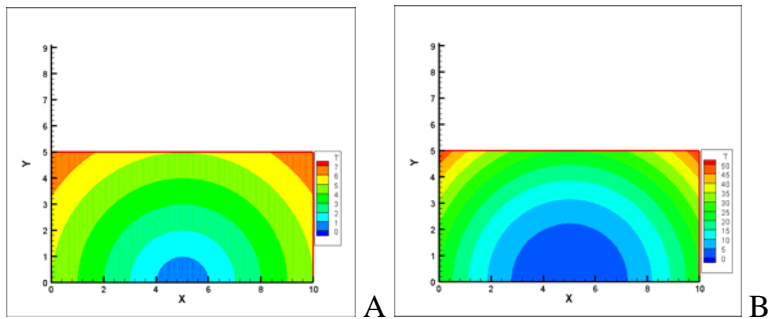


Figure 4-14. The assumptive temperature distribution. A) $T = r$, B) $T = r^2$.

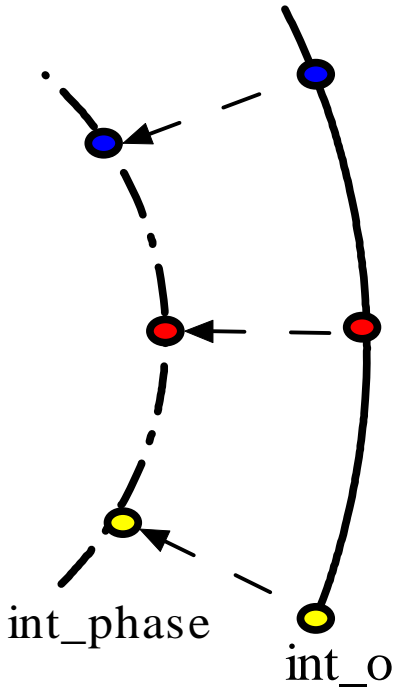


Figure 4-15. The new interface because of phase change.

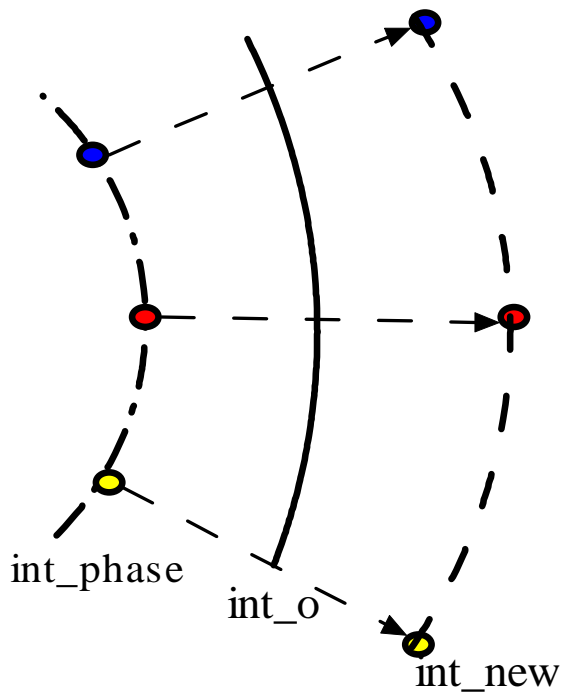


Figure 4-16. The new interface because of balance of force.

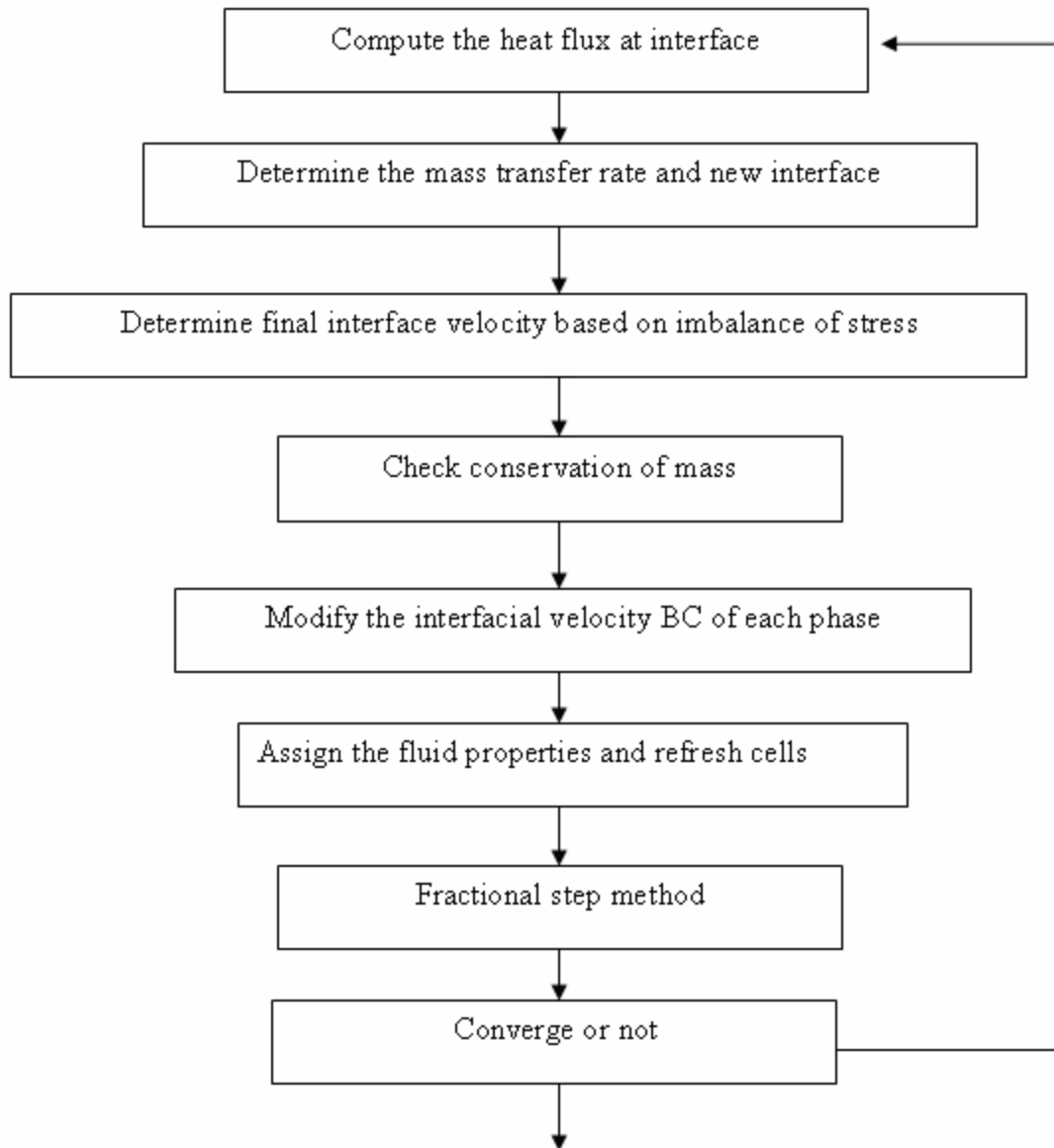


Figure 4-17. The flow chart for the phase change algorithm.

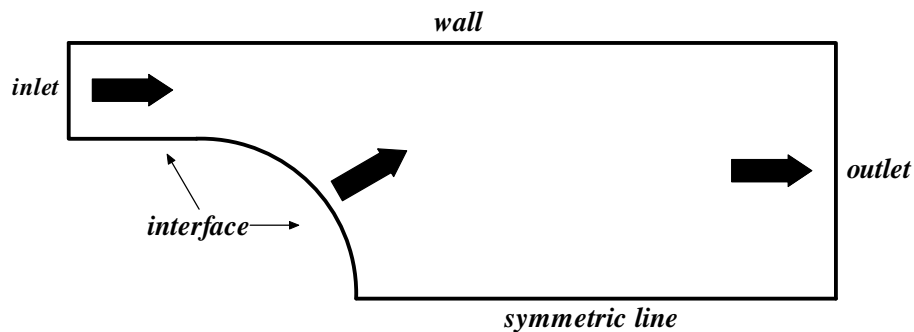


Figure 4-18. The global conservation of mass in gas phase.

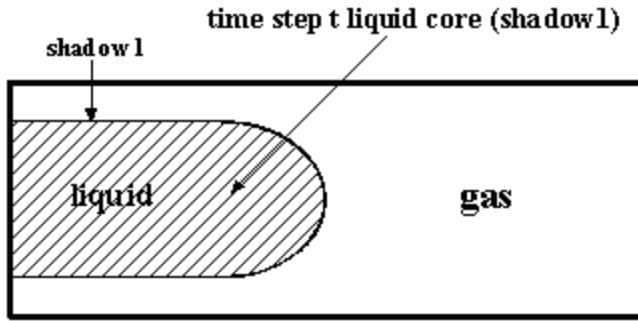


Figure 4-19. Interim interface construction, the initial interface.

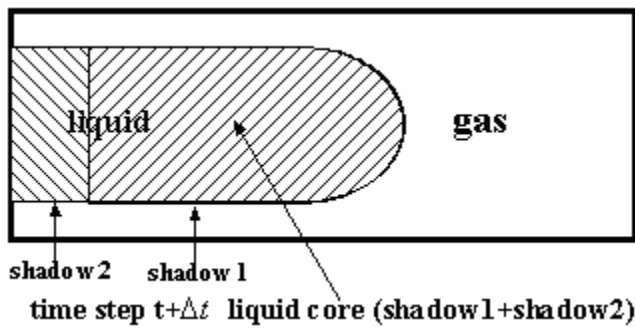


Figure 4-20. Interim interface construction, the new interface.

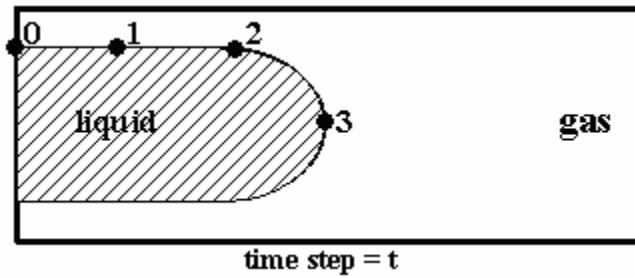


Figure 4-21. Re-structuring of markers, the original markers.

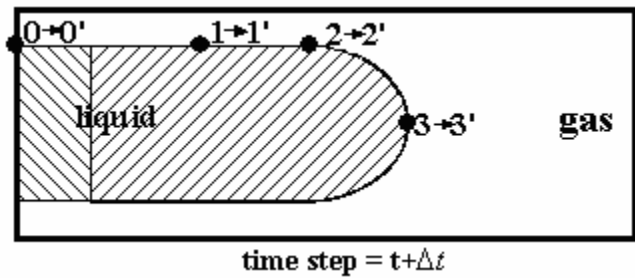


Figure 4-22. Re-structuring of markers, the new markers.

CHAPTER 5 VALIDATION OF CODE

5.1 Introduction

In this chapter, several test cases with known solutions are used to validate the SIMCC code. They are divided into three groups based on the aspects of the numerical techniques. The first group is used to validate the solver of the governing equations and the SIMCC with the fixed interface and includes the Couette flow, fully developed channel flow, cavity flow, fully developed flow in a pipe with a constant wall heat flux and flow over a sphere cases. The second group focuses on the moving interface algorithm and includes the static droplet, the rising bubble and droplet simulations. The last group focuses on the mass transfer at the interface and includes a stationary droplet in a quiescent medium with constant mass transfer rate and the one dimensional phase change problem.

5.2 Group 1, Solver of Governing Equations and the SIMCC with the Fixed Interface

In this group, the interface will not be moving but fixed in the domain and this can help to validate some numerical techniques applied in the SIMCC code, such as the solver of governing equations, the interfacial tracking, merging procedure and the flux and stress computations at the interface.

5.2.1 The Fictitious Interface for Evaluating the SIMCC

In order to validate the SIMCC while taking advantage of known analytical solutions and well-accepted benchmark cases, the entire flow field is divided into two regions separated by a fictitious interface. By comparing the solutions obtained using the fictitious interface with the known solutions, the performance and accuracy of the SIMCC can be evaluated. Detailed treatment of the fictitious interface is given below. As shown in Figure 5-1, since region 1 and region 2 are the same fluid, the normal stress balance at the fictitious interface is:

$$\sigma_1 = \sigma_2 \quad (5-1)$$

The shear stress balance at the fictitious interface is:

$$\tau_1 = \tau_2 \quad (5-2)$$

Continuity of the flow variables at the fictitious interface yields:

$$u_{x1} = u_{x2} \quad (5-3)$$

$$u_{y1} = u_{y2} \quad (5-4)$$

$$p_1 = p_2 \quad (5-5)$$

It should be emphasized that with an interface that separates two different phases, the interfacial conditions will not be the same as the ones listed above.

Furthermore, the normal and shear stress at the fictitious interface can be expressed by the stress tensors:

$$\sigma_1 = \vec{n} \cdot \vec{\vec{T}}_{A_1} \cdot \vec{n} = \vec{n} \cdot \vec{\vec{T}}_{A_2} \cdot \vec{n} = \sigma_2 \quad (5-6)$$

$$\tau_1 = \vec{n} \cdot \vec{\vec{T}}_{A_1} \cdot \vec{t} = \vec{n} \cdot \vec{\vec{T}}_{A_2} \cdot \vec{t} = \tau_2 \quad (5-7)$$

The stress tensor at point A in Figure 5-1, $\vec{\vec{T}}_A$, on the interface from either region can be written as

$$\vec{\vec{T}}_{A_1} = \begin{bmatrix} -p + 2\mu_1 \frac{\partial u_{x1}}{\partial x} & \mu_1 \frac{\partial u_{x1}}{\partial y} + \mu_1 \frac{\partial u_{y1}}{\partial x} \\ \mu_1 \frac{\partial u_{x1}}{\partial y} + \mu_1 \frac{\partial u_{y1}}{\partial x} & -p + 2\mu_1 \frac{\partial u_{y1}}{\partial y} \end{bmatrix}_{A_1} \quad (5-8)$$

$$\vec{\vec{T}}_{A_2} = \begin{bmatrix} -p + 2\mu_2 \frac{\partial u_{x2}}{\partial x} & \mu_2 \frac{\partial u_{x2}}{\partial y} + \mu_2 \frac{\partial u_{y2}}{\partial x} \\ \mu_2 \frac{\partial u_{x2}}{\partial y} + \mu_2 \frac{\partial u_{y2}}{\partial x} & -p + 2\mu_2 \frac{\partial u_{y2}}{\partial y} \end{bmatrix}_{A_2} \quad (5-9)$$

The normal and tangential unit vectors at point A can be evaluated using analytical formulas:

$$n_{x,A} = -\frac{y_A}{(x_A^2 + y_A^2)^{1/2}} \quad (5-10)$$

$$n_{y,A} = -\frac{x_A}{(x_A^2 + y_A^2)^{1/2}} \quad (5-11)$$

$$t_{x,A} = -n_{y,A} \quad (5-12)$$

$$t_{y,A} = n_{x,A} \quad (5-13)$$

For the fictitious interface case, \bar{T}_{A_1} should be equal to \bar{T}_{A_2} ,

It is obvious that the normal and shear stresses should be a function of \bar{u}_A and P_A . So there are two nominal equations but three unknowns. The following is a complete procedure to evaluate the interfacial conditions.

First, the pressure at each marker point is determined by the bilinear and central difference interpolations. As shown in Figure 5-2, two imaginative points B and C, normal and equidistant from point A are defined first. Because the shape of background cells is always rectangular, there must be four cell-centers surrounding each of the points B and C. The pressures at points B and C can be determined by bilinear interpolation. Once the pressures at points B and C are obtained, central differencing can be applied to estimate the pressure at point A with second-order accuracy.

The derivatives of velocity in Equation 5-8 and 5-9 can be determined by the Taylor series expansion:

$$f(x + \Delta x, y + \Delta y) = f(x, y) + [f_x(x, y)\Delta x + f_y(x, y)\Delta y] + \frac{1}{2}[f_{xx}(x, y)\Delta x^2 + 2f_{xy}(x, y)\Delta x\Delta y + f_{yy}(x, y)\Delta y^2] + O(\Delta x^3) \quad (5-14)$$

The procedure is similar to determining the pressure at point A. As shown in Figure 5-3, eight imaginative points must be chosen first. By the bilinear interpolation, the velocity on each imaginative point can be determined.

The derivatives of velocity, for example, $\frac{\partial u_x}{\partial x}$ term in Equation 5-8 can be expressed using

Taylor series expansion as

$$\frac{\partial u_x}{\partial x} = \frac{\begin{bmatrix} 4u_{xF} - u_{xG} - 3u_{xA} & 2\Delta y_1 \\ 4u_{xH} - u_{xI} - 3u_{xA} & 2\Delta y_2 \end{bmatrix}}{\begin{bmatrix} 2\Delta x_1 & 2\Delta y_1 \\ 2\Delta x_2 & 2\Delta y_2 \end{bmatrix}} \quad (5-15)$$

with a second-order accuracy. Here, $\Delta y_1 = y_F - y_G$, $\Delta x_1 = x_F - x_G$, $\Delta y_2 = y_H - y_I$, and

$\Delta x_2 = x_H - x_I$. To avoid the denominator becoming zero, the length of \overline{AH} can not be the same

as \overline{AG} . By similar operations, $\frac{\partial u_x}{\partial y} = f(u_{xA})$, $\frac{\partial u_y}{\partial x} = f(u_{yA})$ and $\frac{\partial u_y}{\partial y} = f(u_{yA})$ at point A of each

region can be obtained. By substituting all these terms back into stress-balance conditions,

Equation 5-8 and 5-9, the shear and normal stresses become functions of u_{xA} and u_{yA} . Thus with

two equations and two unknowns, the interfacial velocity at point A can be obtained.

5.2.2 Couette Flow, Fully Developed Channel Flow and Cavity Flow

Couette flow has a linear velocity profile and a constant pressure distribution, while the fully developed laminar channel flow has a parabolic velocity profile and a linear pressure distribution. The cavity flow is a typical benchmark case (Ghia et al. 1982). For all three cases, fictitious interfaces are placed inside the flow domain to examine the performance of the SIMCC. As an illustration, in Figure 5-4(A), a circular fictitious interface with a radius of 0.1 is immersed into a unit square with a 128×128 grid. This grid is used for the Couette and cavity flow calculations. In Figure 5-4(B), the fictitious interface with a radius of 0.05 is immersed into a 40×1 sized channel with a 155×90 grid system in a fully developed channel flow. These two cases are used to test the solver of continuity and momentum equations for the SIMCC.

5.2.2.1 The Couette Flow

In this section, the errors of the primary variables at the interface and conservative properties at interface will be evaluated. The evaluations of errors here are all based on a 128×128 grid. The radius of the fictitious interface is 0.1 and the center of the interface is placed at $X=0.5$ and $Y=0.5$. In this case, there are 148 cut-cells generated. The exact solution for Couette flow at each cell center of the grid is $U = y$, $V = 0$ and $P = Const.$. The error of interface velocity at each marker point is shown in Figure 5-5(A). The maximum error in this case is less than $6.0E-16$, essentially at the round-off level.

The error in the mass flux of each cell can be expressed as

$$\varepsilon = \int_{CS} \bar{u} \cdot \bar{n} dS \quad (5-16)$$

Theoretically, the summation of these errors should be zero. In this case, the total error is about $1.0E-08$, which is consistent with the accuracy supported by the formula. The error in the mass flux of each cut-cell is shown in Figure 5-5(B). In a steady-state Couette flow, the unsteady, convection, pressure gradient and the diffusion terms in the momentum equations should be zero at each cell. The convective momentum flux is adopted to verify the conservation of momentum flux at the interface. The error in convective flux of each cell can be expressed as

$$\bar{\varepsilon} = \int_{CS} \bar{u}(\bar{u} \cdot \bar{n} dS) \quad (5-17)$$

The summation of these errors should be zero. The actual total error in convective flux of all cut-cells is about $1.0E-7$ in this case. In Figure 5-5(C), the error in momentum flux of each cut-cell is shown.

5.2.2.2 The Fully Developed Channel Flow

In Figure 5-6, the test results of the fully developed channel flow case are presented. As mentioned before, the channel of length 40 starts from $X = -25$ and ends at $X = 15$. The grid is

155×90 and the Reynolds number is 100. A uniform velocity $U=1.0$ is assigned at the inlet and the fully developed boundary condition is assigned at outlet. A fictitious interface with a radius of 0.05 is selected and the center of the interface is fixed at $X = 0.5$ and $Y = 0.5$. The total number of cut-cells in this case is 92.

In Figure 5-6(A), the pressure contour near the interface is shown. It shows that the pressure distribution is linear along the axial direction and smooth across the interface. The fully developed velocity profile at $X=0.5$ is shown in Figure 5-6(B). The maximum velocity is 1.5 which agrees with the theoretical result. Also, the parabolic velocity profile supports the accuracy of the SIMCC. The conservative properties are also examined. In Figures 5-6(C)-(D), the errors in mass and momentum flux are shown. The summation of errors in mass and momentum fluxes are of the order of $1E-07$ and $1E-06$, respectively.

5.2.2.3 The Cavity Flow

In Figures 5-7(A)-(C), the streamlines of the lid-driven cavity flow with different sizes of the fictitious interface are shown. Here, $Re = 100$ is employed with a 128×128 uniform grid system. Figure 5-7(A) shows the case with no fictitious interface. Cases with fictitious interfaces of radii, 0.1 and 0.2 centered at $X=0.5$ and $Y=0.5$ are shown in Figure 5-7(B) and Figure 5-7(C), respectively.

In Figure 5-7(D), the velocity component in the X direction along $X = 0.5$ for different fictitious interface sizes are compared with the case without a fictitious interface. These three profiles almost overlap on one another and are very smooth across the interface. The shape/location of the main vortex, size/shape of the sub-vortices, and velocity component in the axial direction U at $X = 0.5$ compare favorably with benchmark results reported by Ghia et al. (1982).

5.2.3 The Fully Developed Pipe Flow with a Constant Wall Heat Flux

In this test case, a fully developed pipe flow with a constant wall heat transfer rate will be presented. The reasons for selecting this problem to be the test case are: A. there is an exact solution that can be used for validation, B. the temperature field is influenced by both convective and diffusive effects and this is enough to validate the energy equation solver. Also, a fictitious interface is again used to divide the entire domain into two regions. The thermal interfacial condition for this fictitious interface case is continuous heat flux and identical temperature at the interface. The grid system of this case is a rectangular with 1×0.5 and grid point is 80×40 .

Because it is a fully developed pipe flow, the velocity boundary condition is set to be a non-slip condition at the solid wall, symmetric condition at the centerline, fully developed velocity profile at inlet and outlet. The pressure should be a linear distribution along the axial direction. The heat flux at the solid wall is set at 1.0 and thermal conductivity is set as 1.0 also. The radius of tube is 0.5. The exact solution can be expressed as (Mills 1995)

$$T = T_s - \frac{4q''}{kR} \left[\frac{3R^2}{16} - \frac{r^2}{4} + \frac{r^4}{16R^2} \right] \quad (5-18)$$

where T_s is the temperature at wall, q'' is the heat flux and k is the thermal conductivity. To avoid the error caused by the inaccurate computation of heat flux at the wall, the thermal boundary condition at the solid wall is replaced by the equivalent temperature distribution. If k is 1.0 and q'' is 1.0, the temperature distribution along the solid wall can be written as

$$T = T(0) + 4x \quad (5-19)$$

where $T(0)$ is the wall temperature at $X=0$ and is set as 0 in this case. Therefore, an equivalent wall boundary condition at the wall is:

$$T = 4x \quad (5-20)$$

The thermal boundary condition at the centerline is set as symmetric. The thermal boundary condition at the solid wall, the inlet and outlet can be derived by the exact solution.

Figure 5-8 shows the results of temperature distribution.

To validate the result, first, the heat flux at the wall is checked to ensure that the heat flux is $\dot{q}'' = 1.0$. Figure 5-9 shows the heat flux at the solid wall and it shows that there is only a small error near the inlet and outlet and the magnitude of error is about 0.0025.

In order to validate the result further, the temperature profile at $X=0.48125$ along the radial direction is also compared and is shown in Figure 5-10. It shows that the result agrees with the exact solution very well.

Again, a half circle fictitious interface is used for this case. There are two different radii: 0.3 and 0.4. The fluid properties are the same in each phase and the thermal interfacial conditions for this fictitious interface are:

- Temperature is continuous at the interface.
- Heat flux is continuous at the interface.

Figure 5-11 shows the computed temperature distribution of each case. In Figure 5-11, it shows the results are the same as those without an interface. To further validate the case, the temperature profile at $X=0.48125$ along the radial direction for the case with a radius of 0.3 is also compared in Figure 5-12. Figure 5-12 shows the comparison and the computed results overlap with the exact solution very well.

5.2.4 Flow over a Sphere with Heat Transfer

The purpose of this test case is to check the ability of SIMCC for evaluating the heat flux at the interface. In this case, two grids with different stretching, 800×600 and 120×50 are used to demonstrate the ability of SIMCC for evaluating the heat flux at the interface. The overall dimensions of the mesh are $X = (-60, 60)$ and $Y = (0, 60)$ and a half circle is placed at the center of

lower boundary. Its radius is 0.5 and the center is located at (X,Y)= (0.5,0.0). Figure 5-13 (A) and (B) show the grid and geometry of the sphere for the case with the grid 800×600.

In this case, the pressure boundary conditions of upper, left and right sides are zero gradient and symmetric for the lower face. The thermal boundary condition (temperature) of upper, left and right sides are 0. The velocity boundary condition at interface is non-slip and the pressure at the interface is obtained by a second order extrapolation. The temperature of the interface is set at 1.0. The velocity at far field is set as 1.0, the characteristics length is the diameter of this ball. The Reynolds number is 1.0 and the Peclet number is 1.0 also. Figure 5-14 are the stream line plot and pressure and temperature contours.

In this case, the average Nusselt number is suggested by Whitaker(1972):

$$\overline{Nu} = 2 + (0.4Re^{1/2} + 0.006Re^{2/3}) Pr^{0.4} \quad (5-21)$$

Based on the current dimensionless parameter, the Nusselt number of the case with $Re = 1.0$ and $Pe = 1.0$ should be 2.406, Table 5.1 lists the calculated result.

In table 5.1, dx_min means the minimum grid size of each mesh. It shows when the grid size is decreased; better results can be obtained. When the grid is denser than 800 x 600, the error will be less than 2%. In this case, it shows that a higher resolution of results is required near the interface for the heat flux evaluation. It can also be expected that based on the same grid size, SIMCC is the method with the best performance among Cartesian grid methods and this is also the reason that the SIMCC is chosen.

5.3 Group 2, Validation for Moving Interface Algorithm

In the previous group of tests, the techniques for handling the stationary interface including the governing equations solver and SIMCC are validated. In this group, the interface in the validation cases will not be stationary but moving and deforming and therefore a moving interface algorithm must be imported to handle the movement of the interface. Two cases are

used to validate the moving interface algorithm and they are the static droplet and the rising bubble and droplet simulations.

5.3.1 Static Droplet Simulation

The first case employed here is a static droplet in a surrounding gas. The main idea here is to introduce an imbalance of pressure at the interface of a static droplet and then examine how the code reacts to the imbalance by inducing a movement at the sharp interface that results in the pressure adjustment for the interface to return to a balanced state governed by the Laplace-Young equation.

Therefore, for the first case, the selected problem is a stationary water droplet surrounded by its own vapor under isothermal condition in zero gravity. The density ratio is 1,605 and the viscosity ratio is 22. If there are no other force field effects and under a dynamic equilibrium, this droplet should stay stationary and the pressure difference at the interface between the liquid and vapor should be balanced by the surface tension.

The geometry of this validation problem is a two-dimensional domain in an axisymmetric coordinate system with length and width equal to 2.0 and 1.0, respectively. The grid arrangement is 80×40 . A half circle mounted on the center of the lower boundary is used to represent the interface. Figure 5-15 is the illustration of this problem.

The boundary conditions are zero gradients for velocity and pressure at right, left and upper sides and symmetric at lower side since this is an axisymmetric computation. The initial conditions for the velocity and pressure are zero everywhere that creates a pressure imbalance at the interface. In this computation, the Weber number is selected as 0.5. Since the curvature is 4.0 everywhere, the exact pressure jump between the liquid and the vapor phase should be 8.0. Figure 5-16 shows the maximum induced interfacial velocity during the transient adjustment period. It must be emphasized that for the incompressible flow computation, strictly speaking

there should be no induced interfacial velocity for this problem because of the stationary condition and the conservation of mass. However, because of the imbalance of interfacial dynamics, an extremely small interfacial velocity is induced. This small order of magnitude velocity distribution (deformation of interface; induced interfacial velocity) should be considered a numerical disturbance and not a violation of the incompressible assumption. However, the SIMCC code can use it to adjust the pressure difference of each phase since the disturbance of velocity will cause the change of pressure in each phase. In Figure 5-16, the maximum induced interfacial velocity varies and achieves the steady state finally. The maximum induced interfacial velocity is about $1.0E-5$ in this case.

Figure 5-17 shows the convergent histories for the governing equations and the interfacial condition. In the beginning, the interface was adjusted seriously to satisfy the governing equations and interfacial condition. In this stage both residuals are decreasing very fast. After 100 iterations, once the residue of interfacial condition (imbalance) is too small to push the interface, the interface will become stable gradually and looks like a “fixed” interface. In the meantime, the residual of governing equations must be small enough also and this means governing equations and interfacial condition reach convergence at the same time.

Figure 5-18 is the pressure contour for this problem. It shows the pressure difference is identical to the theoretical value, 8.0 and the discontinuity at interface can be handled very well by the current method. The sharp pressure discontinuity across the interface is successfully computed.

5.3.2 Deformed Rising Bubble and Droplet

For the second case, the buoyancy-driven rising bubble and droplet through a quiescent liquid are selected. The test problems in the second case are classified into two groups based on the density ratio (dispersed phase to continuous phase). These groups are the low density ratio

(<0.001) bubbles and higher density ratio (= 0.91) droplets used to verify the current method with a wide range of density ratios. The computational domain used in this section is a rectangle with a length of 70 and width of 38 and the grid system is 550×100 . From $X=0$ to $X=20$ and $R=0.0$ to $R=2.0$, the grid spacing is uniform and then the grid spacing is stretched to the upper, right and left sides. Since the domain is large enough, the boundary conditions are assigned as the zero gradients for both velocity and pressure at the upper, right and left boundaries and a symmetric condition on the lower boundary (centerline). The initial condition for this case is quiescent fluids in both phases and a half-circle with a radius of 0.5 is used to represent the bubble/ droplet and the center of the half-circle is located at (3.0, 0.0). The time step here is 0.01.

For the bubble problem (density ratio ~ 0.001), $Re = 10$ and $We = 8.0$ are assigned. In Ryskin and Leal's research (1984), the bubble is an open space without any fluid. In this computation, water is adopted to be the ambient liquid and the bubble is water vapor, so the density ratio 0.0006 and viscosity ratio is 0.045. Figure 5-19 is a comparison between the current computed result and the result of Ryskin and Leal. It shows that the two agree well with each other.

For further verification with the same bubble of $Re = 10$ but different Weber numbers of $We = 2.0 - 8.0$, the results of the aspect ratio (height to width) are compared with those of Lai et al. (2004) in Figure 5-20. The comparison is very favorable.

For the higher density ratio problem, the droplet with $Re = 10$ and $We = 2$ is adopted for comparison. The density ratio and the viscosity ratio are assigned as 0.91 and 4, respectively so the computed result can compare directly with results by Dandy and Leal (1989).

Figure 5-21 shows that the current computed result agrees well with that of Dandy and Leal in flow structure and droplet shape.

5.4 Group 3, Validation for Accurate Mass Transfer at the Interface

Tests in this group focus on validating the phase change computation at interface. The two test cases used are: a stationary droplet in a quiescent environment with a constant mass transfer rate, and one dimensional phase change problem.

5.4.1 A Stationary Droplet in a Quiescent Environment with a Constant Mass Transfer Rate

For this test case, the main purpose is to evaluate the performance of current code on the velocity discontinuity at the interface between the droplet and its surrounding fluid due to mass transfer. In order to accurately evaluate the current numerical technique, a simplified case was designed where a stationary droplet is assumed to vaporize with a given constant mass transfer flux at the interface. In this way, heat transfer is not involved in the simulation and only the continuity and momentum equations are solved. For this test case, an axisymmetric cylindrical coordinate system is employed. Figure 5-22 is a schematic of this problem. The computational domain is a rectangle with dimensions of 10×5 . A hemi-sphere with an initial radius 0.5 is placed at the center of the lower boundary. The boundary conditions of upper, right and left sides are the second order extrapolations for both velocity and pressure and symmetric at the lower boundary.

In this test case, a water droplet is used and the density of water is $958.3 \text{ kg} / \text{m}^3$ and $0.597 \text{ kg} / \text{m}^3$ for the vapor. In this computation, the numerical time step is 0.1 and the constant and uniform mass flux that leaves the droplet surface, \dot{m} , is assumed to be $10.0 \text{ kg} / \text{m}^2 \text{ s}$. It is noted that there is no internal velocity field inside the droplet because of the quiescent environment that results in an induced interface receding velocity as follows:

$$(u_n)_{\text{int}} = \frac{\Delta m}{\rho_l \Delta t} = \frac{\dot{m}''}{\rho_l} \quad (5-22)$$

The vapor velocity at the interface can be calculated by

$$\dot{m}'' = \rho_v \left((u_n)_v - (u_n)_{\text{int}} \right) \quad (5-23)$$

Based on the assumed mass flux, the vapor velocity at the interface is 16.76 m/s. As the velocity in the vapor phase is solely due to the uniform mass from the droplet surface, the vapor velocity at any radial distance from the droplet surface can be predicted based on conservation of mass:

$$\rho_1 u_1 A_1 = \rho_2 u_2 A_2 \quad (5-24)$$

The velocity of vapor at different location in the vapor phase can be expressed as

$$\frac{u_1}{u_2} = \frac{r_2^2}{r_1^2} \quad (5-25)$$

where r is the distance measured from the center of the droplet. If the known vapor velocity at the interface is used as the reference velocity, the velocity at any location in the vapor phase can be obtained. Therefore, the obtained velocities including the interface velocity, the velocities of both liquid and vapor phases at the interface and the velocities at the outer boundary of the computational domain will satisfy both the continuity equation and interfacial mass conservation condition and therefore they can be considered as the exact solution of this test case and used to validate the numerical results.

Figure 5-23 shows the computed velocity distribution by the current code versus the exact velocity along the radial direction at $X=5$ after first time step. In Figure 5-23, the velocity is zero everywhere in the liquid phase and a huge velocity discontinuity exists at the interface. The maximum vapor velocity is located at the interface and the velocity decays by $1/r^2$ to the outer boundary of the domain. A comparison shows that the computed result agrees closely with the

exact solution. This proves that the current code can handle the mass transfer at the interface with a velocity discontinuity with a high accuracy.

Figure 5-24 is the stream line plot near the water droplet. In Figure 5-24, it shows that the streamlines radiate from the interface to the far field straight.

5.4.2 One Dimensional Phase Change Problem

One dimensional phase change problem also called Stefan problem is a classic test problem and broadly used for the validation for moving boundary/interface algorithm in computational multiphase flow with phase change (Bonacina et al. 1973, Welch and Wilson 2002, Mackenzie and Robertson 2000). Using this test problem, the performance of moving boundary/interface algorithm for phase change computation especially the accuracy of mass transfer at boundary/interface can be evaluated.

The entire system is shown as Figure 5-25. The left forward slashed block represents the wall and it will keep stationary with a constant temperature T_{wall} . The dash-dot line with a distance $\delta(t)$ from the wall is the interface and separates the gas and liquid. The liquid phase and the interface are assigned the saturation temperature T_{sat} . Once phase change happens, the liquid will be vaporized and the volume of gas will increase so that the interface will be pushed to the right side. During the vaporization, the velocity of gas is still kept as zero.

Since the velocity of gas phase is zero, the original unsteady-convective-diffusive energy equation in gas phase can be simplified as unsteady-diffusive equation:

$$\frac{\partial T}{\partial t} = \alpha \frac{\partial^2 T}{\partial x^2} \quad 0 \leq x \leq \delta(t) \quad (5-26)$$

where $\delta(t)$ is the location of this phase interface and α is the thermal diffusivity and defined as

$\alpha = \frac{k}{\rho C_p}$. For this moving boundary/interface problem, the system of equations is closed by

specifying the boundary conditions:

$$\begin{cases} T(x = \delta(t), t) = T_{sat} \\ T(x = 0, t) = T_{wall} \end{cases} \quad (5-27)$$

The conservation of mass at interface:

$$\rho_g v_g \lambda = -k_g \frac{\partial T}{\partial x}_{x=\delta(t)} \quad (5-28)$$

The theoretical solution of temperature and location of interface for this test problem can be found by Alexiades and Solomon's book (1993):

$$\delta(t) = 2\zeta \sqrt{\alpha t} \quad (5-29)$$

$$T(x, t) = T_{wall} - \left[\frac{T_{wall} - T_{sat}}{\text{erf}(\zeta)} \right] \text{erf} \left(\frac{x}{2\sqrt{\alpha t}} \right) \quad (5-30)$$

where erf is the error function and the parameters ζ can be obtained by solving the transcendental equation:

$$\zeta e^{\zeta^2} \text{erf}(\zeta) = C_p \frac{T_{wall} - T_{sat}}{\lambda \sqrt{\pi}} \quad (5-31)$$

In this validation case, the fluid properties of each phase are assigned in Table 5-2, and by this set of properties, the parameter ζ is solved as 1.0597.

Although it is a one dimensional problem, it is computed by the two dimensional code in order to apply the Cut-cell approach at the interface to obtain the best resolution. For the upper and lower side, the boundary conditions are assigned symmetric to simulate one dimensional condition. The computation domain is a 1.0×0.02 rectangle and the grid point are 500×10 , the interface is located at $\delta(t) = 2\zeta \sqrt{\alpha t} = 0.2$ initially and corresponding time is 0.089. The initial

condition can be obtained by the theoretical solution. Figure 5-26 is the obtained results. By this set of figures, it can be seen that the present results match the theoretical results very well. In Figure 5-26(A) and (C), they show the accuracy of the current energy equation solver, moving interface/boundary algorithm and the mass transfer at interface. An accurate interface position can be obtained only when all the above techniques work well. In Figure 5-26(B), all the isothermal lines are purely vertical which means that the current Cut-cell approach can achieve truly high resolution. Overall, by this test problem, the energy equation solver, the moving interface algorithm, the Cut-cell approach and the accuracy of heat flux computation at interface are validated further.

5.5 Summary

In this chapter, the ability of SIMCC is examined systematically. In the first group, it has been demonstrated that the current solver of governing equation is very accurate and the SIMCC only induced tiny errors at the interface. In the second group, by compared with others' results, it has been shown that the SIMCC can handle the moving interface problems well. In the last group, by the two test cases, it has been shown that SIMCC can compute the mass transfer rate from the interface correctly and adjust the interface due to the phase change very accurately. By this series of test cases, the capability of the full set of SIMCC technique to handle the current research is established.

Table 5-1. The error of Nusselt number by different grid resolutions in flow over a sphere case.

	Grid	Nusselt	dx_{\min}	Error
Case 1	120x 50	1.14	0.05	52.3%
Case 2	800x 600	2.36	0.003	1.9%

Table 5-2. The fluid properties of liquid and gas phases for the one dimensional phase change problem.

	Gas	Liquid
Density (ρ)	0.2	1.0
Heat capacity (Cp)	5.0	10.0
Thermal conductivity (k)	1.0	1.0
Latent heat (λ)	N/A	1.0

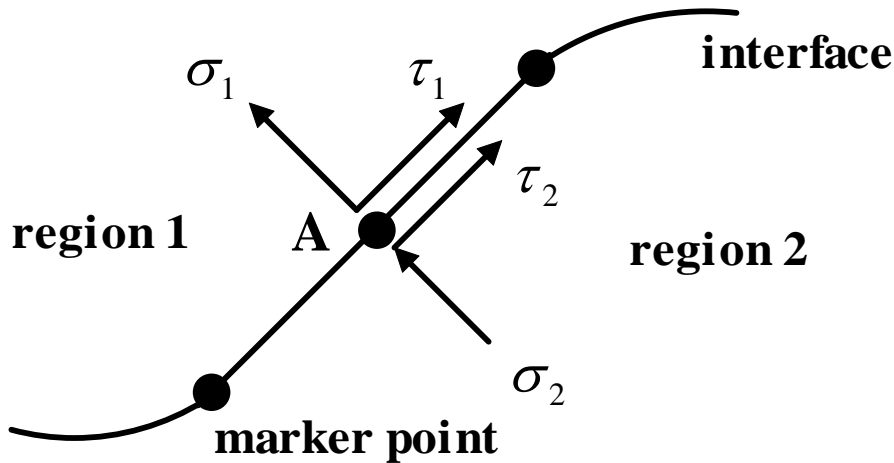


Figure 5-1. The continuous stress condition at marker points for the fictitious interface.

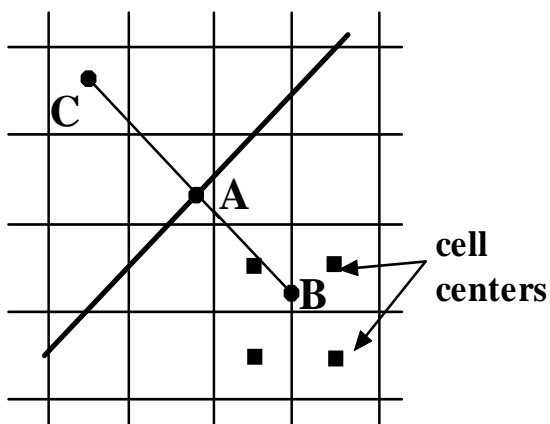


Figure 5-2. The algorithm for second order gradient.

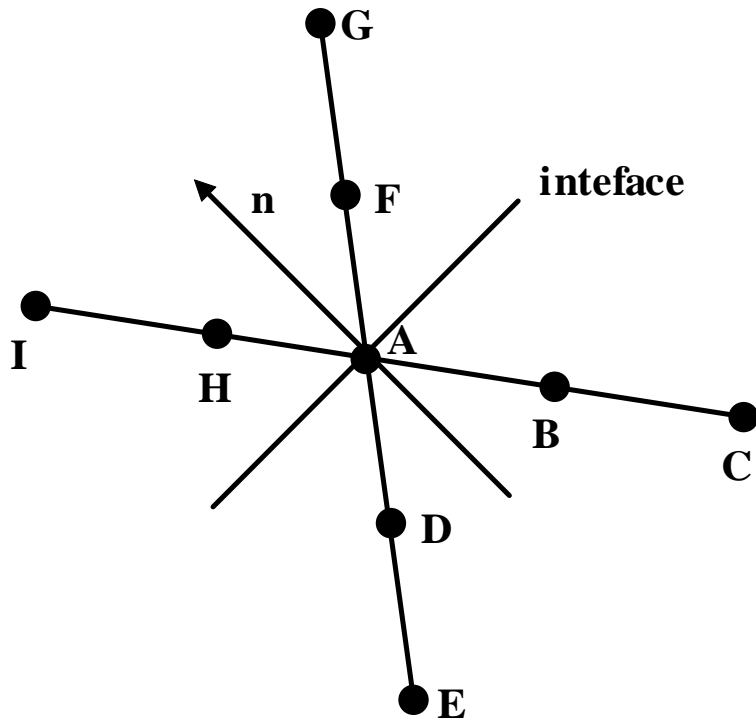


Figure 5-3. Eight points method for second order gradient of velocity.

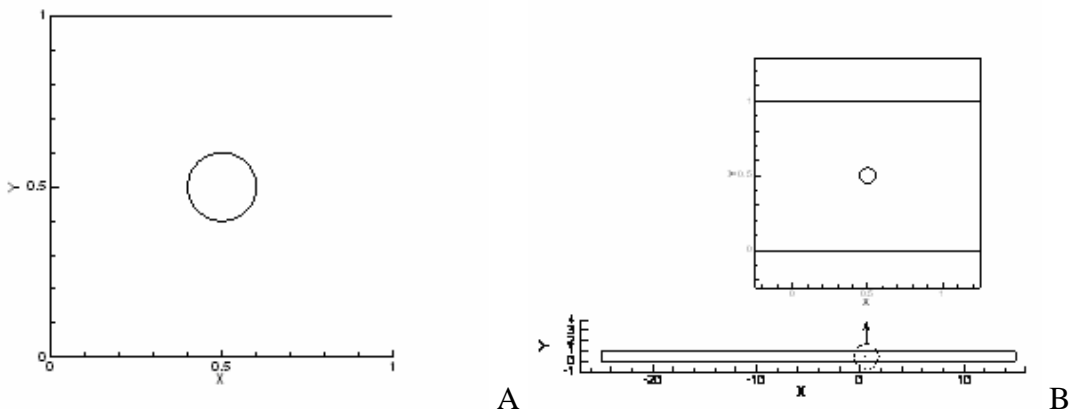
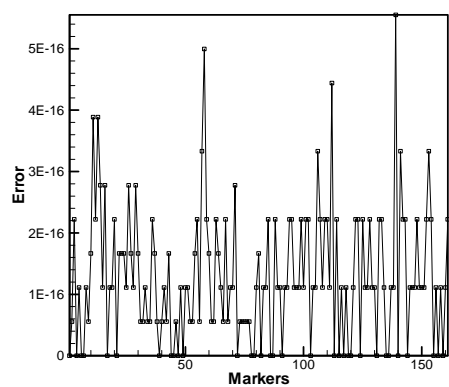
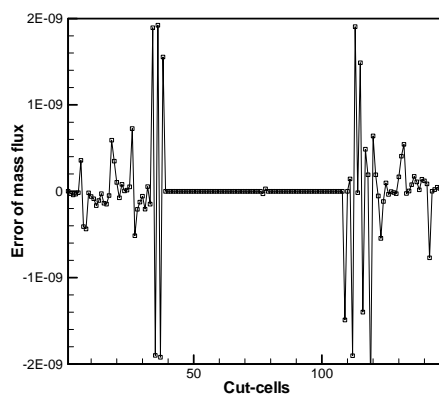


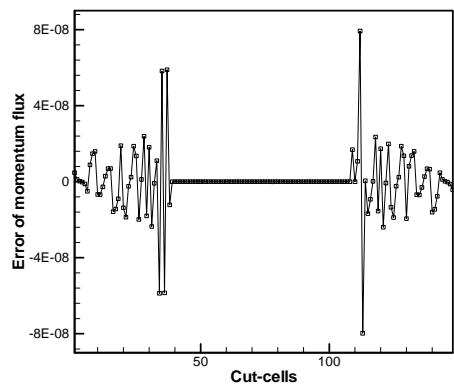
Figure 5-4. Geometry of the Couette flow, cavity flow and fully developed channel with the immersed fictitious interface. A) Couette flow and cavity flow, B) fully developed channel flow.



A



B



C

Figure 5-5. Error in interfacial velocity at all the interfacial marker points (163 points) and error in mass and momentum fluxes of each cut-cell (148 cut-cells) in the Couette flow with radius of fictitious artificial interface $R=0.1$. A) error in interfacial velocity, B) error in mass flux, C) error in momentum flux.

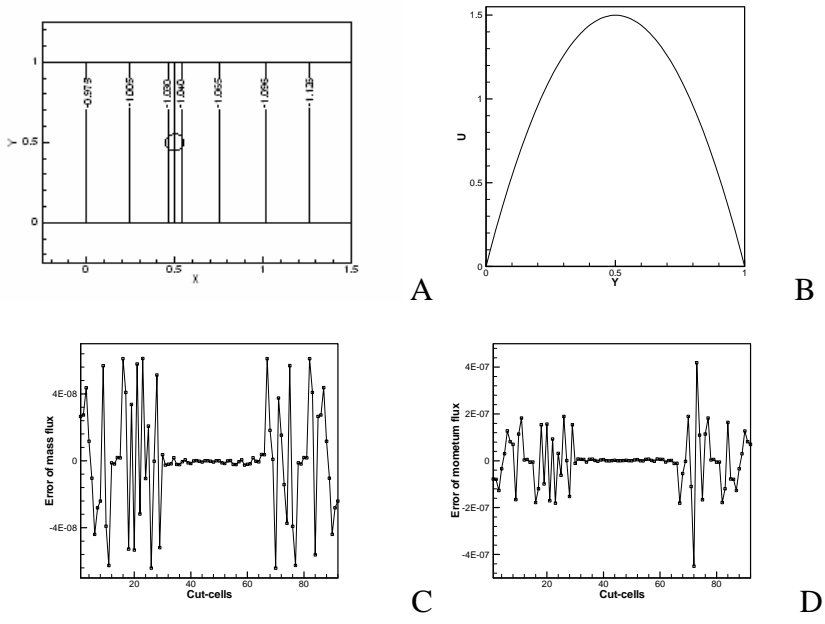


Figure 5-6. Pressure contour, U velocity profile, and error in mass and momentum fluxes of each cut-cell (92 cut-cells) of fully developed channel flow with radius of fictitious interface $R=0.05$ and $Re=100$. A) pressure contour near the artificial interface, B) velocity profile at $X=0.5$, C) error in mass flux, D) error in momentum flux.

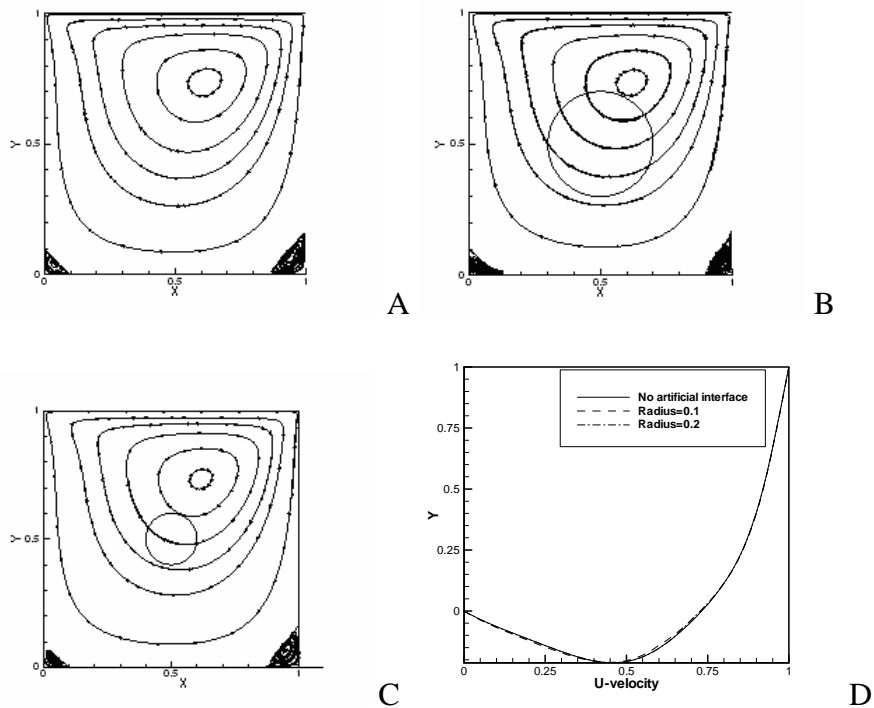


Figure 5-7. Streamline plots and U velocity profile at $R=0.5$ with different fictitious interface radii of cavity flow with $Re=100$. A) streamline plot with no interface, B) with radius=0.1, C) with radius=0.2, D) velocity profile along $X=0.5$.

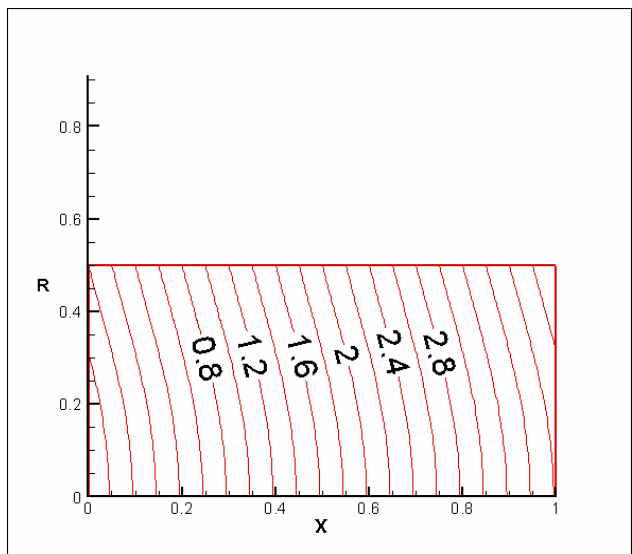


Figure 5-8. The temperature distribution of fully developed pipe flow with constant heat flux case.

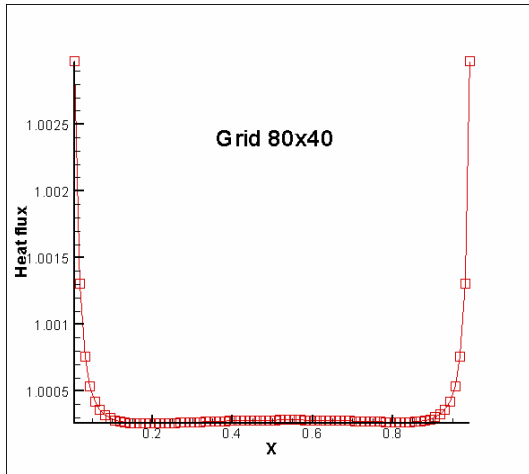


Figure 5-9. The heat flux at wall of fully developed pipe flow with constant heat flux case.

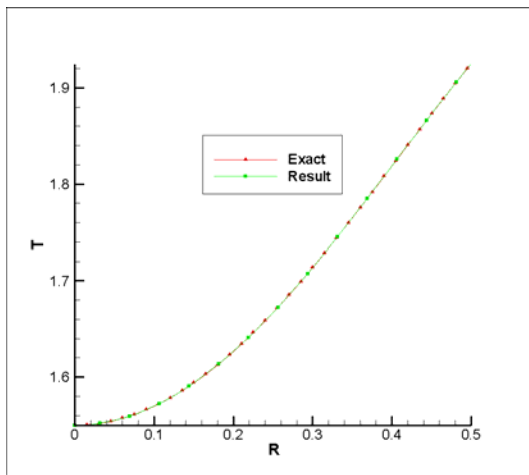


Figure 5-10. The temperature profile of fully developed pipe flow with constant heat flux case at $X=0.481235$ along radial direction.

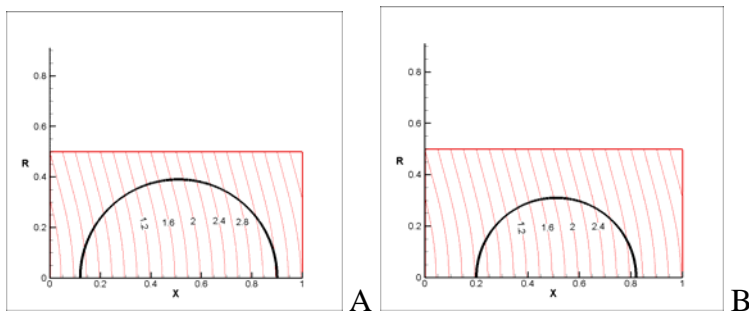


Figure 5-11. The temperature distributions of fully developed pipe flow with constant heat flux case with different fictitious interfaces. A) $R=0.4$, B) $R=0.3$.

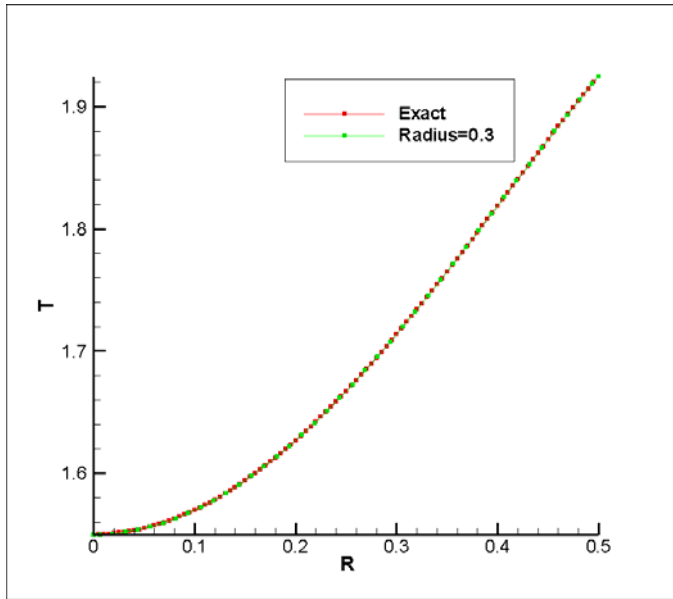


Figure 5-12. The temperature profile of fully developed pipe flow with constant heat flux case with a fictitious interface ($R=0.3$) at $X=0.481235$ along radial direction.

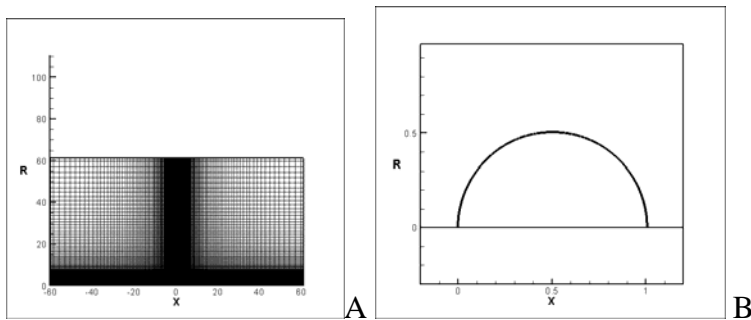


Figure 5-13. Grid and geometry of flow over a sphere with heat transfer. A) the grid system, B) the interface.

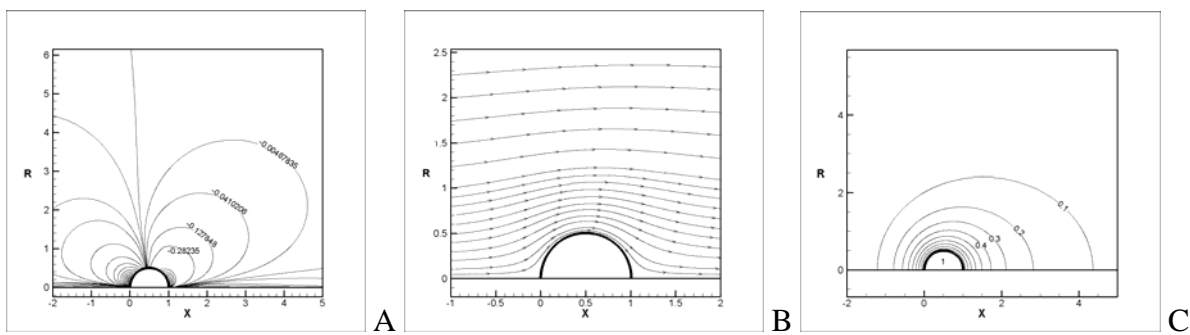


Figure 5-14. The pressure contour, the stream line and temperature contour of flow over a sphere with $Re=1$, $Pe=1$.

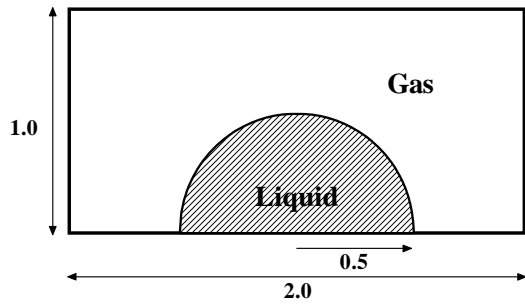


Figure 5-15. Schematic of stationary droplet problem.

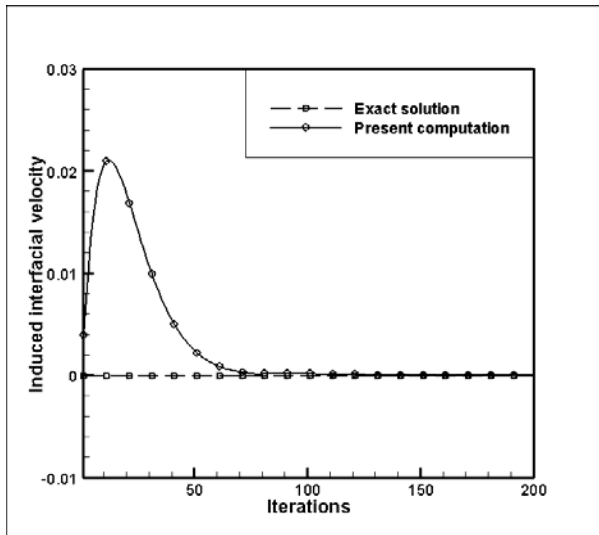


Figure 5-16. The maximum induced interfacial velocity of stationary droplet problem.

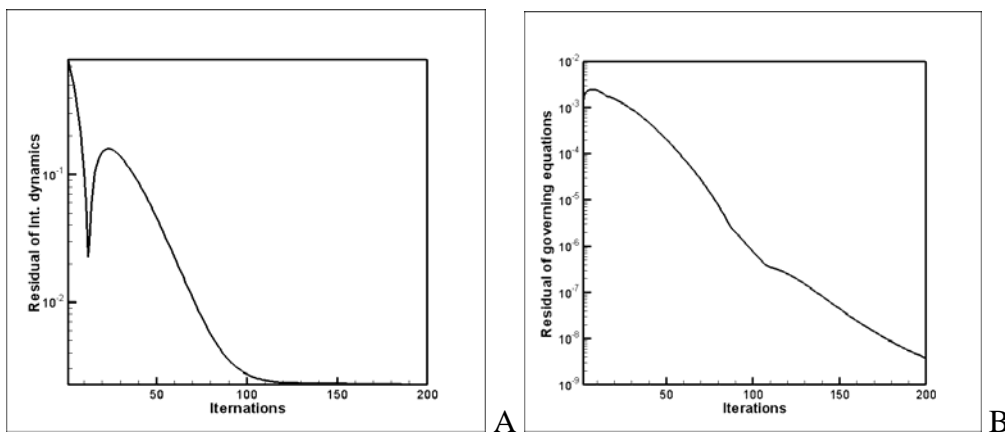


Figure 5-17. Convergent histories of the interfacial condition and the governing equations of stationary droplet problem. A) interfacial condition, B) governing equations.

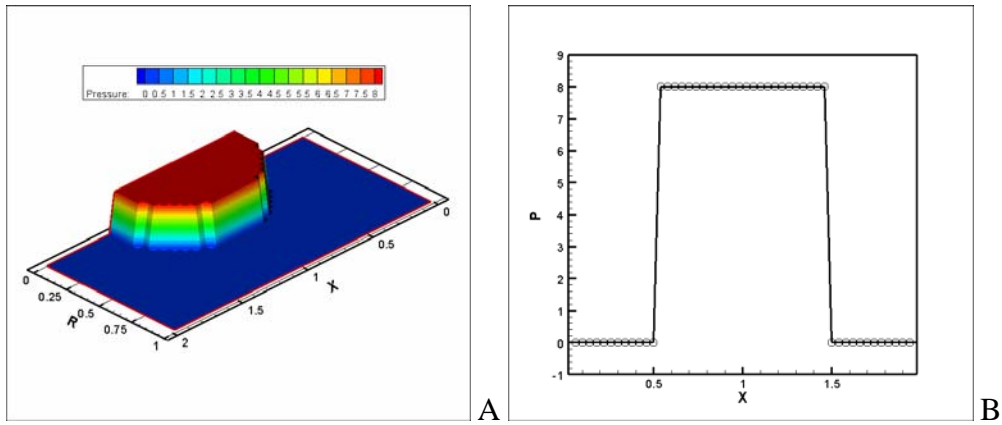


Figure 5-18. Pressure contour for the stationary droplet. A) entire pressure contour, B) pressure along X axis at $R=0$.

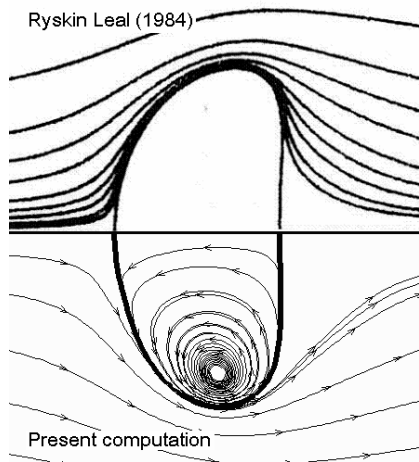


Figure 5-19. The shape and streamline plot for a bubble with $Re=10$ and $We=8$.

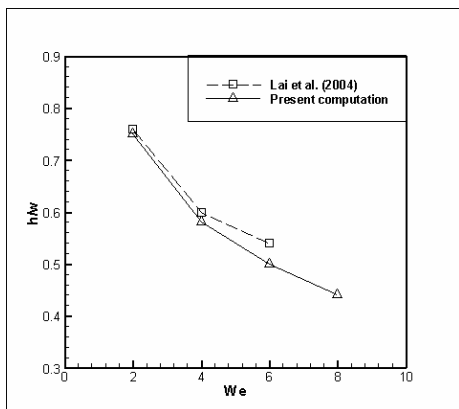
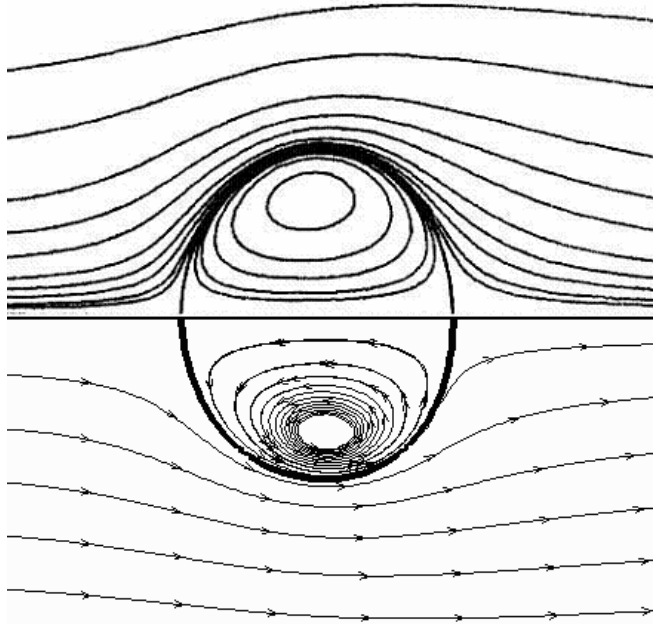


Figure 5-20. The aspect ratio plot for a bubble with $Re=10.0$ and $We= 2.0-8.0$.

Dandy & Leal (1989)



Present computation

Figure 5-21. The streamline and shape plot for a droplet with $Re=10$ and $We=2$.

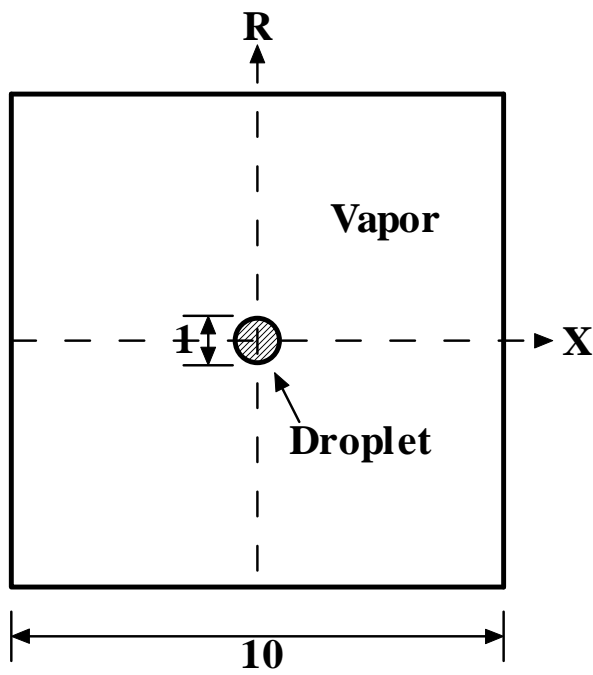


Figure 5-22. Geometry of static droplet with a constant mass transfer rate problem.

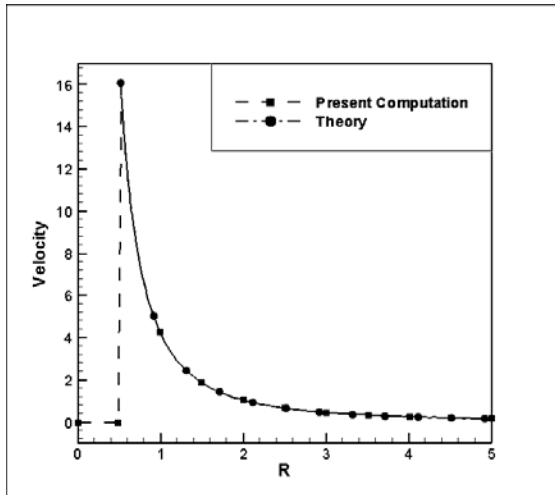


Figure 5-23. Velocity distribution of static droplet with a constant mass transfer rate problem along radial direction at $X=5$.

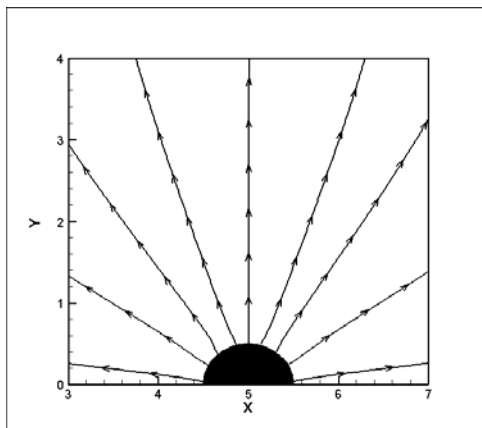


Figure 5-24. Streamline plot near the interface of static droplet with a constant mass transfer rate problem.

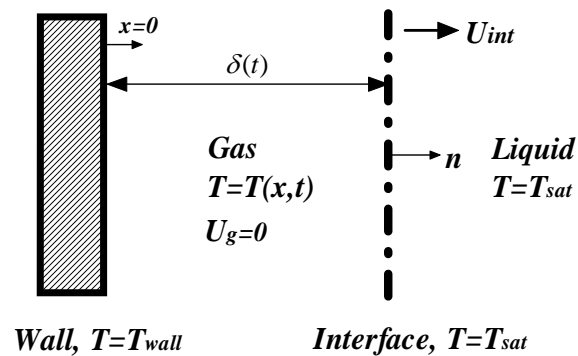
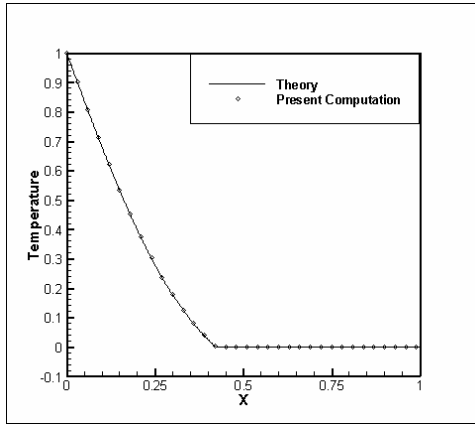
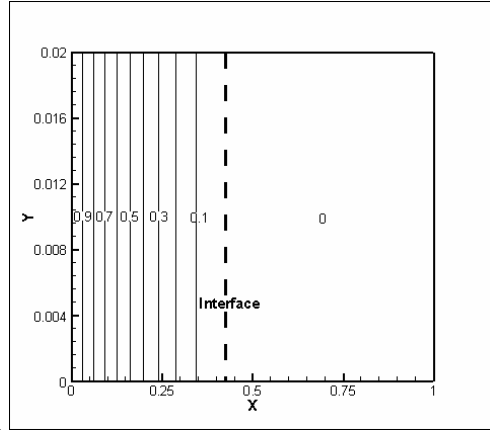


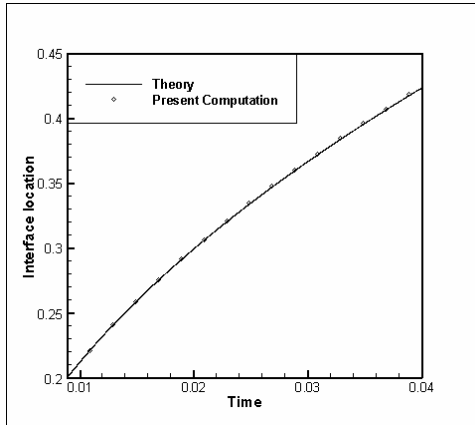
Figure 5-25. Illustration of one dimensional phase change problem.



A



B



C

Figure 5-26. The location of interface and temperature distribution, contour for one dimensional phase change problem. A) temperature distribution, B) temperature contour, C) location of the interface.

CHAPTER 6 LIQUID-GAS TWO-PHASE FLOWS IN A PIPE WITHOUT PHASE CHANGE

6.1 Introduction

In this chapter, the main focus is the liquid-gas two-phase flow in a pipe without phase change. There are two studies discussed in this chapter.

The first study is isothermal two-phase flow, and the selected liquid is the nitrogen at 77K at 1 ATM. Since 77K is the saturation temperature of nitrogen, the nitrogen can exist as both liquid and vapor. Since the temperature is fixed, the energy equation will not be solved and only the continuity, momentum and interfacial conditions are solved. There are two dimensionless parameters that affect the flow in this case: the Reynolds number (Re) and the Weber number (We). In real cryogenic flow, the Reynolds number is usually very high. Therefore only cases with higher Reynolds number are considered here. By definition, Reynolds number and Weber number can vary independently according to the surface tension. Therefore both high and low surface tension cases are possible and will be discussed.

The second case is two-phase flow with heat transfer but no phase change. In this case, the proposed fluids are liquid water at 273K and air at 373K at 1 ATM. Based on the assumptions, water will not be vaporized with just simple heat transfer taking place at the interface. The energy equation will be solved and another dimensionless parameter Peclet number (Pe) will be included into the energy equation. Similar to the isothermal case, only the cases with higher Reynolds number are considered here. Again, once the Reynolds number is decided, the Weber number may be large or small and therefore two cases of surface tension will be discussed here. The Peclet number can not be assigned independently and should be determined based on the Prandtl number (Pr). The Prandtl number is a fluid property and therefore, once Reynolds number and species of the fluid are determined, the Peclet number is determined also.

6.2 Isothermal Liquid-Gas Two-Phase Flows in a Pipe

In this section, the computational method presented in previous chapters is employed to numerically simulate a liquid cylindrical plug translating through gaseous medium in a circular pipe. The purpose is to demonstrate the capability and accuracy of the current method for a pressure-driven internal two-phase flow with a moving interface due to shape deformation and liquid phase translation. The ratios of fluid properties of two phase flows are:

$$\frac{\rho_l}{\rho_g} = 352.4; \quad \frac{\mu_l}{\mu_g} = 15.8$$

The sample problems are classified into two groups. For liquid-gas two-phase flows, as indicated by the governing equations presented in previous chapters, the Reynolds and Weber numbers are the only dimensionless parameters needed to characterize and distinguish different fluids and flow regimes. Two major groups are adopted here. The first group is used to focus on the effects of different Reynolds numbers. In this group, there are four Reynolds numbers selected: 250, 500, 1000 and 2000 and the Weber number is fixed at 500. For the first group, with the combinations of Reynolds and Weber numbers, it could represent fluids such as liquid nitrogen or water. For the first group, the objective is to examine the convection effects characterized by various Reynolds numbers. In the second group, the Reynolds number is fixed as 500 and three different Weber numbers that correspond to three different strengths of surface tension are selected. These three surface tensions are equal to 1.0, 0.1, and 0.01 time the pressure difference that result in three different Weber numbers of 2.6316, 26.316 and 263.16, respectively. For this group, the main challenge is to demonstrate the ability of current SIMCC code to handle the large deformations due to the surface tension effect.

6.2.1 Effect of the Reynolds Number

For this group, the inflow boundary conditions for the velocities of both phases at the inlet are assigned as 1.0. While for the pressure, 1.0 is set for the vapor phase and $1.00526 (p_l = p_g + curvature / We)$ for the liquid phase, respectively, to include the surface tension effect between the two phases at the inlet. This strategy will be applied in all following cases to make the first point of interface is fixed at the same location in the inlet boundary during the computation. The time step in this computation is set at 0.001.

First, the flow streamlines in the two-phase zone and those immediately after it are plotted in Figure 6-1 for $t = 6.0$ and $Re = 2000$. In the two-phase zone, the streamlines are almost straight and parallel as expected. The transition from the two-phase zone to the single-phase pure gas zone near the front of liquid core is very smooth. The lines are slightly distorted in the vicinity of the liquid front as the gas flow is trying to fill the entire pipe interior. In this type of flow, since the velocity at wall is zero and therefore, the flow will be pushed towards the center of pipe for a fully developed parabolic profile because of the mass continuity. Therefore, the streamlines of gas phase near the front of liquid core get distorted to satisfy the continuity of mass.

Figures 6-2(A), (B) and (C) show the pressure maps at $t = 6.0$ with $Re = 2000$. Figures 6-2(B) and (C) focus on the two-phase zone and single phase zone, respectively, while Figure 6-2(A) provides pressure distribution for the entire computational domain. For the single gas phase (downstream of the liquid core), Figure 6-2(C) shows that the pressure decreases linearly along the axial direction that is similar to a fully developed single-phase gaseous pipe flow. For the two-phase flow zone as shown in Figure 6-2(B), the pressure driven flow patterns are displayed in the gas and liquid parts, respectively. The slight discontinuity is seen at the liquid-gas

interface due to surface tension, dynamic head and shear stress effects. In general, the entire domain is composed of three sub-domains that all show approximately linear pressure gradients. This also shows the ability and accuracy of the current SIMCC for multiphase computations.

Figure 6-2(D) shows the axial pressure distributions at the pipe wall, radial location $R = 0.2$ and the center of pipe. Basically, the three curves are very close to one another so the pressure is relatively independent of the radial location. In general, the pressure profile is composed of two linear curves (one for the two-phase zone and the other for the single-phase zone) of different gradients that are joined at the frontal area of the liquid core. The gradient in the two-phase zone is much larger than that of the single-phase zone because the gas phase in this two-phase zone must accelerate and create a jet profile. Also this is due to the fact that the gas-phase controls the pressure drop. The sharp drop in pressure in the centerline curve is due to surface tension.

For the purposes of examining the ability of the current method to accurately simulate the transition from the two-phase zone to the single-phase zone, Figure 6-2(E) and (F) were plotted to provide three radial and three axial local enlargements of pressure distributions in the neighborhood of the liquid core frontal area. In Figure 6-2(E), it shows that axial pressure distributions along the centerline and at $R = 0.2$ are very similar to each other, except that the sharp drop discontinuities are located at different axial locations according to where the interface is positioned. As expected, the pressure distribution at the wall is continuous without any discontinuity and has a smooth transition between the two zones. The three curves all merge together after the liquid front in the pure gas zone. In Figure 6-2(F), three pressure distributions in the radial direction are plotted at different locations, $X = 6.2, 6.4$ and 6.6 . For $X = 6.6$, basically, it is located in the pure gas phase and hence, it is virtually a straight line. At $X=6.2$,

there is drop between $R=0.35-0.37$ and this is the location of interface. At $X=6.4$, the drop exists at $R=0.17-0.19$ and the interface is located at this section also. Inside the liquid phase, there are very slight pressure fluctuations prior to the drop and the pressure rises slightly after the drop in the gas phase. Both pressure variations are believed to be due to the changes in the gas phase immediately after the interface where the gas flow is slowing down and bending towards the center.

The above can be further explained by examining Figure 6-2(G). Figure 6-2(G) is a plot of the curvature along the liquid-gas interface. The plot is based on about six hundred marker points placed on the interface with uniform separation distance between adjacent points. Point 1 is at the entrance and last point is at the centerline. The curve shows that the curvature is about 5.4 at the centerline (last marker). In this computation, the effect of viscosity is very weak because of the high Reynolds number and the velocity is continuous at interface. With these conditions, the interfacial condition can be simplified as

$$p_l - p_v = \frac{\kappa}{We} \quad (6-1)$$

By this simplified interfacial condition and the dimensionless parameters, it can be estimated that the order of pressure discontinuity at the interface is about κ/We . According to the curvature at the liquid front in Figure 6-2(G) and the assigned Weber number, the pressure discontinuity can be roughly estimated about $0.0108 = (5.4/500)$. This pressure differential is verified in Figures 6-2(E) and (F).

In summary, the magnified pressure plots given in Figure 6-2 demonstrate that the current method is capable of capturing the pressure discontinuity and flow transition from a two-phase condition back to a single-phase condition with fidelity and accuracy.

Figure 6-3 shows the pressure distributions along the centerline of the pipe for $We = 500$ and four different Reynolds numbers: $Re = 250, 500, 1000$ and 2000 . For each Reynolds number, the pressure distribution is composed of two straight lines of different slopes as explained before for Figure 6-2(D). In general, the rate of dimensionless pressure drop is inversely proportional to the Reynolds number. For the case with the highest Reynolds number of 2000 , the pressure drop is only around 10% of the case with the lowest Reynolds number of 250 and this trend is the same as that in the single phase flow because the pressure difference will be used to balance the shear stress occurring at the wall. In each curve, the pressure shows a small drop at the front of liquid core and the magnitude is about 0.011 for all the cases. This is reasonable since the strength of surface tension in each case is about the same.

Figure 6-4(A) shows the velocity profiles at different axial locations: $X = 2, 4, 6$ and at the exit of the pipe. Since the flow is two-phase for $X < 6.4$, the velocity profile at any axial location comprises of two parts corresponding to the phase. In the liquid region the velocity is uniformly 1.0 . In the gas phase portion, because the velocity is zero at the wall and non-slip between the two phases at the interface, the gas profile would have a jet effect as shown in Figure 6-4(A) and the maximum velocity is located near the liquid phase since the velocity of liquid core is about 1.0 . In the two-phase zone, the velocity profile relatively does not depend on the axial location.

In the current method, the global conservation of mass is the key element and therefore, the global conservation of mass must be satisfied and verified. For this two-phase computation, both phases are assumed incompressible. Therefore, the rate of the “volume” of fluids in and out of the pipe should be the same at any instant. This implies after the flow in the single-phase gas zone reaches the fully developed condition, the gas flow velocity profile should be identical to the conventional single phase fully developed flow in a pipe that is a parabolic profile. Since the

gas flow has reached the fully developed condition well before the exit, the velocity profile named as “U at X = Exit” in Figure 6-4(A) and (B) should be the theoretical parabolic profile with maximum velocity of 2 at the centerline and zero at the pipe wall. The comparison between calculated velocity profile and the theoretical result is given in Figure 6-4(B). It is seen that the agreement is excellent.

Figure 6-5 shows the shape of liquid cores for different Reynolds numbers at the same time, time=6.0. As expected, there is no significant difference among these cases because the strength of surface tension is about the same here as the Weber number is the same for all four cases. After 6000 time steps, the front of liquid core does show slightly different deformation due to the convection effect.

6.2.2 Effect of the Weber Number

In this group of simulations, the Reynolds number is kept at 500 while the purpose is to evaluate the ability of the current method to handle larger deformations due to higher surface tension effects. The boundary conditions are very close to those used in group one except at the entrance. The radius of liquid core is 0.38 at the entrance and therefore, the curvature will be $2.6316 = (1.0/0.38)$ in the theta direction. If the Weber number is assigned as 2.6316, the pressure discontinuity at the interface between the two phases at the entrance should be 1.0 (κ/We). With this procedure, once the curvature is fixed, the pressure difference can be adjusted by changing the Weber number. Based on this idea, three different Weber numbers are selected in this group: 2.6316, 26.316 and 263.16 to generate three pressure jumps, p_{liquid} / p_{gas} at the interface of 2.0, 1.1 and 1.01, respectively at the entrance.

Figures 6-6(A), (B) and (C) show the pressure maps at $t = 6.0$ with $Re = 500$ and $We = 2.63$. Figures 6-6(A) and (B) focus on the two-phase zone and single-phase zone, respectively,

while Figure 6-6(C) provides pressure distribution for the entire computational domain. In general, the features in Figure 6-6 are similar to those in Figure 6-2 but both Reynolds and Weber numbers are smaller for the current plots. In this case, the pressure jump between the two phases is equal to 1.0 at the entrance. At the front of liquid core, because the surface tension is much stronger due to a larger curvature than that at the entrance, the pressure in the liquid phase at this front of the liquid core is raised to balance the larger surface tension. In Figure 6-6, it also shows the larger deformation due to the surface tension at the front of the liquid core. For the entrance portion, there should be no deformation because the equilibrium condition is assigned there. This shows the ability of SIMCC to handle the surface tension effect and large deformation. Figure 6-6(B) focuses on the pressure contour at downstream of the liquid core. It shows the downstream pressure decreases linearly that is similar with the single phase flow.

Figure 6-7(A) provides the pressure distributions along the wall and centerline of the pipe. It shows that the pressure distribution at the wall is constructed by two linear profiles of different slopes, and this trend is very similar with the case of wall pressure distribution as shown in Figure 6-2(D) for different Reynolds and Weber numbers. For the liquid phase at the centerline, the pressure decreases linearly near the entrance and rises up before going through a large discontinuous drop across the interface at the front of liquid core. Figure 6-7(B) is the curvature along interface. Similar to Figure 6-2(G) in group one, Figure 6-7(B) shows the curvature values of the liquid-gas interface. The general trend in Figure 6-7(B) is also similar to that in Figure 6-2(G). Near the entrance, the curvature is almost constant because only theta direction (tangential) is involved. Near the liquid core front, the curvature will increase due to the contribution from the R-X plane (curvature is counted in two directions.).

Figure 6-8 is the streamline plot for $Re=500$ and $We=2.63$ at $time=6.0$. Similar with the case in group one, in the two-phase zone, the streamlines are relatively straight for both phases. The difference is that slightly more bending of the gas streamlines near the top of the liquid core for the current case is observed due to the liquid core deformation.

Figure 6-9(A) shows the U velocity profile at different axial locations at $time=6.0$. These profiles are very similar to those in Figure 6-2 for group one. The velocity distribution at the exit also achieves the fully developed parabolic profile and again it shows that the current code can maintain a global conservation of mass very well. In Figure 6-9(B), the U velocity profile at the exit is compared with the theoretical result of a fully developed velocity profile and the two match with each other very well. Although there is a relatively large deformation, the SIMCC can still strictly maintain the conservation of mass.

The effects of different surface tension strengths are shown in Figure 6-10 for the three different Weber numbers. It must be emphasized here that the corresponding inlet pressure boundary conditions between the two phases are also different due to differences in surface tension coefficients. In this figure, as expected it shows that the degree of liquid phase shape deformation is inversely proportional to the Weber number as the higher Weber number the lower the surface tension coefficient as a relatively flat interface corresponds to very small surface tension. It is noted that the degree of deformation is not a linear function of the Weber number. As given in Figure 6-10, the difference in deformation between $We = 26.3$ and $We = 263$ is much less than that between $We = 2.63$ and $We = 26.3$ even though for both cases the change in the Weber number is one order of magnitude.

Figure 6-11 shows the liquid core deformation as a function of time as it moves downstream for the case with $We = 2.63$ and $Re = 500$. The results show that the degree of deformation increases with time as the liquid plug travels downstream.

6.2.3 Two-Phase Flow Pressure Drop

As indicated in the above, the pressure gradient in the two-phase flow is much higher than that in the single-phase flow. It is important to summarize the effects of different Reynolds numbers and Weber numbers on the magnitude of increase in pressure drop in the two-phase zone. The ratio of the averaged local friction coefficient in the two-phase zone to the fully developed single-phase gas flow friction coefficient is plotted in Figure 6-12 as functions of the Reynolds number and the Weber number. In Figure 6-12(A), it is seen that the friction coefficient ratio increases with increasing Reynolds number almost linearly. The increasing trend of the ratio with the Reynolds number is thought to be due to the increased drag between the two phases as the Reynolds number gets higher, while the trend for different Weber numbers is totally different as shown in Figure 6-12(B). The friction coefficient ratio decreases exponentially in the low Weber number regime and then relatively flattens out with a very small gradient. This trend is readily explained by the degree of shape deformation as shown in Figure 6-10: more deformation will result in higher drag between the two phases. A much larger change in shape between $We = 2.63$ and $We = 26.3$ than that between $We = 26.3$ and $We = 263$ is noted. As a result, the drop in friction coefficient ratio is much larger between $We = 2.63$ and $We = 26.3$ than that between $We = 26.3$ and $We = 263$.

6.3 Grid Refinement Study

In the numerical simulation, the results may be not accurate due to the resolution of grid especially for the coarser grid system. In this section a grid refinement study is performed to ensure the adopted resolution of grid system is fine enough in this research. The case with

We=2.63 in section 6.2.2 is adopted here. There are three grid resolutions selected. The minimum grid lengths are 0.02, 0.01 and 0.005. Figure 6-13 shows the locations of interface by the three grids at the same time and it shows that there is not much difference between three interfaces. In order to save computational time while preserving accuracy, unless otherwise mentioned, all following simulations in this study will adopt 0.01 as the minimum grid spacing.

6.4 Liquid-Gas Two-Phase Flows in a Pipe with Heat Transfer

In this section, for the sample calculations, the selected two phase fluids are liquid water and air at 1 ATM. The physical conditions of the two-phase flow and heat transfer system are described as follows. In the beginning ($t = 0$) the pipe is filled with only air which is in thermal equilibrium with the wall at 373.14 K. When the transient starts ($t > 0$), the gate at the inlet of the pipe is opened and an annular two-phase flow with water in the center core and air filling the space between the wall and the water, both phases at 273.15K, are entering the pipe at the same and uniform velocity. The wall is maintained at 373.14 K during the transient. With this maximum temperature difference between the two phases, there is no phase change and only sensible heat transfer at the liquid-gas interface. The selected two phase fluids are liquid water at 273.15K and air at 373.14K. The ratios of fluid properties of two phase flows are:

$$\frac{\rho_l}{\rho_g} = 1055.07 ; \frac{\mu_l}{\mu_g} = 81.39 ; \frac{k_l}{k_g} = 17.99 ; \frac{Cp_l}{Cp_g} = 4.17$$

The corresponding Prandtl number for water should be:

$$Pr = 13.0$$

The time step in this computation is set as 0.001.

It is noted that for the current system, there are three dimensionless parameters, Reynolds, Peclet and Weber numbers that must be specified. For the Weber number, two cases are selected, one low Weber number at 2.63 and the other high Weber number at 500. Different Weber

numbers can be used to evaluate the effects of shape deformation. The Reynolds and Peclet numbers for the current study are selected as

$$Re = 500 ; Pe = 6500$$

In the high Weber number case, extra two cases: (1) $Re = 250$ and $Pe = 3250$ and, (2) $Re = 1000$ and $Pe = 13000$ are also provided to investigate the effects of different Reynolds and Peclet numbers.

6.4.1 Low Surface Tension Case

For this case, the Weber number is set at 500 such that the inertia force overwhelms the surface tension force. As a result the shape change of the liquid slug is relatively small. In Figure 6-14, the pressure and flow field results are presented. The bold dashed line represents the location of the liquid-gas interface. Figures 6-14(A) and (B) show the isobaric pressure contours on the R-X plane at time= 5.5. In Figure 6-14(A), it is seen that the pressure decreases linearly in the streamwise direction for both phases. In general, the magnitude of shear stress at the wall and the pressure jump across the liquid-gas interface determine the pressure gradients in the liquid phase. Therefore the pressure of the liquid phase is larger than that of the gas phase at the same downstream location due the surface tension effect that causes a pressure jump at the interface. In the liquid phase away from its frontal area, as indicated in Figure 6-14(B) where the pressure contour near $X=3$ is focused locally, it shows that the pressure jump across the interface is very close to the theoretical value ($p_l - p_g \sim \kappa / We \sim 2.63/500 = 0.00526$ as the curvature is 2.63 obtained from Figure 6-14(D)) since the liquid pressure is influenced and controlled by the gas phase because that the liquid phase is fully surrounded by the gas phase that carries the bulk of the inertia force. In general, there is no pressure gradient in the radial direction for both phases. At the front of liquid slug, the curvature increases to 5.5 as shown in Figure 6-14(D) because of

the additional curvature in the R-X plane and therefore, the pressure jump in the front of the liquid core can be estimated as $5.5/500=0.011$ and this pressure jump can be verified in Figure 6-14(C) where the pressure distribution along the centerline is plotted. After the front of liquid core, the gas flow diffuses into a single phase flow occupying the entire pipe. For downstream locations far away from the liquid front, the pressure decays linearly as the flow adjusts into a fully developed single-phase pipe flow. Figure 6-14(E) is a streamline plot. In Figure 6-14(E), it shows that the streamlines deform in the immediate downstream of the liquid front towards to the centerline of the pipe in the single-phase region. Because of the non-slip condition and continuity requirement, the fluid near the solid wall will be pushed toward to the center of pipe and the maximum velocity takes place at the centerline when the single-phase flow is fully developed. In Figure 6-14(F), it shows that the velocity profile at the outlet of pipe reaches the fully developed condition. Also, in the two-phase region, due to a large density difference, the gas flow can not affect the liquid substantially, therefore, the gas phase must take the form of jet flow to satisfy the continuity and it can be seen in Figure 6-14(F). Similarly, the shape of the liquid core will not deform too much and the interfacial velocity is close to the inlet velocity (~ 1.0). Based on results provided in Figure 6-14, it shows that the current numerical method can accurately enforce the interfacial condition, the continuity, and momentum equations for the flow field computation.

Next, the heat transfer results are presented. Figure 6-15 is the isothermal temperature contour and the interfacial temperature distribution for the case of $We=500$, $Re=500$ and $Pe=6500$ at different time steps of 1.5, 3.5, and 5.5.

According to Figures 6-15(A-C), they basically show that the moving liquid slug is a heat sink with a large capacity, because the thermal capacity in the liquid phase is much larger than

that in the gas phase, the temperature changes in the liquid core are much less than those in the gas phase. The heat transfer in the gas annular portion is mostly fully developed as the isotherms are parallel to one another after a very short entrance region. The isotherms then bend to become relatively parallel to the liquid slug frontal area that again shows the flow field effects and the heat sink nature of the liquid phase. Since this is an unsteady computation, the highest temperature of liquid core is located at the right-upper corner because this local region is heated by the gas phase of the highest temperature gradient. In Figure 6-15(D), the time-dependent temperature distributions of the liquid-gas interface are plotted, which basically demonstrates the heating up of the horizontal portion of liquid phase and much less heat transfer in the vertical frontal portion.

The general heat transfer effectiveness from the pipe wall is measured through the dimensionless Nusselt number, Nu , as defined below:

$$Nu = \frac{h_s D}{k_s} = \frac{\dot{q}_s'' D}{k_s (T_s - T_m)} \quad (6-2)$$

where \dot{q}_s'' is the heat flux from the solid pipe wall to the gas flow and T_m is the mean flow temperature at each downstream location that includes the contribution from both phases in two-phase region. The Nusselt number along the pipe wall in the downstream direction have been plotted in Figure 6-16 for the case of $We=500$, $Re=500$ and $Pe=6500$ at three instants of $t = 1.5$, 3.5 and 5.5 . As can be seen from Figure 6-16, the Nusselt number value is basically a reflection of the respective heat transfer mechanism that is dictated by the flow field. In the region from the entrance to around $X = 0.5$, the Nusselt number takes a sharp drop from a large value to reach a value of 8.9 that is the so-called entrance region. After the relatively very short entrance region, the heat transfer is fully developed and the fully developed portion is continued until reaching the frontal area of the liquid slug. After the liquid front, the Nusselt number goes through a sharp

decrease again as the gas flow adjusts to the single phase condition. The adjustment portion is also very short and the Nusselt number quickly approaching the value of 3.66 which corresponds to the Nusselt number for a fully developed single-phase flow in a circular pipe with a constant wall temperature. It is worth noticing that the enhancement of heat transfer due to a liquid slug is quite extensive as that the heat transfer is increased more than 140% (Nu from 3.66 to 8.9). The gas jet flow in the two-phase region raises the Nusselt number from 7.3 (pure conduction in the annulus) to 8.9.

The effects of the Reynolds number on the heat transfer in the two-phase region are examined in Figure 6-17. Figure 6-17(A) shows the Nusselt number distributions for $Re=250$ ($Pe=3250$), 500 ($Pe=6500$) and 1000 ($Pe=13000$) at $time=5.5$. First, it shows that the entrance length is proportional to the Reynolds number even though the entrance lengths for all three cases are relatively short. For the Nusselt numbers in the fully developed region, as expected, it shows that the higher the Reynolds number, the higher the Nusselt number as the Peclet number is proportional to the Reynolds number. But the differences among the three Nusselt numbers are less than 0.03 as seen in the close-up around $X = 4.7$, therefore the Reynolds number effect is really small. Figure 6-17(B) provides the temperature profiles for the liquid-gas interface for the three different Reynolds cases. The heating of the liquid slug is relatively faster for the lower Reynolds number. This is due to the fact the more heat is convected downstream to the single-phase region rather than to the liquid slug for higher Reynolds numbers.

6.4.2 High Surface Tension Case

For this case, the Weber number selected is 2.63 to represent the condition where the surface tension is dominant over the inertia. The Reynolds number and the Peclet number are maintained at 500 and 6500, respectively for this case. Under a large surface tension force, liquid slug would exhibit a substantial shape change near the upper-right corner as shown in Figure 6-

18. The result of a dominant surface tension force in a two-phase flow is the roll up of the liquid slug front around the top corner. Therefore, the interface near the front of liquid core will deform to pull backward.

Figure 6-19 displays the isothermal temperature contours and the liquid-gas interfacial temperature profiles at different times of $t = 1.5, 3.5,$ and 5.5 . Basically, the general trends of the heat transfer characteristics for the low Weber number case are similar to those in the high Weber number case but there are some differences due to the shape change that will be discussed below.

In Figures 6-19(A-C), it shows that the interface near the front of liquid core deforms as the liquid plug moving downstream. Because of the substantial deformation at the front of the liquid core, the cross-sectional area of gas phase between the liquid phase and solid wall decreases, that results in the local acceleration of the gas velocity. The increased gas velocity around the deformed liquid frontal area enhances not only the convective heat transfer from the pipe wall but also the heating of the liquid phase. In Figure 6-19(D), the higher interface temperatures at the deformed portion of the liquid slug reflect the enhanced heat transfer from the gas flow. As the liquid phase deforms more when moving further downstream, the affected interface temperatures also rise higher.

The Nusselt number distribution along the pipe wall is given in Figure 6-20. Again, the general trends are similar to those for the high Weber number case except that there is a local peak corresponding to the enhanced heat transfer due to the deformation of the liquid slug front corner as explained above. The local heat transfer increases range from 10% at time=1.5 to 20% at time=3.5 and then to 30% at time=5.5. The general heat transfer enhancement over the pure

conduction case in the annular region and the smooth transition from the two-phase region to the fully developed single-phase region are all similar to those in the high Weber number case.

To facilitate a close comparison between the high and low Weber number cases, Figure 6-21 is provided for this purpose. Figure 6-21(A) is a comparison of the interfacial temperatures for the low and high surface tension cases at the same time instant. Starting from the inlet and continuing until the deformation begins, the two curves are almost overlapped with each other because both the gas flow and the geometry are very similar. Near the deformed liquid area, there is about 50% temperature difference. At the relatively vertical front of liquid core, the temperature differences between the two cases become very small because the heat transfer is no longer affected by the shape deformation. In Figure 6-21(B), it is the comparison of the Nusselt number distributions. The only difference between the two cases is again due the deformation which causes a maximum 25% increase in the local Nusselt number at the peak location.

6.5 Summary

In this chapter, the liquid-gas two-phase flows in a pipe without phase change are computed and it includes the isothermal and pure heat transfer cases.

For the isothermal case, it shows that velocity fields and pressure distributions were correctly computed for both two-phase and single-phase zones and a smooth transition between the two was also obtained. In the two-phase zone, the liquid velocity profile is basically unidirectional and uniform while a jet profile was found in the gas phase. Almost immediately downstream of the liquid core front, the single-phase gas flow establishes the fully developed parabolic profile. The pressure is virtually independent of the radial direction and the pressure distribution in the axial direction is composed of two straight lines of different slopes for the two-phase and single-phase zones, respectively. The dimensionless pressure gradient in the two-phase zone is inversely proportional to the Reynolds number. The ratio of the averaged local

friction coefficient in the two-phase zone to the fully developed single-phase gas flow friction coefficient increases with increasing Reynolds number almost linearly, whereas this ratio decreases exponentially in the low Weber number regime and then relatively flattens out with a very small gradient for intermediate and large Weber numbers. The liquid core shape deformation is relatively insensitive to the Reynolds number, however the deformation is large for small Weber numbers and is negligible for intermediate and large Weber numbers.

For the case with heat transfer, irrelevant to the Weber number, in general the moving liquid slug in the central core which induces a jet gas flow in the annulus between the pipe wall and the liquid slug serves as the main heat sink of a large capacity. The combination of the gas jet flow and the large sink capacity in the two-phase flow region results in a heat transfer increase of more than 140% over that in a fully developed single-phase flow. Immediately downstream of the liquid slug, the gas flow adjusts quickly to establish as a fully developed single-phase flow and the local Nusselt number along the pipe wall reflects that process. The effect of different Reynolds numbers on the heat transfer in the two-phase region is negligibly small. For the low Weber number case where the surface tension substantially over-weighs the inertia force, the resultant shape change in the form of roll-up and bending backwards around the upper corner of the liquid slug reduces the local gas flow area in the annulus. This flow area reduction creates a increase in the gas velocity that in turn causes a local heat transfer enhancement ranging from 10% to 30% depending on the length of time the liquid slug spends in the pipe.

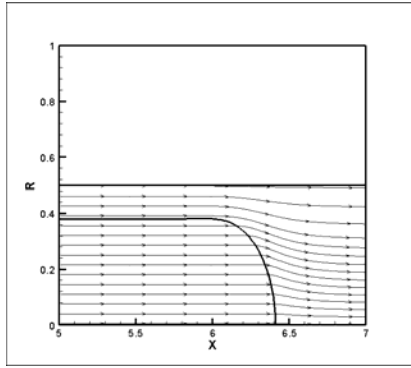


Figure 6-1. Streamline of the isothermal case at time=6.0 with $Re=2000$ and $We=500$.

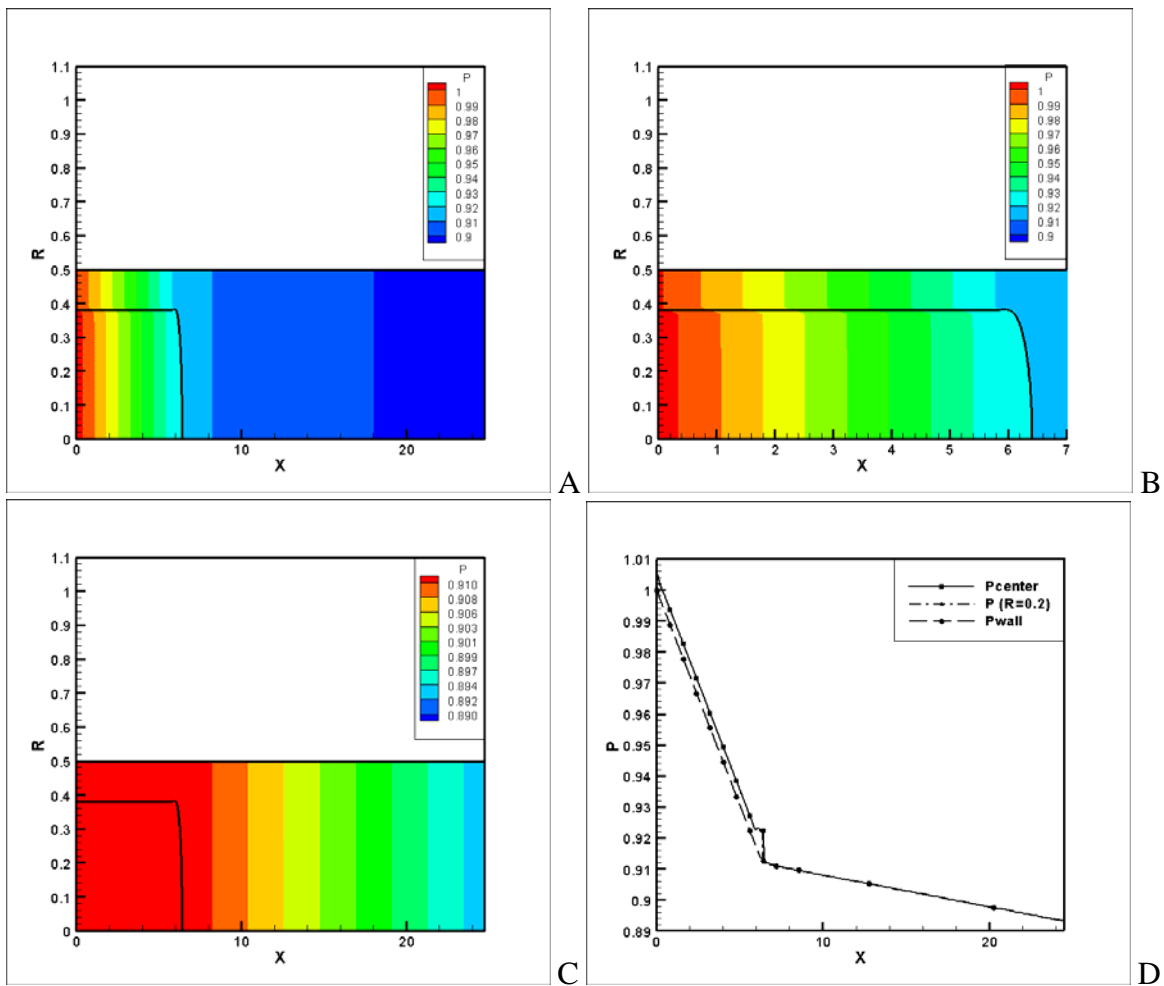
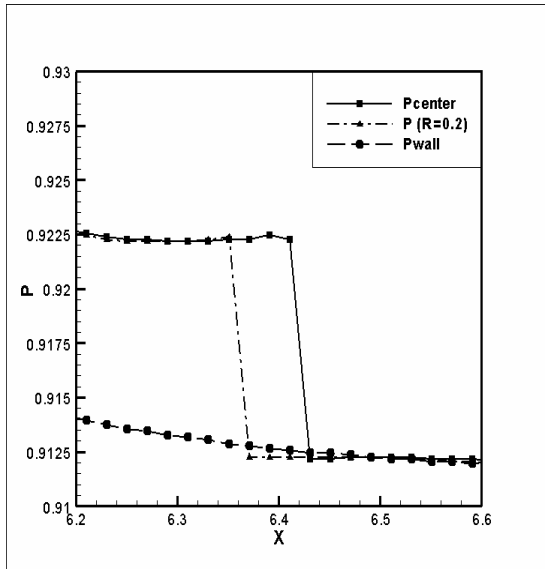
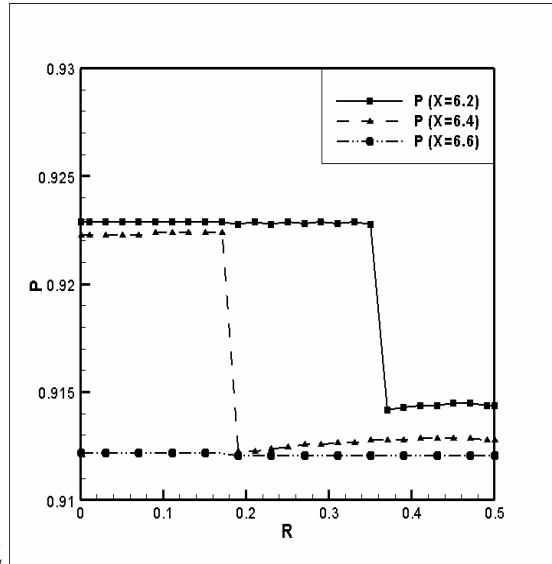


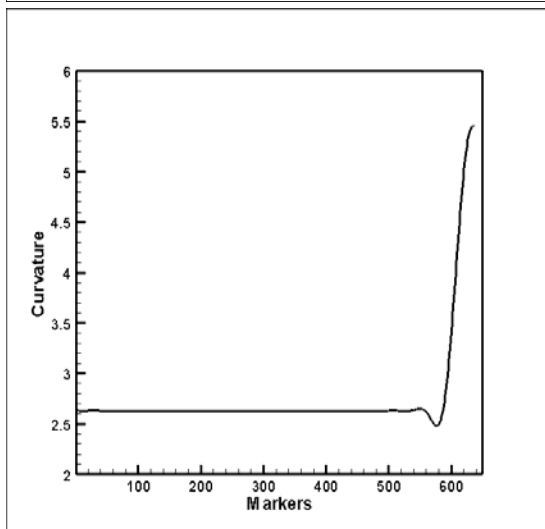
Figure 6-2. The pressure contours/distributions at time=6.0 with $Re=2000$ and $We=500$. A) entire pressure contour, B) near the entrance, C) downstream part, D) distribution at center and wall, E) at different locations along axial direction near the front of liquid core, F) at different locations along radial direction near the front of liquid core, G) curvature along interface.



E



F



G

Figure 6-2. Continued.

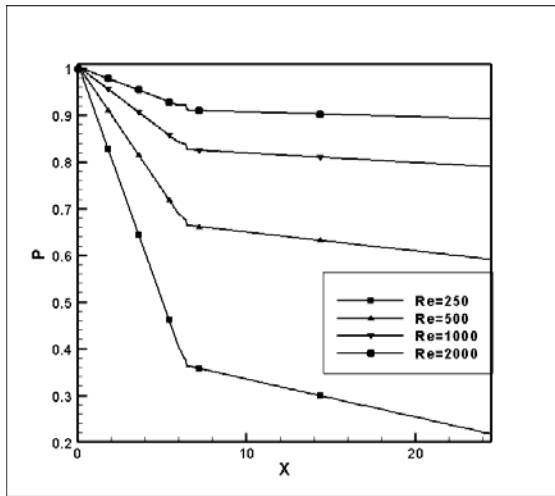


Figure 6-3. The pressure distributions along the centerline based on different Reynolds numbers at time=6.0.

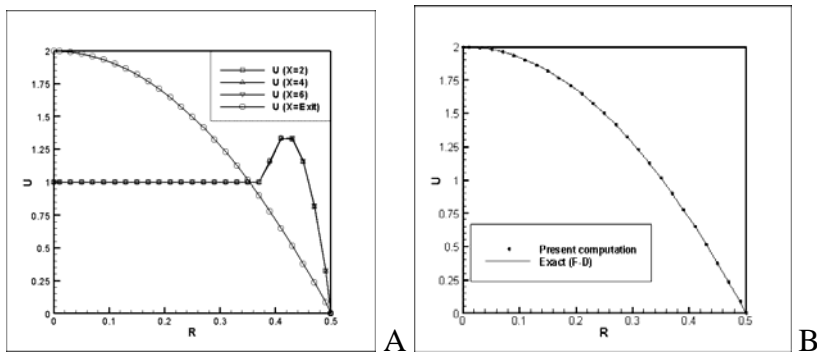


Figure 6-4. The U velocity profile at time=6.0 with Re=2000 and We=500. A) at different locations, B) comparison of velocity at the outlet.

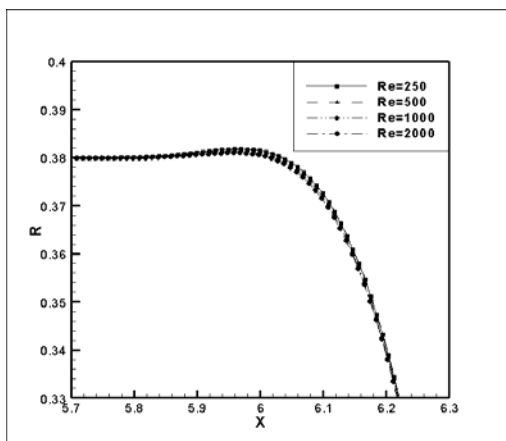


Figure 6-5. Shapes of liquid cores with different Reynolds numbers at time=6.0.

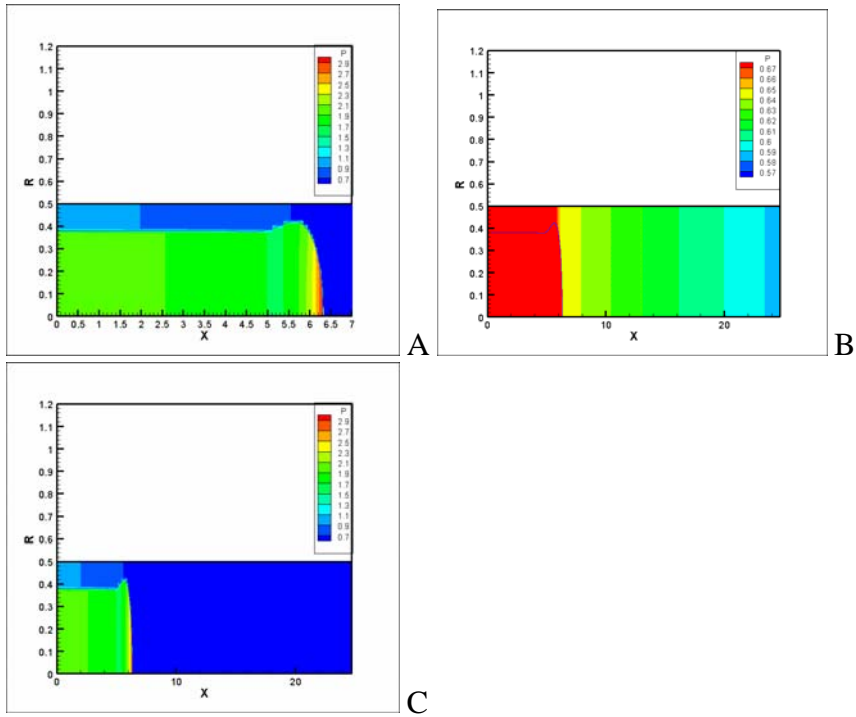


Figure 6-6. The pressure contours at time=6.0 with $Re=500$ and $We=2.63$. A) two-phase zone, B) single-phase zone, C) entire domain.

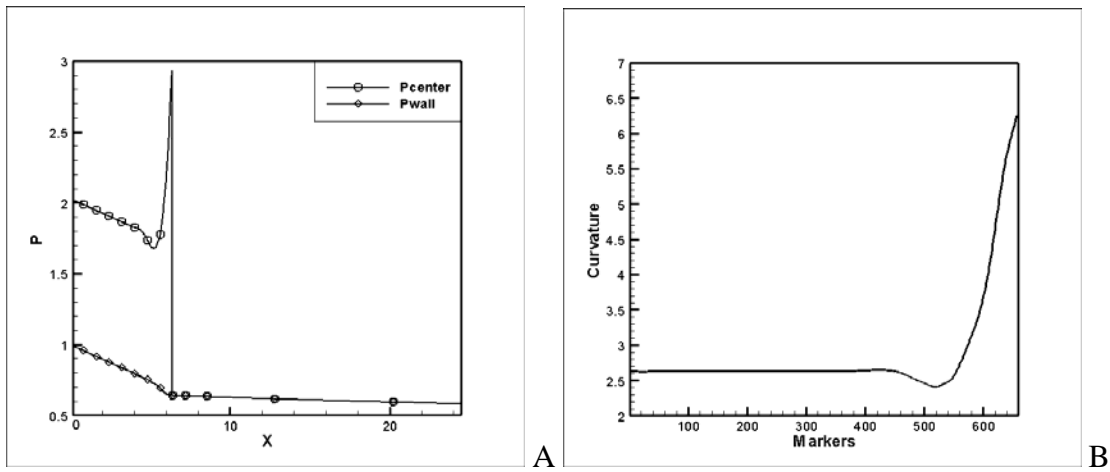


Figure 6-7. Pressure distribution and the curvature of interface at time=6.0 with $Re=500$ and $We=2.63$. A) pressure distribution, B) curvature distribution.

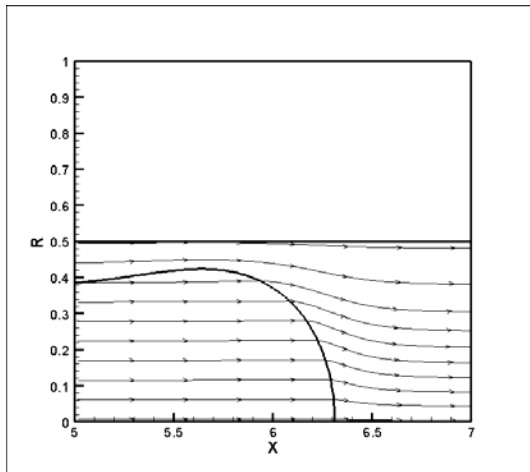


Figure 6-8. Streamline plot at time=6.0 with $Re=500$ and $We=2.63$.

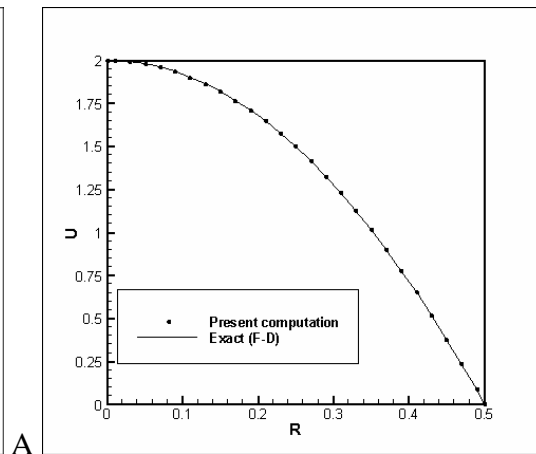
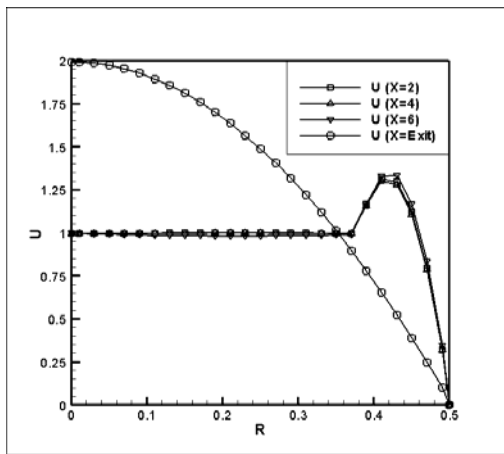


Figure 6-9. U velocity profile at time=6.0 with $Re=500$ and $We=2.63$. A) at different locations, B) comparison of velocity at the outlet.

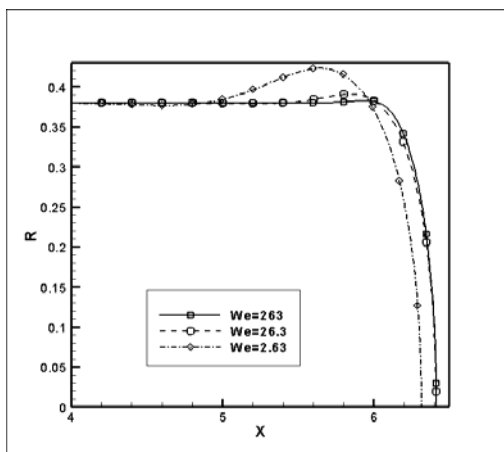


Figure 6-10. Shapes of the interface by different Weber numbers at time=6.0.

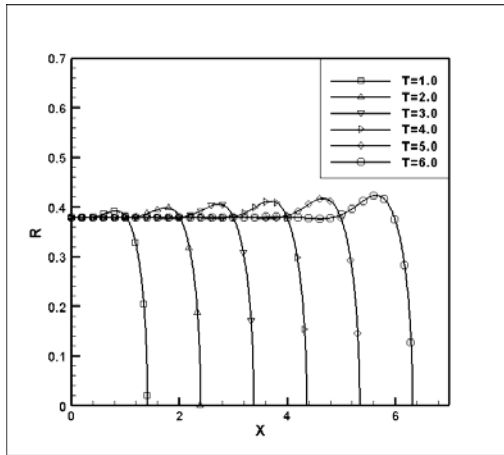


Figure 6-11. The development of interface with $Re=500$ and $We=2.63$ at different time steps.

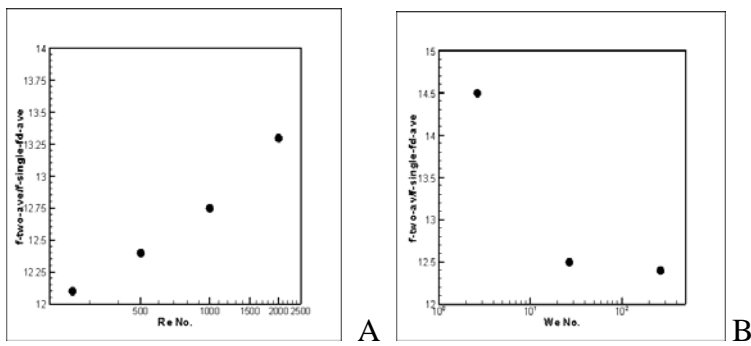


Figure 6-12. The ratio of averaged local friction coefficient in the two-phase zone to the fully developed single-phase gas flow friction coefficient. A) as a function of the Reynolds number, B) as a function of the Weber number.

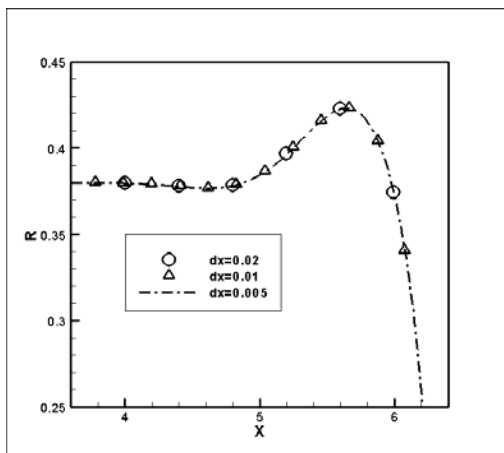


Figure 6-13. The computed interfaces by three different grid resolutions.

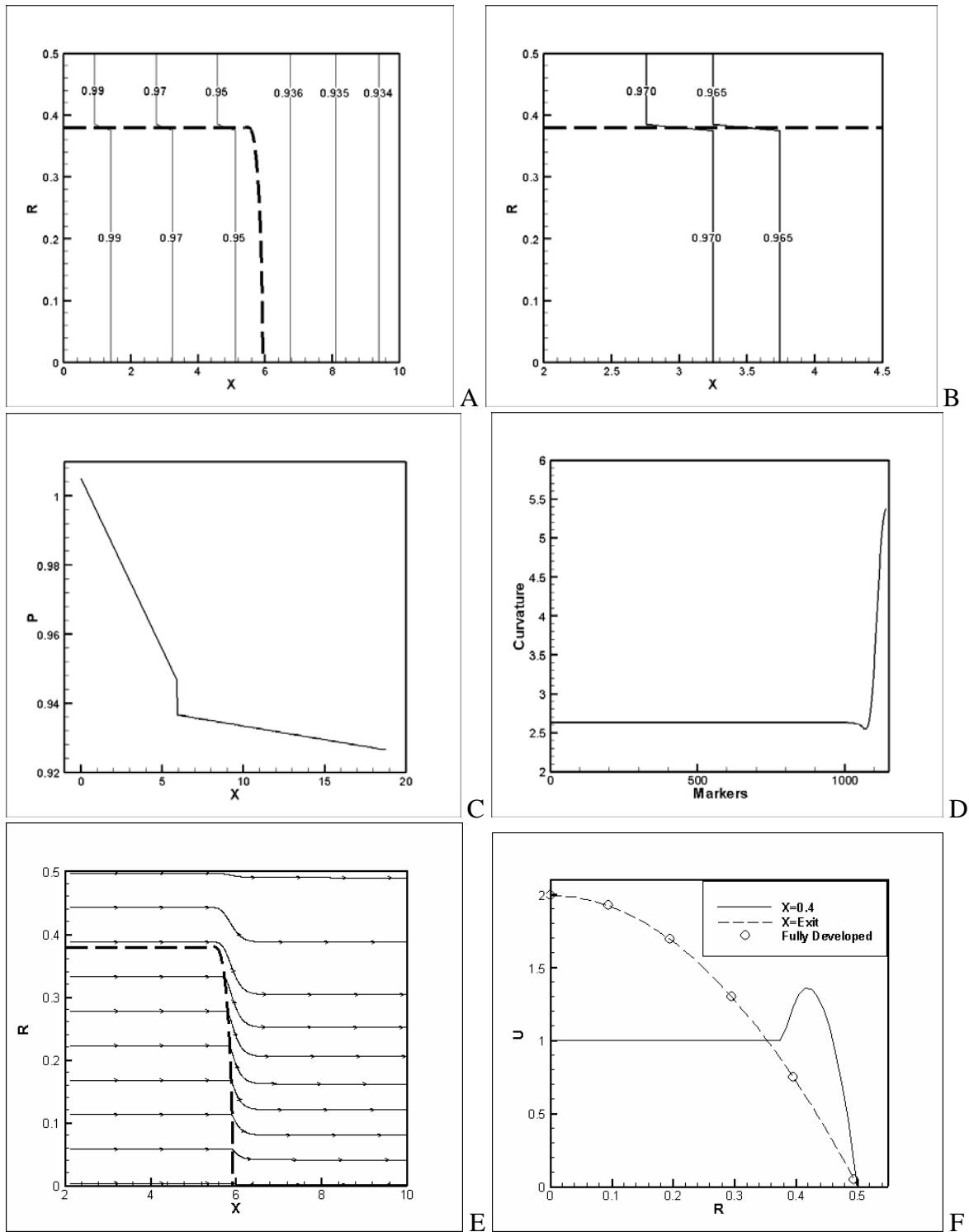


Figure 6-14. The pressure contours, pressure and curvature distribution, streamline plot and the contour of U component contour of the case with $Re=500$, $Pe=6500$ and $We=500$ at $t=5.5$. A) pressure contour, B) enlarged pressure contour near $X=3$, C) curvature distribution, D) streamline plot, E) U velocity component along radial direction.

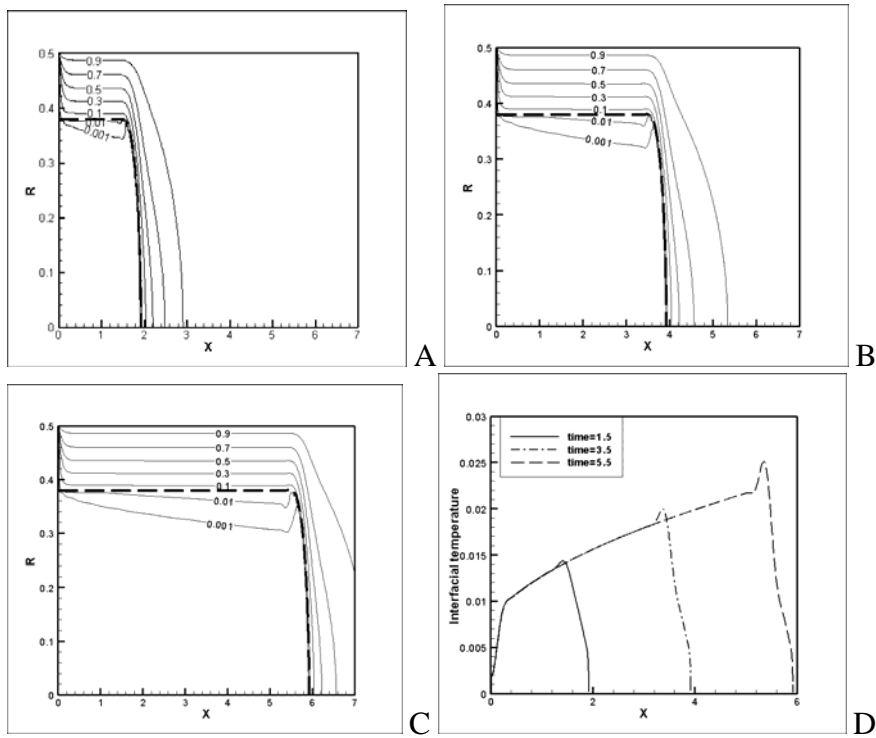


Figure 6-15. The temperature contours of two-phase plug flow and the interfacial temperature at different time steps with $Re=500$, $Pe=6500$ and $We=500$. A) time=1.5, B) time=3.5, C) time=5.5, D) interfacial temperature.

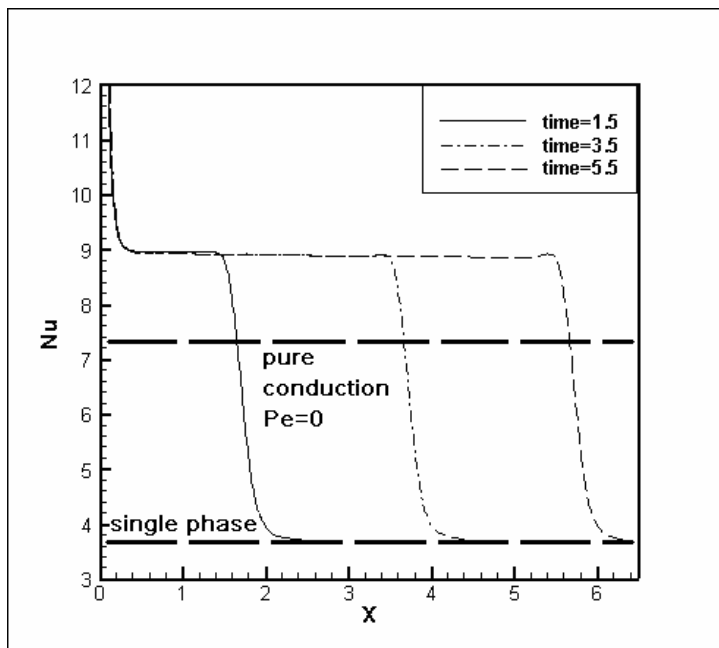


Figure 6-16. The Nusselt number at the solid wall at different time steps with $Re=500$, $Pe=6500$ and $We=500$.

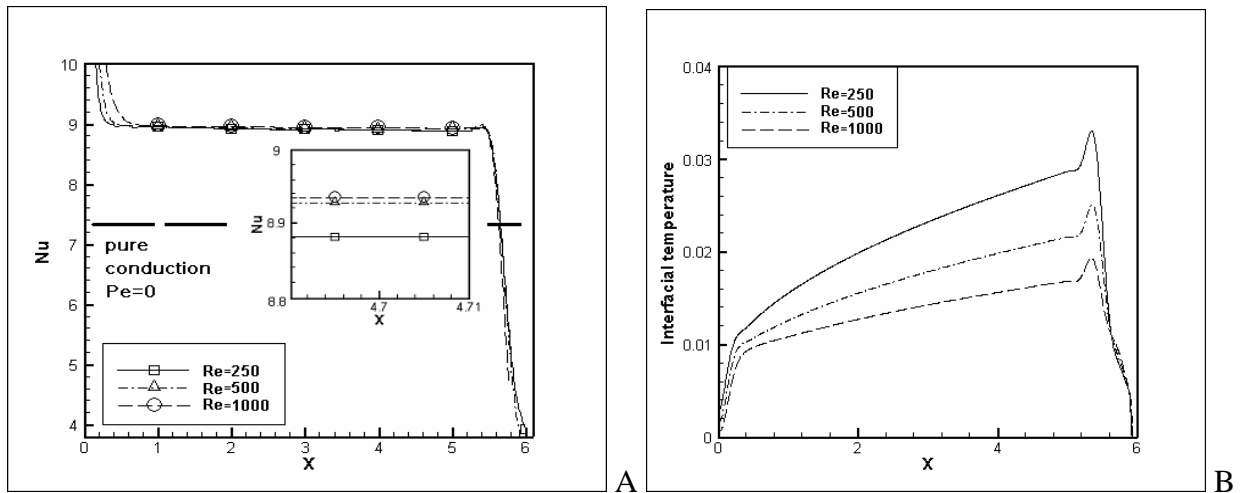


Figure 6-17. The comparison of interfacial temperature and Nusselt number at wall for different Reynolds number with $Pe=6500$ and $We=500$ at $time=5.5$. A) Nusselt number at wall, B) interfacial temperature.

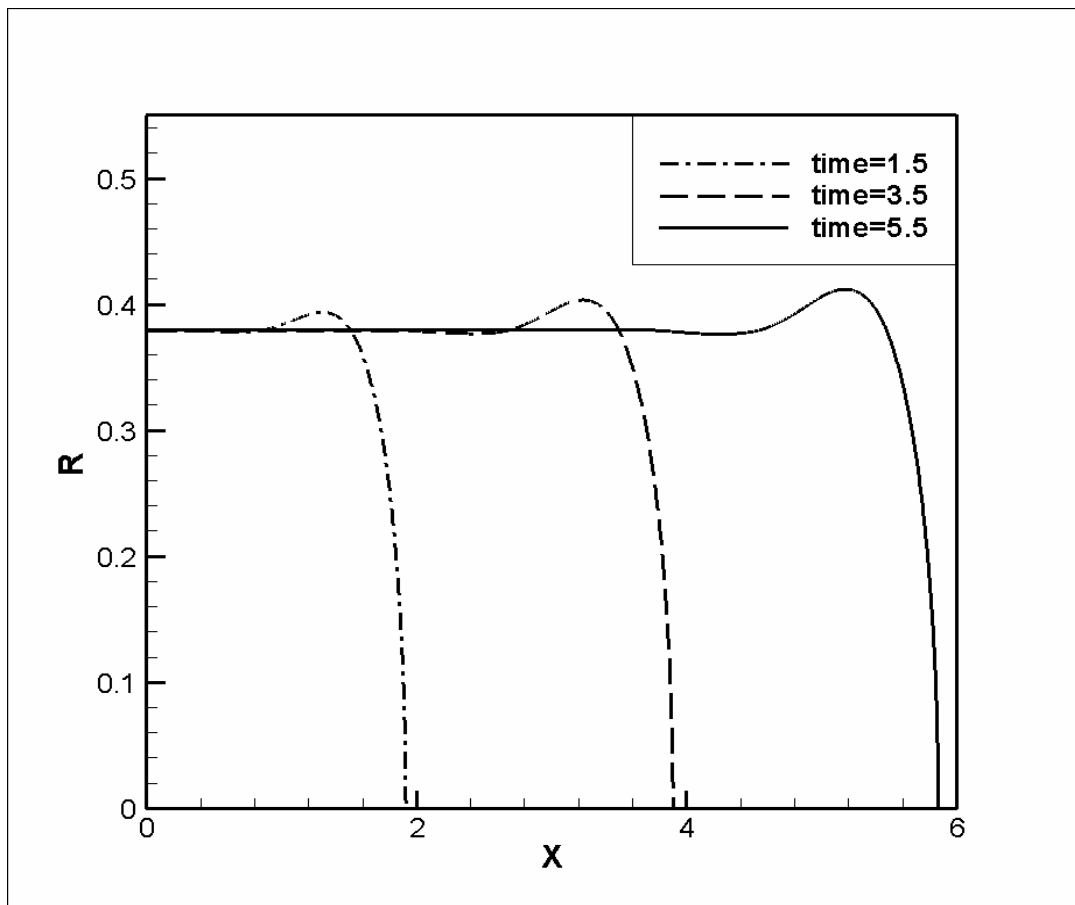


Figure 6-18. The shapes of the liquid slug at three different time steps for the case of $Re=500$, $Pe=6500$ and $We=2.63$.

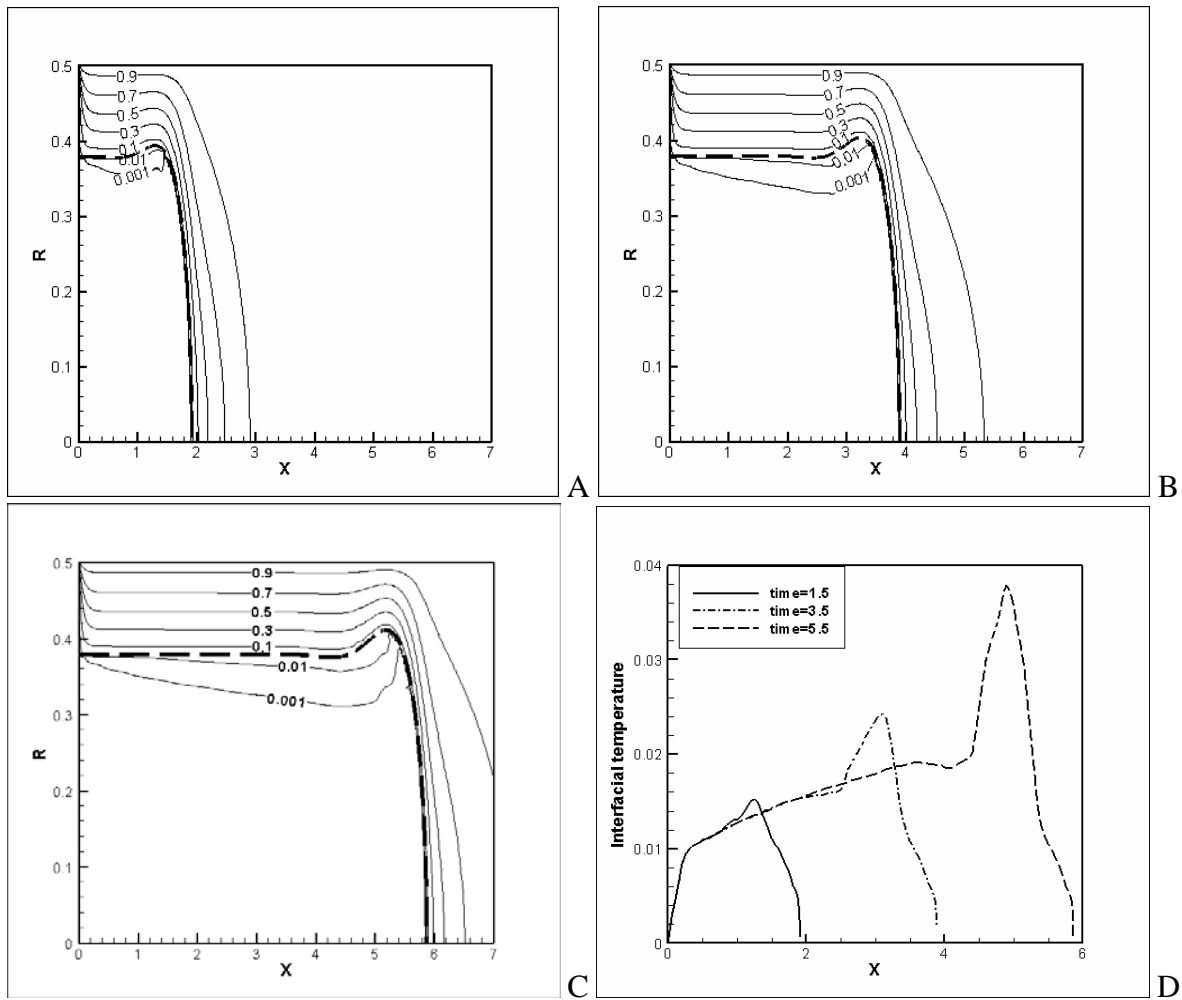


Figure 6-19. The temperature contour of two phase plug flow and the interfacial temperature with $Re=500$, $Pe=6500$ and $We=2.63$ at different time steps. A) time=1.5, B) time=3.5, C) time=5.5 and D) interfacial temperature.

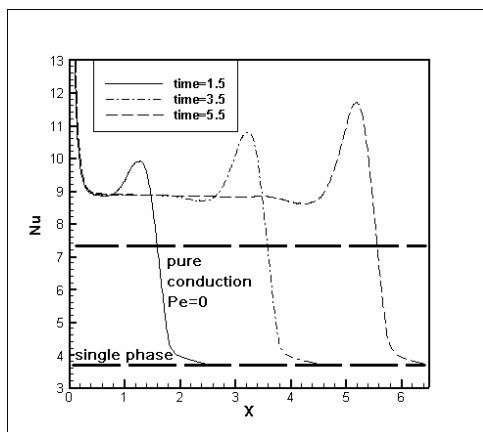


Figure 6-20. The Nusselt number at the solid wall $Re=500$, $Pe=6500$ and $We=2.63$ at different time steps.

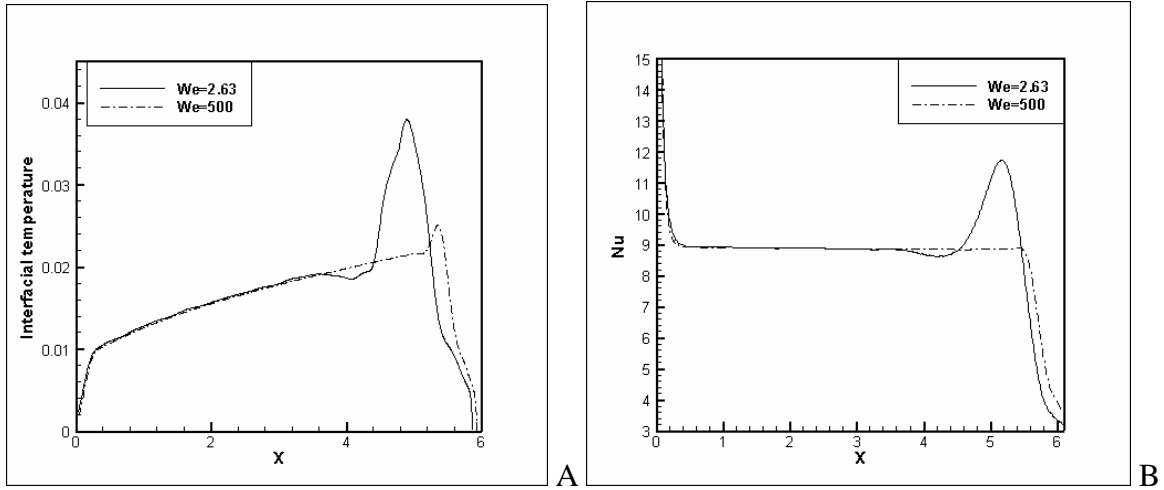


Figure 6-21. Comparison of the interfacial temperature and the Nusselt number with different Weber numbers. A) interfacial temperature, B) Nusselt number.

CHAPTER 7 LIQUID-GAS TWO-PHASE FLOWS IN A PIPE WITH PHASE CHANGE

7.1 Introduction

In this chapter, the text will focus on phase change computation. Based on thermodynamics, the temperature at the vaporizing liquid-gas interface is assumed as the saturation temperature corresponding to the system pressure and the pipe wall temperature is set to be higher than the saturation temperature. Therefore, as the liquid phase is also at the saturation temperature without any subcooling, the heat flux reaches the liquid-gas interface will be fully consumed to supply the latent heat because the temperature of liquid can not increase. As the phase change occurs, the gas mass flow rate downstream will increase due to the vaporization from the liquid surface that adds mass flows to the gas phase. Also, because of the large temperature difference assumed between the liquid phase and solid wall, the thermal radiation is considered. In the current approach, two kinds of heat transfer boundary conditions of the solid wall are considered. In the first case, the wall temperature is assumed to be constant, so that the heat flux comes from wall is relatively high and constant. This can represent the case with a very large wall heat capacity. In the more realistic situation, the wall temperature may not remain constant and it would be chilled down by the colder fluid in the pipe. In the second case, a finite wall heat capacity is assumed. It will focus on the impact of the pipe wall chilldown process on the two-phase flow and heat transfer. One refrigerant R-508B and two cryogenic fluids of liquid nitrogen and hydrogen are chosen as coolants. The diameter of the proposed pipe is 4 mm and inlet velocity is 10cm/s for both phases and the selected material for the wall is a Titanium alloy with $\rho = 4450 \text{ kg/m}^3$, $C_p = 4200 \text{ J/(kgK)}$, and $k = 4.8 \text{ W/(mK)}$

7.2 R-508B Refrigerant with Constant Wall Temperature

In this section, the selected fluids are the liquid and gas refrigerant R-508B at 208K and 248K, under 3 ATM. Its chemical formula is CHF_3 / CF_3CF_3 , 46/54% and its molecular weight is 95.39. Under this condition, the temperature at liquid phase is the saturation temperature for 3 ATM and will not change during the computation and the phase change should take place at the liquid-gas interface.

The main purpose of selecting this particular working fluid is to add a non-cryogenic case but its application is quite extensive.

The ratios of fluid properties for the two phases are:

$$\frac{\rho_l}{\rho_g} = 98.89; \frac{\mu_l}{\mu_g} = 21.74; \frac{k_l}{k_g} = 9.04; \frac{Cp_l}{Cp_g} = 1.53$$

The two fixed dimensionless parameters are:

$$Pr = 3.26, Ja = 0.034$$

The time step in this computation is set as 0.001. In the phase change computation, there are four dimensionless parameters in the governing equations and interfacial conditions, and they are Reynolds (Re), Peclet (Pe), Weber (We) and Jakob (Ja) numbers. Once the thermodynamic properties of working fluid and the temperature difference are decided, the only free dimensionless parameters are Reynolds and Weber numbers. In order to demonstrate the ability of the SIMCC code to handle the large deformation and change of volume due to the strong surface tension and phase change effects, the Reynolds and Jakob numbers are selected as 10.0 and 2.63, respectively. Figure 7-1 shows the contours of the U-velocity component at time =1.0, 2.5 and 4.0.

In Figure 7-1, the U-component contours show that there are two locations with higher U velocities in each contour plot. The first location is in the gas phase near the upper-right corner

of liquid core. Because of the vaporization at the upper surface of liquid core, the liquid will be vaporized as gas and enters the gas phase. It can be expected that the mass flow rate of gas will be increased before entering the single-phase region so that the velocity of gas is sped up till this location and results in the maximum velocity.

Figure 7-2 is the history of local maximum U-velocity of the gas phase near the upper-right corner of liquid core. It shows that the local maximum velocity increases as time increases but this trend is not linear. If there were no shape change for the liquid slug, then the maximum U-velocity history curve would be linear as the evaporating surface area would increase linearly with time and the rate of mass evaporation is proportional to the surface area. Also the distance between the pipe wall and the liquid core would stay unchanged. In the current case, the interface shape does change substantially due to a strong surface tension effect and phase change process. In Figure 7-3, it shows the interface shapes at different times. At $t = 4.0$, the maximum distance between the pipe wall and the liquid core is 0.24. The initial (time=0) maximum distance is 0.12. This explains why the curve in Figure 7-2 is not linear and the slope must decrease since the cross section of area of gas phase increases.

Another location with a higher velocity is at the center of the pipe. Near the wall, because of the non-slip condition and the continuity requirement, the gas is pushed to the centerline and also because of the mass flow from the two-phase upstream, the velocity at the centerline will be higher than other locations. Figure 7-4 is the streamline plot of the gas phase at time=4.0. By the distribution of streamlines, it does show that the streamlines are pushed to the center of the pipe and this means the gas is pushed to the center of the pipe.

Figure 7-5 shows the V-velocity component contour at different time steps. Downstream to the front of the liquid core, the flow of gas is pushed to the center so that the maximum negative

V-velocity is located near this region. This highest negative V-velocity component increases as time increases due to more vaporization from the liquid core. Near the centerline, the V-velocity component will be close to 0 and that means the gas flow turns its direction because of the symmetric condition. This conclusion can also be seen in Figure 7-5. In Figure 7-5, the phase change at the interface is much stronger at the beginning due to the initial condition. As time increases, it shows that the vaporization becomes weaker.

Figure 7-6 is the temperature contours at different time steps. To compare the gas temperatures near the front of the liquid core, it shows that the temperature gradient is much higher at time=1.0 due to the initial condition. At time=4.0, the gradient is much weaker because of the convective effect and also, the distance between the liquid core and the wall increases. It can be expected that phase change is very strong at beginning and becomes weaker as time increases.

Figure 7-7 is the Nusselt number evaluated at the solid-gas interface at different time steps. It shows that in general the Nusselt number decreases as time increases. By Figure 7-6, it is very clear that the thermal gradient decreases along the downstream direction so that the Nusselt number decreases with increased downstream location. In the single phase region, all three curves converge to the fully developed single-phase flow case very fast and the corresponding Nusselt number is 3.66.

Figure 7-8 shows the total mass flow rate of gas phase at the pipe exit. Basically, the trend is very close to that in Figure 7-2. The mass transfer rate increases as time increases but the slope of curve becomes smaller as time increases.

7.3 Constant Wall Temperature Case with Liquid Nitrogen

In this section, the working fluid is nitrogen with liquid and gas phases at 77K and 300K, respectively under 1ATM. Under these conditions, the temperature at liquid phase is the

saturation temperature and will not change during the computation and vaporization take place at the liquid-gas interface.

The ratios of fluid properties of two phases are:

$$\frac{\rho_l}{\rho_g} = 706.91; \frac{\mu_l}{\mu_g} = 8.85; \frac{k_l}{k_g} = 5.41; \frac{Cp_l}{Cp_g} = 1.97$$

The corresponding ratio of the Prandtl number for both phases should be:

$$\frac{Pr_l}{Pr_v} = 3.21$$

The time step in this computation is set as 0.001.

Three sets of dimensionless parameters are considered based on the fluid properties and geometry. They are listed in Table 7-1.

7.3.1 Flow Field with the Constant Wall Temperature Case

Since the heat transfer and phase-change process is closely related to the two-phase flow structure, a typical flow field shown in Figure 7-9 will be examined first that provides the velocity vector and streamline plots for Case 2 at time=1.5. Once the phase change is involved, the liquid will be vaporized and infuse into the gas stream so that the gas flow field is constantly changing with the mass flow rate and velocity increasing with increased downstream positions and the flow patterns are changed accordingly. For the liquid phase, it is a very simple unidirectional slug flow, while the gas phase is basically a continuously changing and accelerating annular jet flow due to the vaporization from the liquid surface. As seen in the streamline plot, the lines that originate from the liquid-gas interface represent the vaporization mass fluxes. The streamline density gets very high near the front of the liquid slug, that results in the maximum velocity in the two-phase region.

After the maximum jet velocity, the gas flow diffuses into a pure single-phase region and the gas flow becomes fully developed relatively quickly.

Figure 7-10 shows the U-component velocity contours for all three cases at time=1.5. To compare the three cases, the flow patterns are very similar to one another and the maximum velocities of three cases are all located near the upper-right of the liquid core which is the intersection between the two-phase region and the single-phase region. These flow structures are consistent with the velocity vector plot given in Figure 7-9. Due to the conservation of mass, the mass flow rate of the gas phase at each downstream cross section of the pipe should be the same in the single-phase region (about $X > 2.0$) as there is no more source of mass transfer. Therefore, the velocity decreases as the area of the cross section of the pipe increases in the single-phase region.

Figure 7-11 is the V-component velocity contours for all three cases at time=1.5. Again, they are all similar to one another also. By Figure 7-11, the highest vertical velocities are located on the horizontal portion of the liquid-gas interface where the vaporization rate is the highest accordingly. Immediately downstream of the front of the liquid core, it shows that the V-component velocities are negative and possess the maximum values because the gas must rush downward to fill the entire pipe. Far away from the front of the liquid core, the V-component decreases very fast and approaches zero as the single-phase becomes fully developed.

Figure 7-12 gives the value of the maximum gas velocity for each of the three cases and a relatively linear relationship is found for the maximum gas velocity with the Reynolds number.

Based on Table 7-1, the case with a lower Reynolds number is also with a lower Peclet number. By the conservation of energy, the vaporization mass flux, at liquid-gas interface is proportional to Ja/Pe as given below:

$$\left\{ \begin{array}{l} \dot{m}'' = \rho_g ((u_n)_g - (u_n)_{\text{int}}) \\ ((u_n)_g - (u_n)_{\text{int}}) \propto \frac{Ja}{Pe} (\bar{\nabla}T_g) \\ \dot{m}'' \propto \frac{Ja}{Pe} (\bar{\nabla}T_g) \end{array} \right. \quad (7-1)$$

Therefore, the case with a lower Peclet number will experience a higher evaporation rate that contributes to a higher maximum velocity. But it should also be noted that the gas temperature gradient term in the above equation would be slightly higher at a higher Reynolds number due to forced convective heat transfer in the annulus, however this effect is less significant than that due to the Peclet number.

Figure 7-13 is the temperature profile contour of the three cases at time=1.5. For all three cases, they all belong to the category of a high Peclet condition, so the contours are very similar to one another. Under a high Peclet number, the convection is dominant as can be seen in those temperature profiles that the heat transfer in the two-phase region corresponds to parallel isotherms due to a fully developed annular flow. In the single-phase region, the temperature profiles quickly establish the form of a fully developed pipe flow heat transfer.

Figure 7-14 plots the liquid-gas interface shapes for the three cases at time=1.5. As the interface shape deformation is strongly dependent on the Weber number and the three cases almost have relatively the same Weber numbers, so it can be expected only slight differences among them. This is indeed the case as shown in Figure 7-14. Near the entrance of the pipe, the three interfaces almost overlap. Near the front of the liquid core, intrinsically the deformation of the interfaces is more substantial for each case due to the magnitude of surface tension effect (different *We* numbers). Higher Weber numbers imply a lower surface tension effect and therefore, the case with the smallest Weber number (Case 3) deforms more than the other two cases.

Using the liquid slug shape as a basis for the evaluation of the grid size requirement, a grid refinement test is done to ensure the results obtained will not be influenced by the grid resolution. There are three grid sizes selected and they are 0.005, 0.01 and 0.05. The parameters for Case 3 are employed for the evaluation study. Figure 7-15 shows the interfaces for the three grid sizes at $t=1.5$. It is seen that there is not much difference among the three grid lengths and the selected grid length of 0.01 is adequate for the current numerical computations.

7.3.2 The Mass Transfer at Interface with Constant Wall Temperature

In this section, it focuses on the evaporative mass transfer process at the liquid-gas interface. As shown in the previous section, the mass transfer rate is represented by the difference between the velocities at the interface and accordingly the evaporation rate is dominated by the gas phase temperature gradient, the Jakob and the Peclet numbers. Previously, Figures 7-13 shows that temperature distributions are similar in the two-phase region for all three cases. In Figure 7-14, there is only a small difference near the front of the liquid core where the distance between the solid wall and the liquid surface is the shortest for Case 3 that results in a highest gas phase temperature gradient locally. Figure 7-16 (A) is the computed temperature gradients of three cases along the interface marker points at time=1.5. Figure 7-16 (B) provides the locations of markers.

In Figure 7-16(A), all three curves are similar except near the front of the liquid core, where the temperature gradient for Case 3 is larger than others because the distance between the liquid surface and the solid wall is the smallest for this case. At the entrance, because of the inlet boundary conditions, the temperature gradient is zero. At the front of the liquid core, because the distance between liquid slug surface and the solid wall becomes longer, the temperature gradient becomes smaller in all the three cases.

Because the gradients of temperature of these three cases are similar along most part of the interface, the ratio of mass transfer rate at the interface for these three cases can be estimated by Equation 7-1. By Table 7-1, all three cases have the same Jakob number so that the mass transfer rate is inversely proportional to the Peclet number:

$$\dot{m}'' \propto \frac{1}{Pe} \quad (7-2)$$

Since the Prandtl number is the same for all three cases, the evaporation rate should also be inversely proportional to the Reynolds number. Figure 7-17 is the total mass flow rates measured at the outlet of pipe for the three cases at time=1.5 and as expected the mass flow rate at the exit is inversely proportional to the Reynolds number.

7.3.3 The Transient Phase Change Process with Constant Wall Temperature

In this section, the focus is on the time-dependent characteristics of the phase-change process and Case 2 is used for the evaluation. Figure 7-18 is the temperature gradient history at the liquid-gas interface along the marker points for Case 2.

In Figure 7-18, it shows that the temperature gradients near the entrance do not change as time increases because it is controlled by the inlet boundary conditions. The peaks of temperature gradients are decreasing because the gas is chilled down by the liquid phase. The temperature gradients all drop drastically at the front of liquid core because that the distance between the solid wall and liquid surface becomes very large there. At the beginning, there is only one peak in the temperature gradient curve. Because of the deformation of the liquid-gas interface due to the surface tension as shown in Figure 7-14, small oscillations develop near the frontal area of the liquid core.

Figure 7-19 plots the history of mass flow rate at the exit for Case 2. It shows that the mass flow rate increases as time increases due to continuous evaporation from the liquid slug. The

curve is relatively linear; therefore the rate of evaporation is increasing almost linearly during that period.

Figure 7-20 gives the Nusselt number distributions for the three cases along the surface of solid wall at time=1.5. From Figure 7-13, it shows that the temperature contours of the three cases are very similar and therefore, the Nusselt numbers are also very close. They will be affected by the distance between the wall and the liquid surface. As discussed previously, the distance for Case 3 is shorter than others so that the Nusselt number for Case 3 will be larger than others. In Figure 7-20, it does show this trend. After the initial drop, the Nusselt number increases in the axial direction due to the increase of velocity from vaporization. Also, downstream of the front of liquid core ($X > 2.0$), the gas phase will adjust quickly to become a fully developed single phase flow and the Nusselt number in this region reflects that process. Far away from the inlet, the effects of the liquid slug is diminished and the Nusselt number is asymptotically approaching the fully developed single phase heat transfer value. For the purpose of evaluating the heat transfer enhancement due to evaporation, the Nusselt number is plotted by a long-dash line for an identical case except that there is only convection with no phase-change. The enhancement due to phase change is on the average 60%.

7.3.4 The Comparison of Nusselt Number with Phase Change Process and Constant Wall Temperature

In this section, the Nusselt number in liquid nitrogen with phase change and constant wall temperature is compared. In Hammouda et al.'s paper(1997), they gave the correlation for inverted annular flow as following:

$$Nu = 5.071 / Pr_v^{0.0439} + 0.0028 Pr_v^{0.645} Re_v \quad (7-3)$$

where Pr_v and Re_v are the Prandtl and Reynolds numbers for gas phase. In their research, the physical model is similar with the current research but there is still some difference in numerical procedures.

In current research, it is a direct numerical simulation, to solve the governing equations, boundary conditions and interfacial conditions directly without any empiricism. In Hammouda et al.'s research, they used two-fluid model. Their model is a semi-analytic model and using empirical correlations for transport coefficients. Also, their model is one dimensional in streamwise direction and assumes the computation is steady state, fully developed condition without the entrance effect so that they can not provide dynamic information. Figure 7-21 is the comparison of Nusselt number by the current method and Hammouda et al.'s correlation. In Figure 7-21, the upper long dash line is computed by Hammouda et al.'s correlation and the short dash line is by current SIMCC code. Near the inlet, because of the entrance effect, the thermal boundary layer will be thicker so that the Nusselt number obtained by SIMCC is smaller. In Hammouda et al.'s research, their model can only work in fully developed region so there is no entrance effect in their research and the Nusselt number computed by their correlation should higher than current method. The thermal boundary thickness should become thinner as X increases because of the stronger convection effect due to vaporization in two-phase zone. After the front of liquid core, the flow pattern is single-phase flow and the Nusselt number will decrease very fast and converge to the Nusselt number in single-phase zone. The correlation from Hammouda et al. can work in two-phase zone but the single-phase zone. By this comparison, it helps to validate the current computation for Nusselt number. At least, the computation of Nusselt number in this research is in a reasonable order.

7.4 Wall Chillover Process by Liquid Nitrogen

In this section, the selected fluid is also the liquid and vapor nitrogen at 77K and 300K under 1 ATM. The time step in this computation is set as 0.001.

The dimensionless parameters of Case 2 in the previous section are adopted in this section for the chillover study. For the chillover case, the wall is no longer kept at a constant temperature, whereas it is given a finite thickness and its temperature is decreasing as a result of heat loss to the cooling fluid. Therefore, computational grid system will include the wall. There will be three different thicknesses of the solid wall in this section and they are $\Delta R = R_{wo} - R_{wi} = 0.02R$ (Case 1), $0.04R$ (Case 2), $0.08R$ (Case 3).

7.4.1 Flow Patterns during Chillover Process

Figure 7-22 includes the contours of two velocity components U and V and the temperature contour of Case 1 at time=1.5.

When comparing with the Case 2 of the constant wall temperature condition in the previous section, the flow pattern is very similar with only small differences in the magnitude. Table 7-2 provides the maximum velocity in the two-phase region for the three wall chillover cases at time=1.5. The constant wall temperature case is also listed for comparison. Case 1 has the lowest maximum velocity because its thermal capacity is smaller than the other two which results in less amount of vaporization.

Figure 7-23 is the wall temperature contours of three cases at time=1.5. The results show that as expected, the thinner wall is chilled down faster than the thicker one.

7.4.2 The Wall and Liquid-Gas Interface Conditions during Chillover Process

This section focuses on the impact from the chillover process on the mass transfer at the interface. The generated mass flow rate at the interface is determined by the temperature gradient and the dimensionless parameters, Jakob and Peclet numbers.

Figure 7-24 is the wall temperature distribution at the solid-gas interface for the three cases at time=1.5. It shows that the wall for Case 3 is chilled down faster than others because the thickness of the wall of Case 3 is much thinner than others. Since this is an unsteady computation so that the lower temperature should be located at the entrance. Far away from the entrance, the temperature will converge to the initial temperature of 1.0

By the temperature contour given in Figure 7-23 and the temperature distributions at the solid-gas interface provided in Figure 7-24, it can be expected that the temperature gradients may be smaller near the entrance. Figure 7-25 shows the gas-side temperature gradients of the three cases along the liquid-gas interface at time=1.5.

In Figure 7-25, the temperature gradient at liquid-gas interface of Case 1 is smaller than others. The temperature gradient of Case 3 is larger than others and it is very close to the reference case of the constant temperature wall condition, since the thicker the wall is, the more the energy is stored. Accordingly, the solid-gas interface temperature would decrease more slowly; therefore, the temperature gradient at the liquid slug surface will be larger.

In this section, the dimensionless parameters for all cases are the same so that the mass flow rate at outlet should be determined by the heat flux at the interface. Table 7-3 shows the mass flow rates for the three and reference cases at time=1.5 at the outlet of pipe and the results agree with the temperature gradient plotted in Figure 7-25 where Case 3 has the largest temperature gradient and correspondingly the most evaporation rate which gives rise to the highest mass flow rate at the exit. By Table 7-3, it also shows that the mass flow rate at the exit approaches to that of the case with constant wall temperature as the thickness of the wall increases.

7.4.3 The Time-Dependent Development during Chilloidown Process

In this section, the time-dependent system behavior during the chilloidown process is presented. Figure 7-26 displays the temperature profiles along the inside surface at three different time steps for Case 1. The cooling of the wall is enhanced by the evaporation from the cold liquid slug and the effect due to the motion of the liquid slug is also shown by the wall surface temperature history.

Figure 7-27 is the temperature gradients of Case 1 along the solid-gas interface at different time steps. To compare with the constant wall temperature case in previous section, it shows that the temperature gradient decays faster for the chilloidown case.

Since the heat flux at the liquid-gas interface is different for the various chilloidown cases, it is clear that the mass flow rates will not be the same at the exit. Figure 7-28 is the history of mass flow rates for the three chilloidown cases and the constant wall temperature case.

At the beginning, the mass flow rates of all cases are very similar because the wall temperature/heat flux at this moment is governed by the same initial condition and the chilloidown process at the wall has just started. Once the time increases, the wall is chilled down continuously so that the difference in mass flow rates will increase. For the cases with a thicker wall, the temperature of the wall decreases slower so that the mass flow rate of the case with a thicker wall is close to the case with a constant wall temperature.

7.5 Wall Chilloidown Process by Liquid Hydrogen

In this section, the liquid hydrogen is investigated as it has been used extensively in space applications. The selected fluids are liquid and gas hydrogen at 20.27K and 200K under 1 ATM. The ratios of fluid properties the hydrogen are:

$$\frac{\rho_l}{\rho_g} = 576.94; \frac{\mu_l}{\mu_g} = 1.94; \frac{k_l}{k_g} = 0.92; \frac{Cp_l}{Cp_g} = 0.714$$

For comparison purposes, the liquid and gas nitrogen case is used as a reference to measure the differences in phase-change heat transfer when hydrogen is used. The nitrogen properties are taken for 77.36K and 300K under 1 ATM for liquid and gas phases, respectively. The ratios of fluid properties for the nitrogen are:

$$\frac{\rho_l}{\rho_g} = 706.91; \quad \frac{\mu_l}{\mu_g} = 8.85; \quad \frac{k_l}{k_g} = 5.41; \quad \frac{Cp_l}{Cp_g} = 1.97$$

The initial conditions, initial location of interface and boundary conditions are the same as those in the pervious chilldown case section. By the same geometry and boundary conditions, the four dimensionless parameters for hydrogen and nitrogen are:

$$\text{Hydrogen: } Re = 2145; \quad Pr = 1.08; \quad Ja = 4.27; \quad We = 1.71$$

$$\text{Nitrogen : } Re = 2043; \quad Pr = 2.32; \quad Ja = 0.42; \quad We = 3.69$$

By these two sets of dimensionless parameters, they show that the Reynolds, Weber and Prandtl numbers are close between hydrogen and nitrogen but the Jakob numbers are quite different. The ratio of Jakob numbers for both fluids is about ten times. The thickness of the wall in this section is $\Delta R = R_{wo} - R_{wi} = 0.02R$.

In the following, the results of hydrogen will be given side by side with corresponding ones from nitrogen for a direct comparison between these two cases.

Figure 7-29 provides a direct comparison for the U-velocity contours of hydrogen and nitrogen at time=0.4. In general, the two cases have very similar U-velocity profiles. The maximum U-velocities for the two cases are also located almost at the same location near the exit of the annular channel. But, the magnitudes are totally different and the maximum U-velocity for hydrogen is about four times of that for nitrogen that is exclusively due to the much higher evaporation rate of hydrogen resulting from a much larger Jakob number as explained next. From previous discussion, the mass transfer rate can be estimated by

$$\dot{m}'' \propto \frac{Ja}{Pe} (\overline{\nabla T}_v) \quad (7-4)$$

The ratio (Ja / Pe) of hydrogen to nitrogen is 20.8 that is the main cause for the maximum U-velocity difference.

Figure 7-30 is the V-velocity contours of two cases at time=0.4 and they show the same trend as that of the U-velocity contours. The contours are similar but the magnitudes are quite different. First, the vaporization rate on the liquid slug surface is much uniform for the hydrogen case. The relatively non-uniform evaporation rate from the nitrogen liquid slug surface is due to the shape deformation whereas the hydrogen surface is very flat. Second, based on Figures 7-29 and 7-30, they show that the convection effect for the hydrogen case is much stronger so that the location of second highest V-velocity is much close to the liquid-gas interface for nitrogen case.

Figure 7-31 is the temperature contour comparison for the two cases at time=0.4. It shows large differences between the two cases. Since the convective effect in hydrogen is much stronger due to higher evaporation rates than that in the nitrogen case. It can be expected that the temperature profile in the hydrogen case should reflect that. Due to the strong convection, the temperatures at downstream in the hydrogen case is cooler than those in the nitrogen case.

Figure 7-32 shows the temperature distributions at the solid-gas interface for both cases during chilldown process. Due to the stronger convection effects, the solid wall for the hydrogen case is cooled down much faster than that in the nitrogen case, especially near the entrance region. In the downstream region, the temperature of both cases will be close to the initial wall temperature since there is only very few heat transfer in that region.

Figure 7-33 compares the Nusselt number distributions on the inner surface of pipe wall for the two cases. Both cases show very similar entrance region behaviors near the inlet. Similarly, because of the stronger convection effects, the thermal boundary in the hydrogen case

will be thinner than that in the nitrogen case as shown in Figure 7-31 and this means that the Nusselt number in the hydrogen case should be larger. On the average, the heat transfer coefficient on the pipe wall is 25% higher in the hydrogen case.

7.6 Summary

In summary, three working fluids with two different wall conditions were investigated in this chapter. Because of the evaporation phase change that takes place on the liquid slug surface, mass fluxes are generated from the liquid-gas interface that acts as a source of mass input to the gas stream. In fluid dynamics, this generated gas does change the flow structure substantially. Because of the generated gas, the total mass flow rate of the gas phase can not be a constant at any downstream location in the two-phase region. Also, there is always a very strong jet effect near the intersection between the single- and two- phase zones, where the maximum gas stream velocity is located. Therefore, the flow patterns with phase change are different from those without phase change.

Because of the evaporation that causes a large increase in the gas stream velocity in the two-phase region, a much stronger convective effect is therefore induced. This enhanced convection results in a substantial increase in the heat transfer efficiency of entire system. This enhanced convection effect can also be seen in the chilldown process where the wall temperature decreases faster in the case with a stronger convective effect.

The wall chilldown case is a highly transient process as the heat transfer that supplies the latent heat for evaporation decreases with time due to decreasing heat transfer driving force, the temperature gradient between the pipe wall and the liquid slug.

In the last case, a close comparison was made between liquid hydrogen and liquid nitrogen as cryogenic working fluids. In general, under similar conditions, liquid hydrogen offers a much

higher evaporation rate that induces more intensive convection effects. The Nusselt number is approximately 25% higher for the liquid hydrogen case.

Table 7-1. Dimensionless parameters for the nitrogen case with constant wall temperature.

Dimensionless Parameters	Re	Pe	Ja	We
Case 1	2000	4640	0.42	3.69
Case 2	1500	3480	0.42	2.76
Case 3	1000	2320	0.42	1.84

Table 7-2. The maximum velocity for the nitrogen case with wall chilldown and the reference cases at time=1.5.

Constant Temperature		Wall Chilldown Cases		
		Case 1	Case 2	Case 3
Max Velocity	13.62	12.90	13.31	13.41

Table 7-3. The mass flow rate for the nitrogen case with wall chilldown and the reference cases at time=1.5.

Constant Temperature		Wall Chilldown Cases		
		Case 1	Case 2	Case 3
Max Flow Rate	0.594	0.571	0.585	0.591

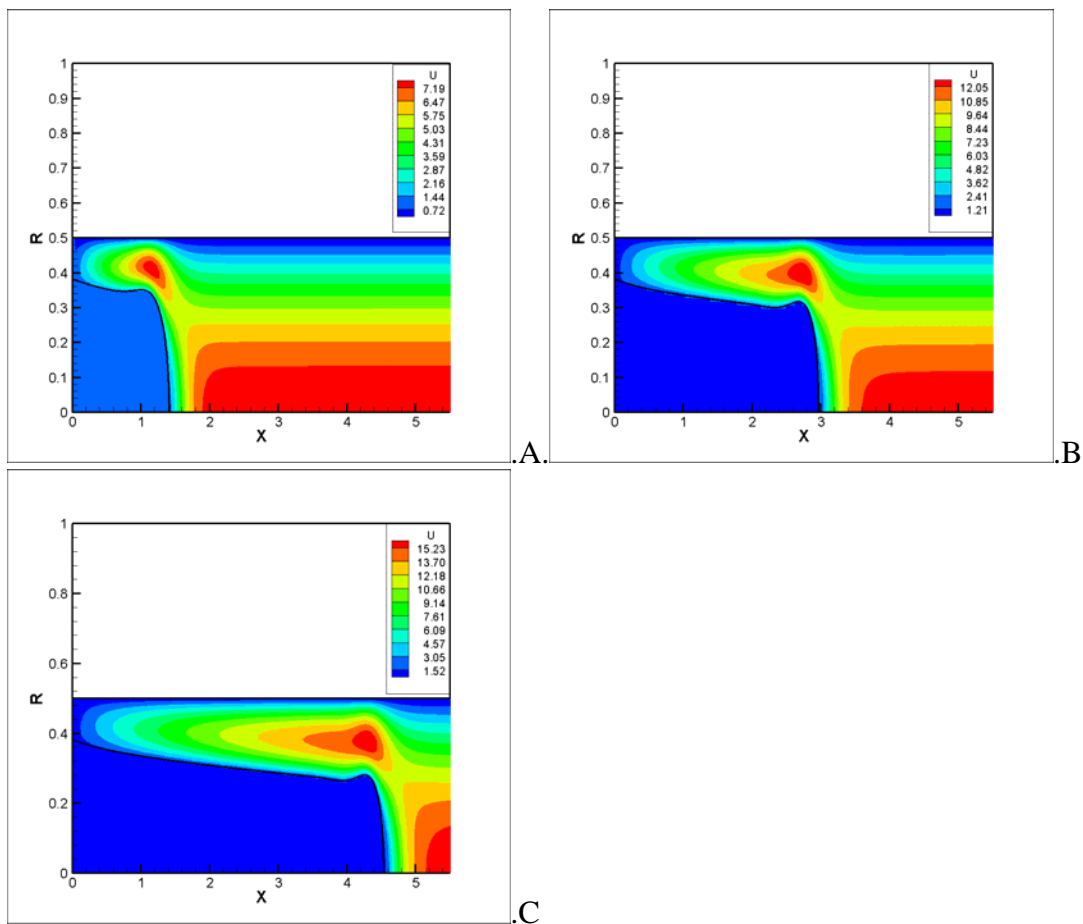


Figure 7-1. The U contours for the refrigerant R-508B case at different time steps. A) time=1.0, B) time=2.5, C) time=4.0.

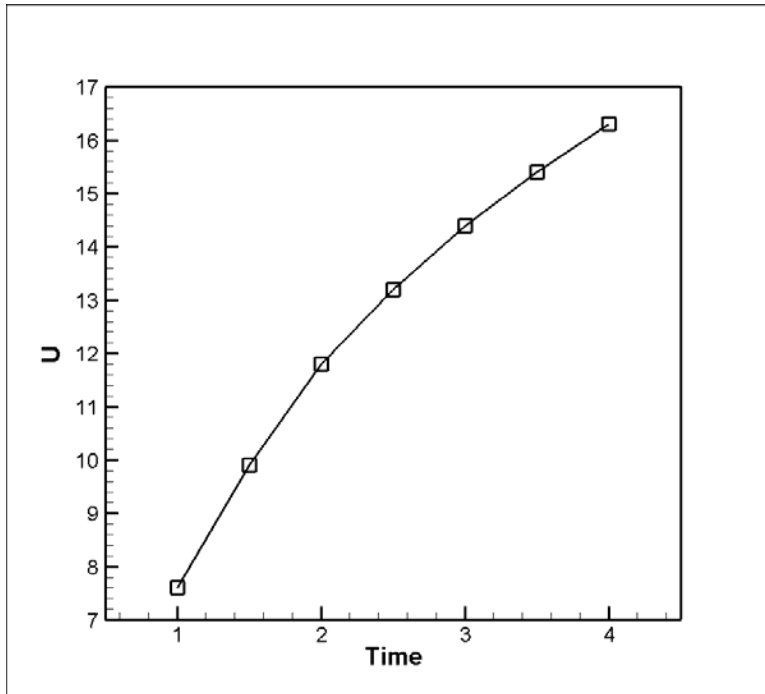


Figure 7-2. The local maximum U in the gas phase for the refrigerant R-508B case at different time steps.

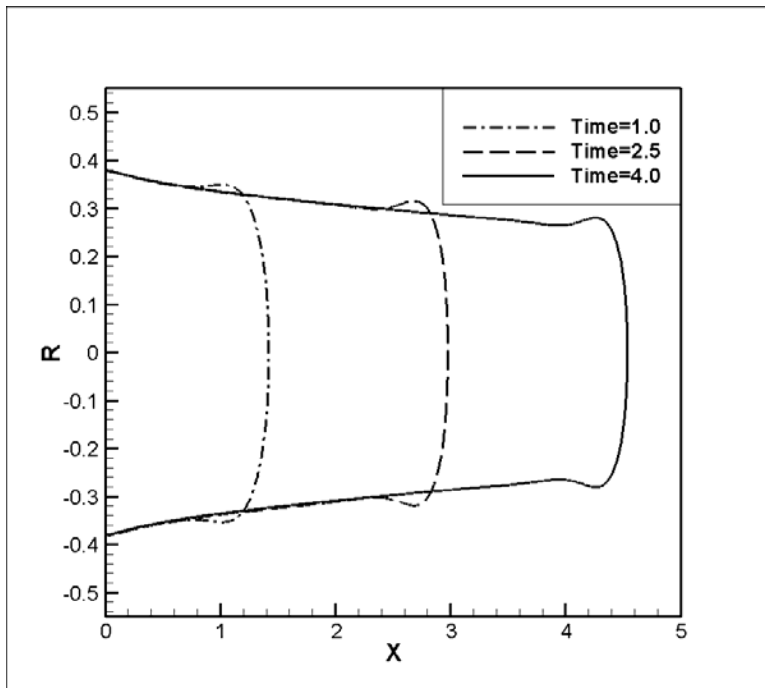


Figure 7-3. The interfaces for the refrigerant R-508B case at different time steps.

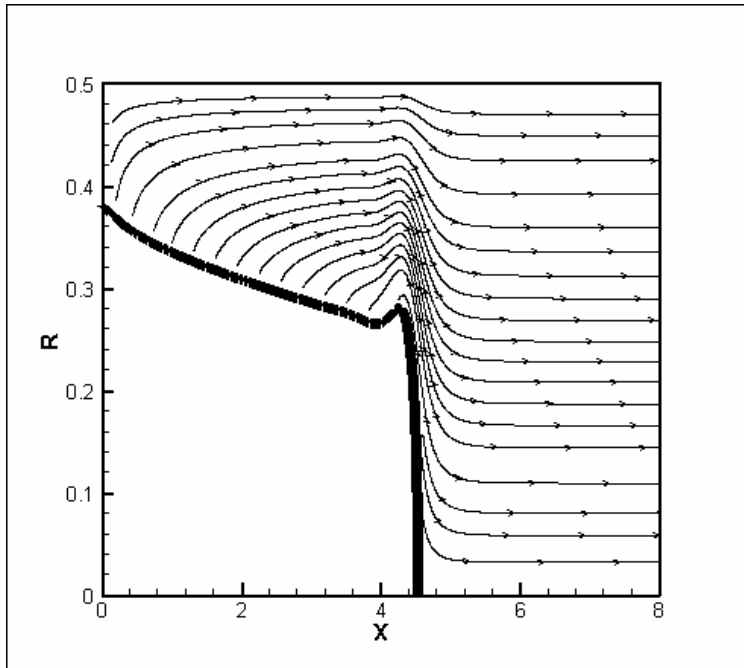


Figure 7-4. The streamlines in the gas phase for the refrigerant R-508B case at time=4.0

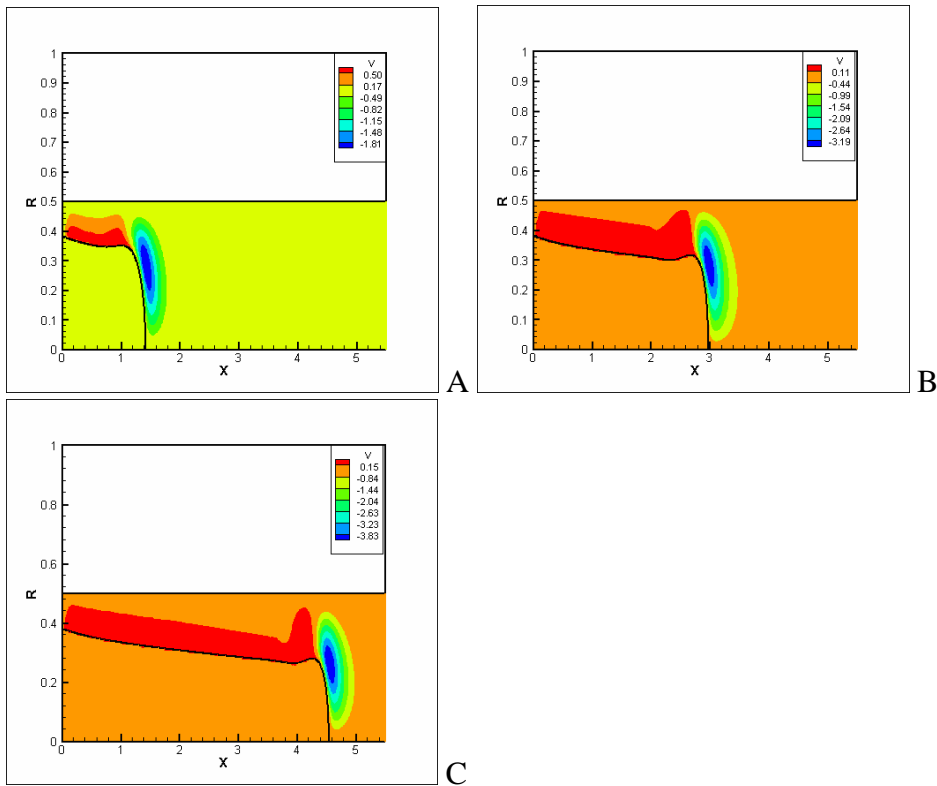


Figure 7-5. The V contours for refrigerant R-508B case at different time steps. A) time=1.0, B) time=2.5, C) time=4.0.

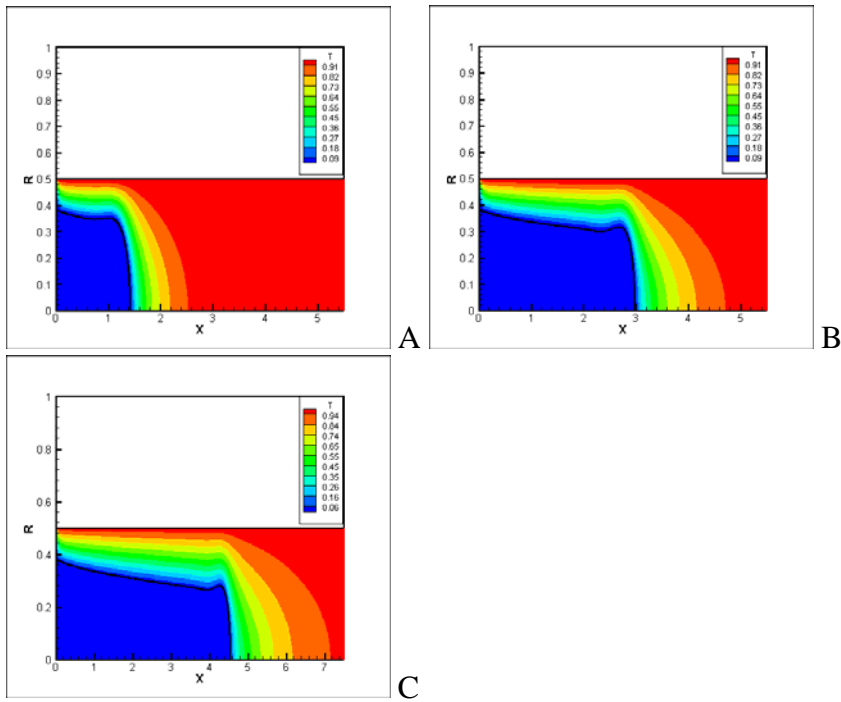


Figure 7-6. The temperature contours for refrigerant R-508B case at different time steps. A) time=1.0, B) time=2.5, C) time=4.0.

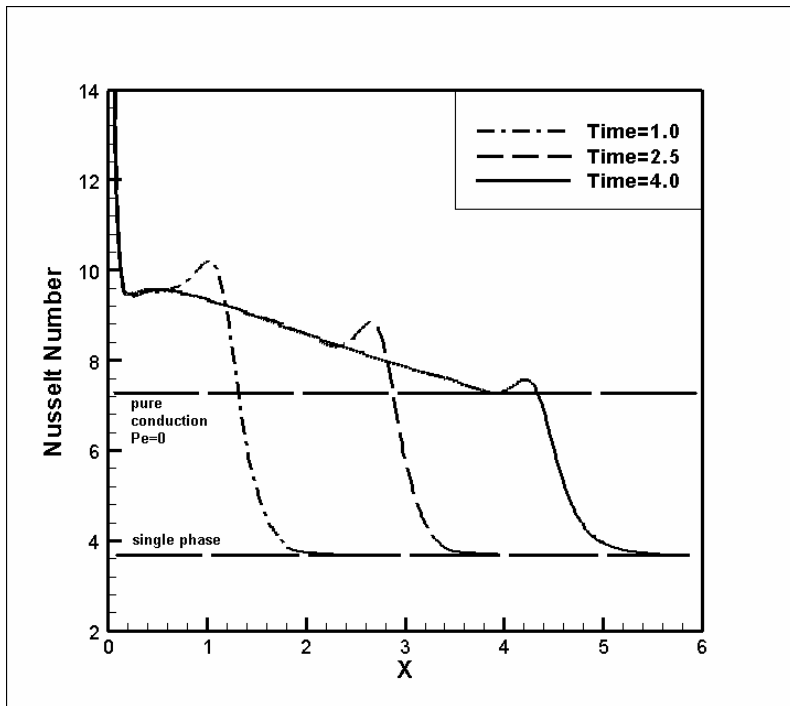


Figure 7-7. The Nusselt numbers along solid wall for the refrigerant R-508B case at different time steps.

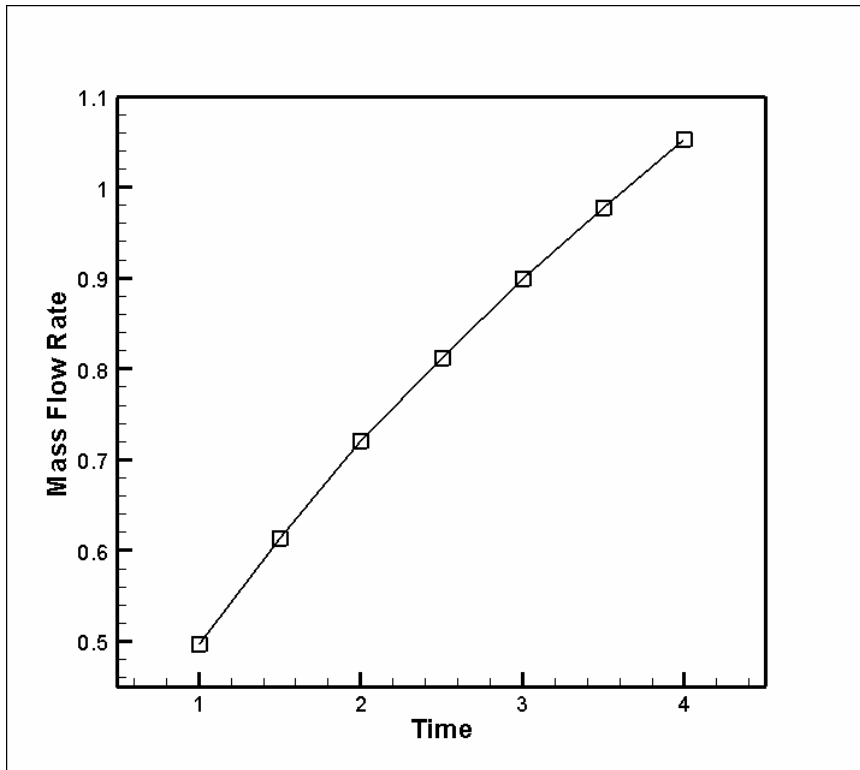


Figure 7-8. The total mass flow rate of gas phase for the refrigerant R-508B case at different time steps.

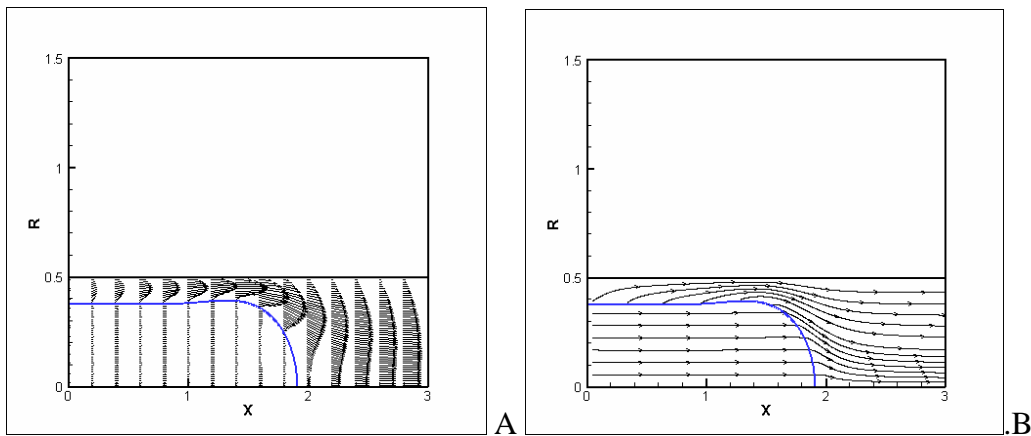


Figure 7-9. The vector and the streamline plots for Case 2 in the nitrogen case with constant wall temperature at time=1.5. A) vector plot and B) streamline plot.

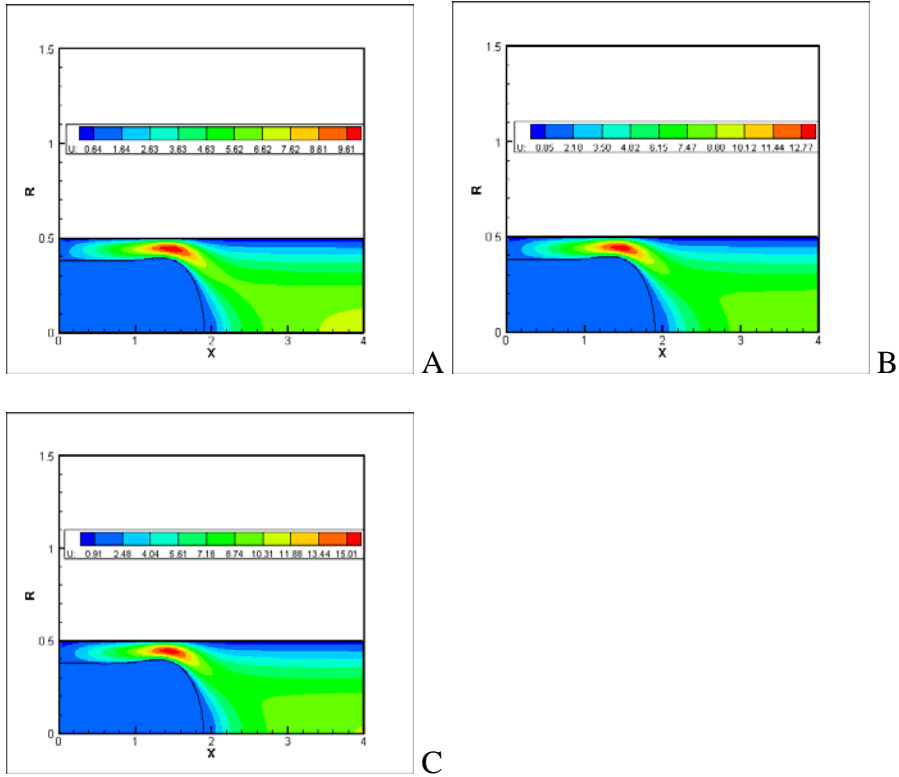


Figure 7-10. The U contours for the nitrogen case with constant wall temperature at time=1.5.
 A) Case 1, B) Case 2, C) Case 3.

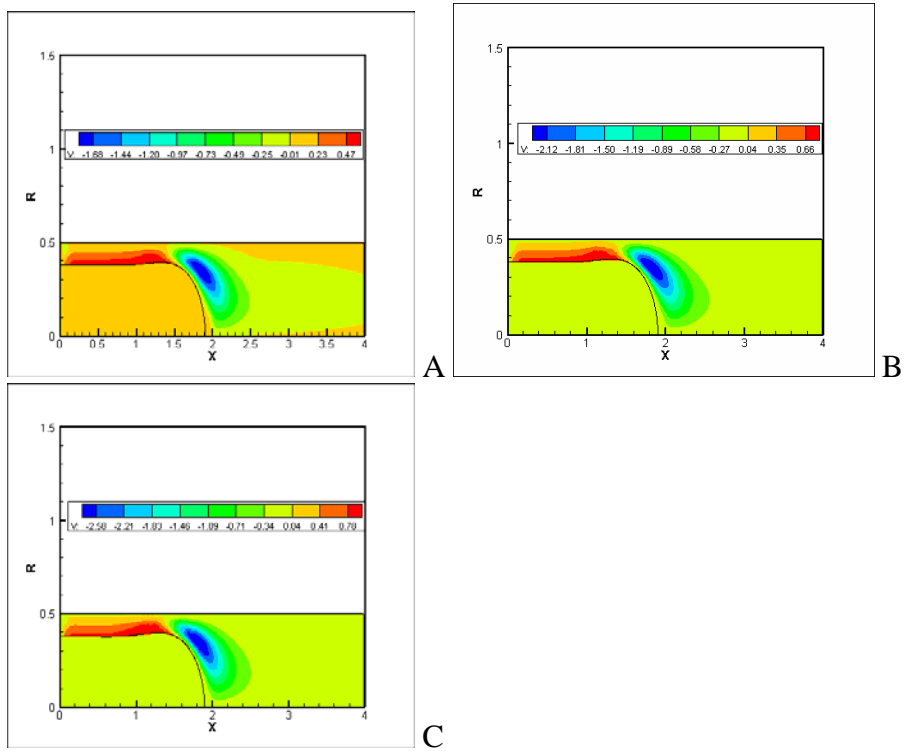


Figure 7-11. The V contours for nitrogen case with constant wall temperature at time=1.5. A) Case 1, B) Case 2, C) Case 3.

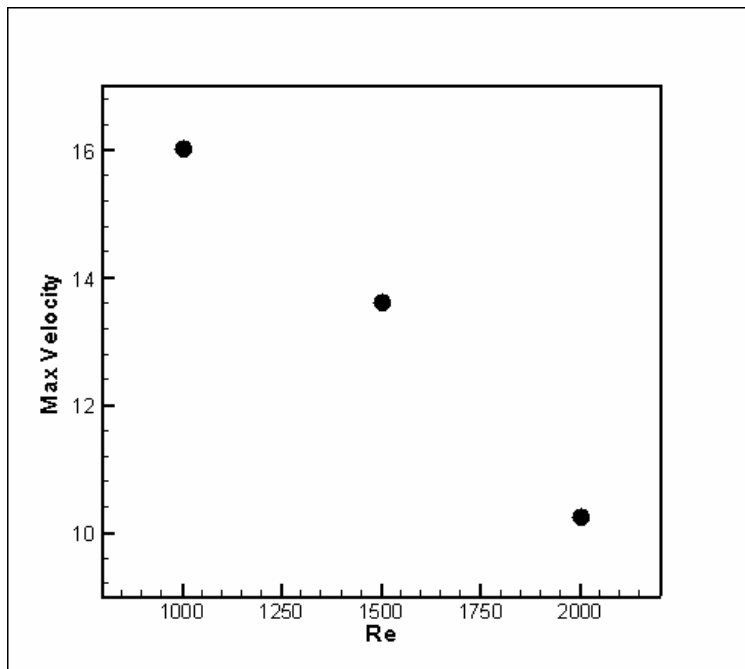


Figure 7-12. Maximum velocity for the nitrogen case with constant wall temperature of three cases.

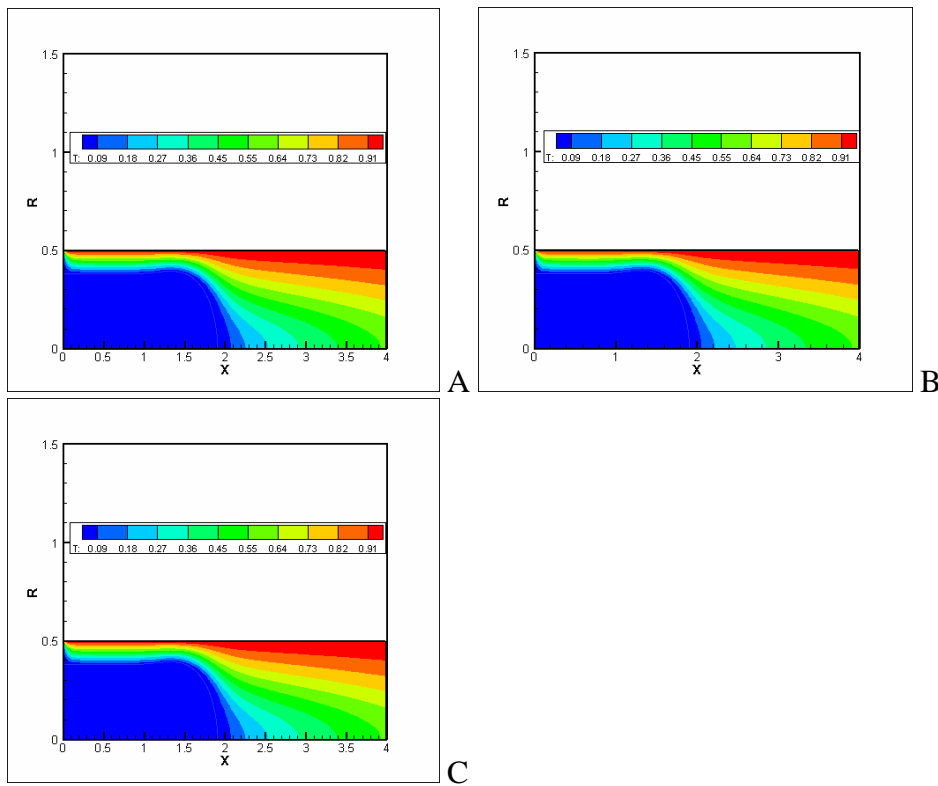


Figure 7-13. The temperature contours for nitrogen case with constant wall temperature at time=1.5. A) Case 1, B) Case 2, C) Case 3.

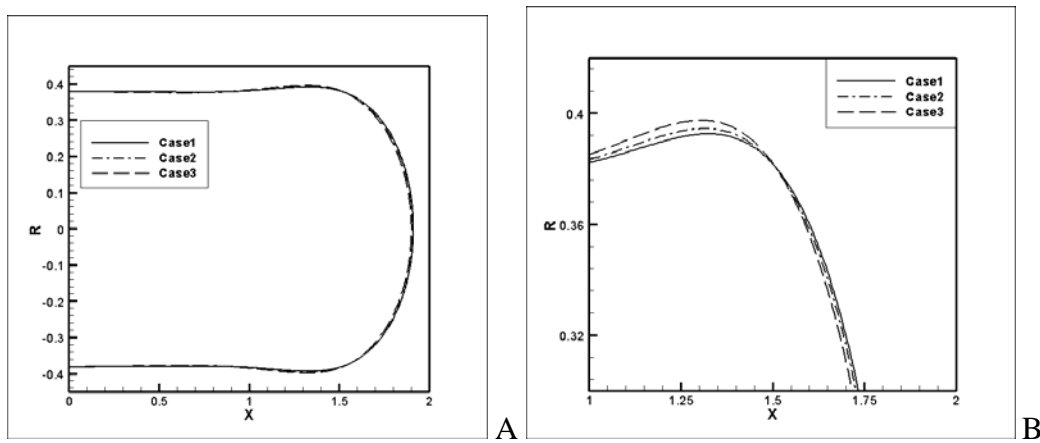


Figure 7-14. The interfaces of three cases for the nitrogen case with constant wall temperature at time=1.5. A) entire, B) local.

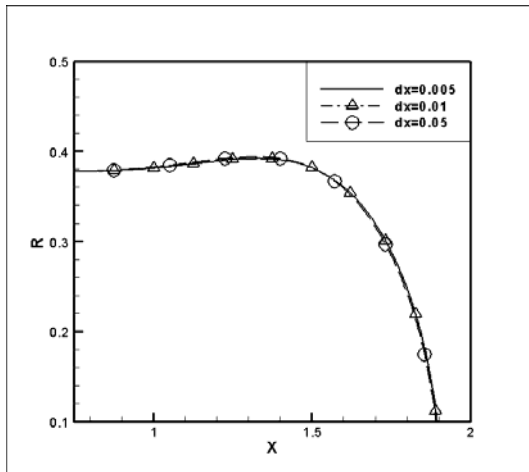


Figure 7-15. The interfaces of three different grid lengths.

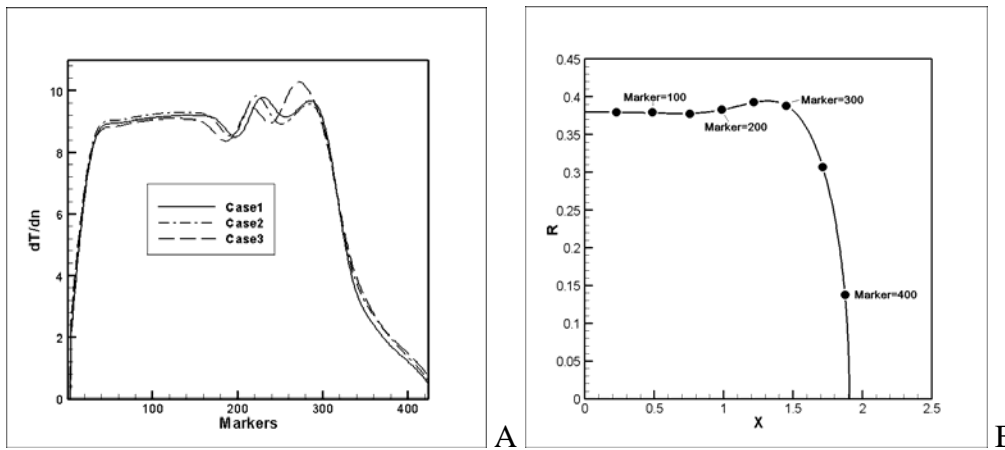


Figure 7-16. The temperature gradient of three cases along the interface at time=1.5 and the locations of markers for the nitrogen case with constant wall temperature.

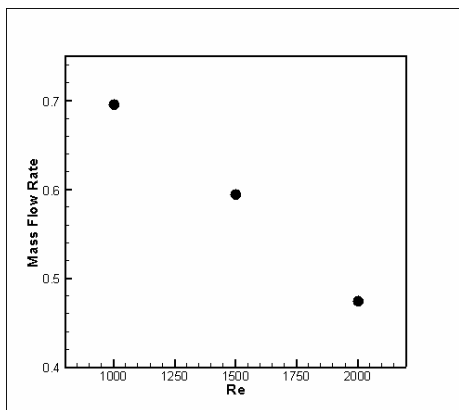


Figure 7-17. The mass flow rate for the nitrogen case with constant wall temperature at time=1.5.

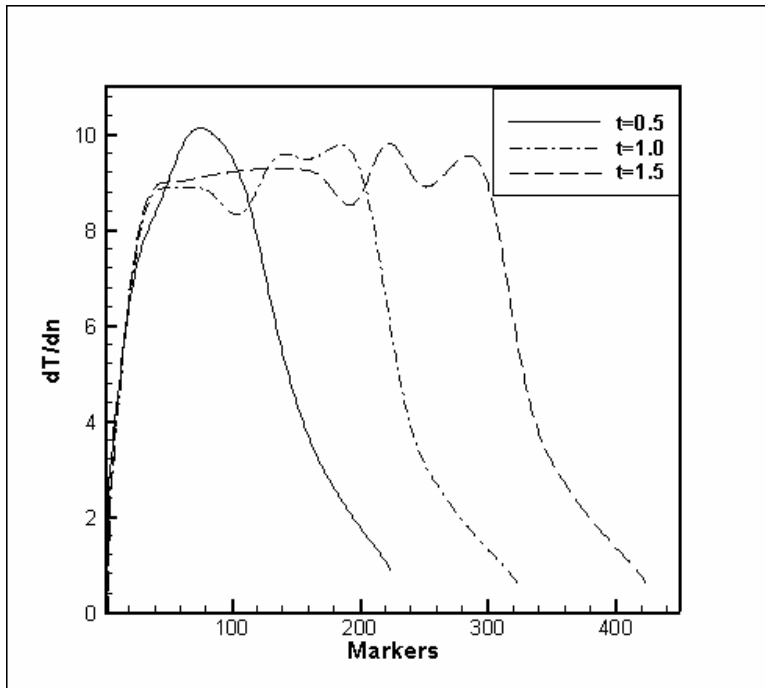


Figure 7-18. The history of temperature gradient along the interface of Case 2 in the nitrogen case with constant wall temperature.

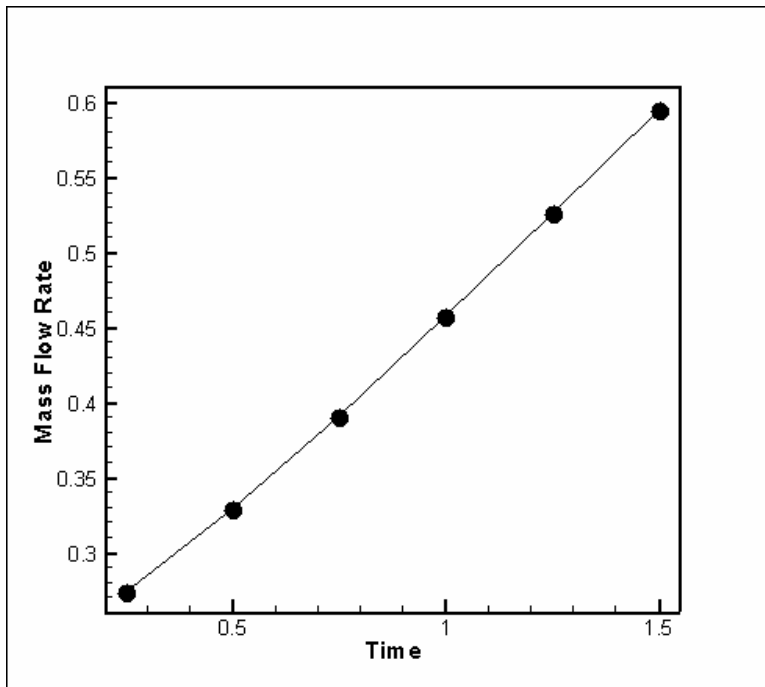


Figure 7-19. The history of mass flow rate of Case 2 for nitrogen case with constant wall temperature.

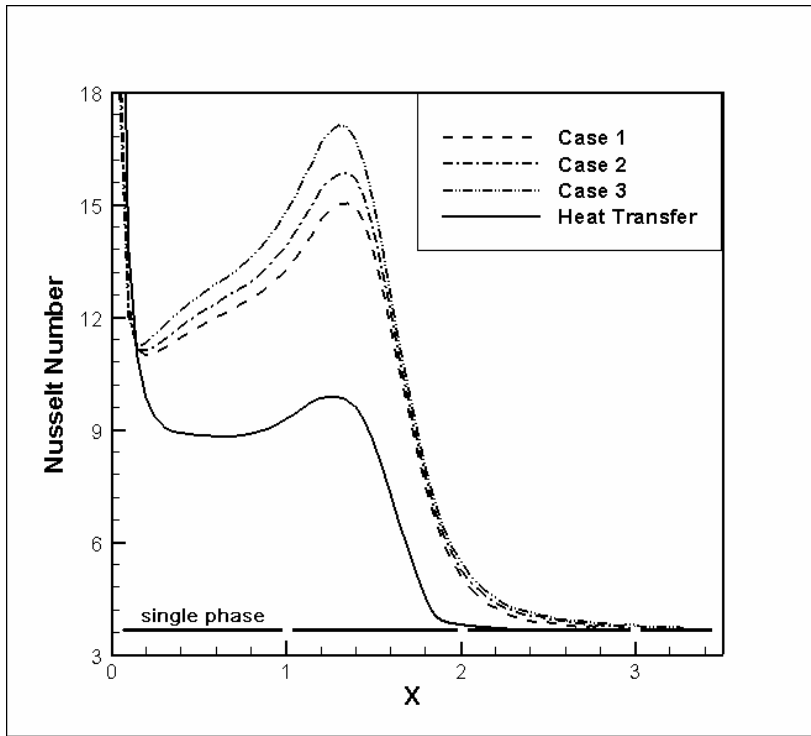


Figure 7-20. The Nusselt number at wall for the nitrogen case with constant wall temperature at time=1.5.

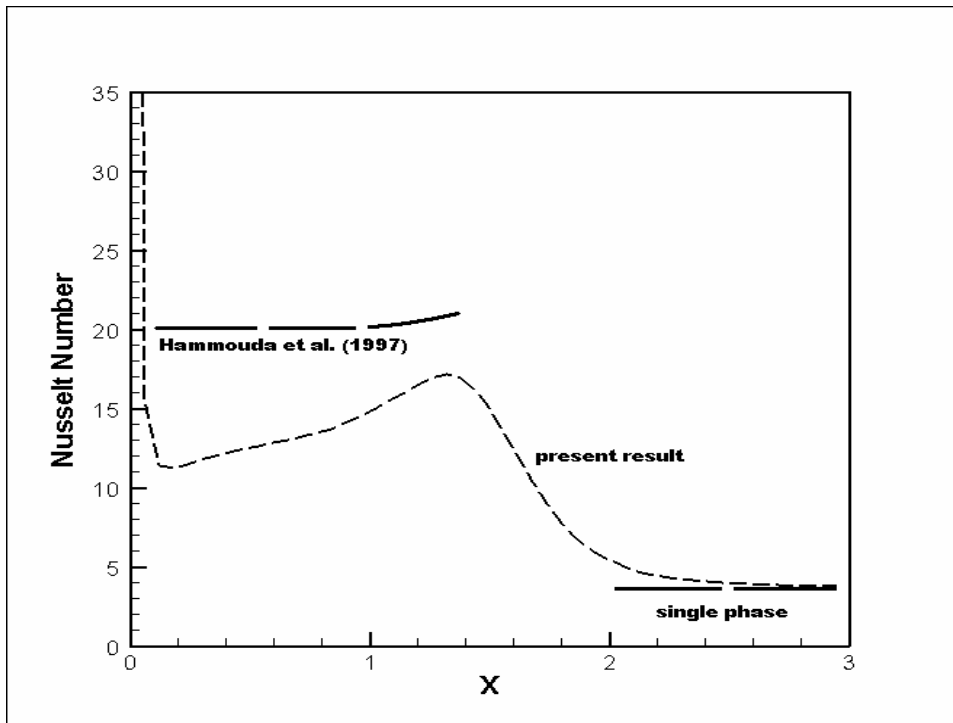


Figure 7-21. The comparison of Nusselt number by the current method and Hammouda et al.'s correlation.

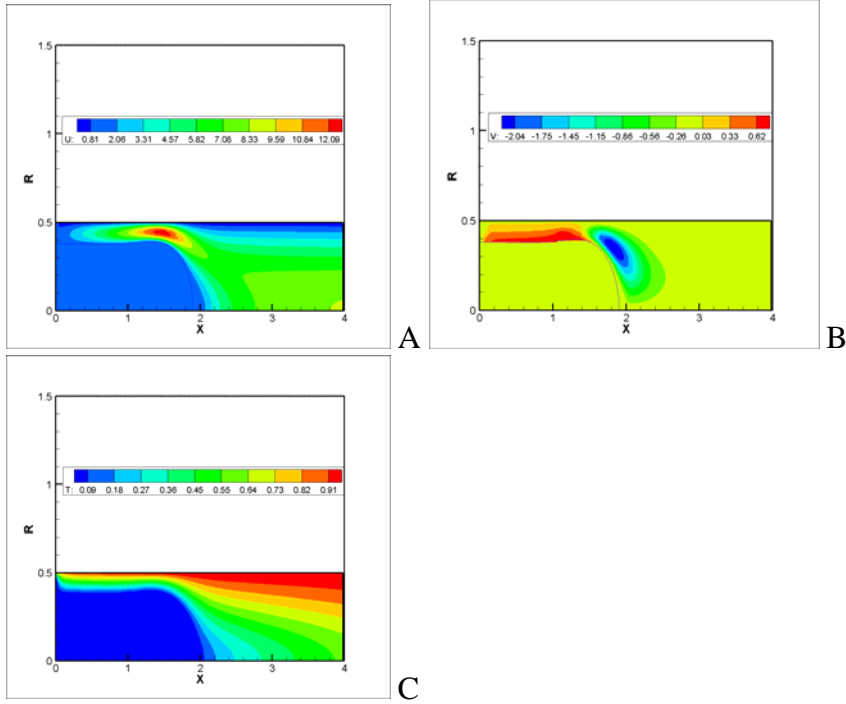


Figure 7-22. The U, V and temperature contours of Case 1 in the nitrogen case with wall chilldown at time=1.5. A) U contour, B) V contour, C) temperature contour.

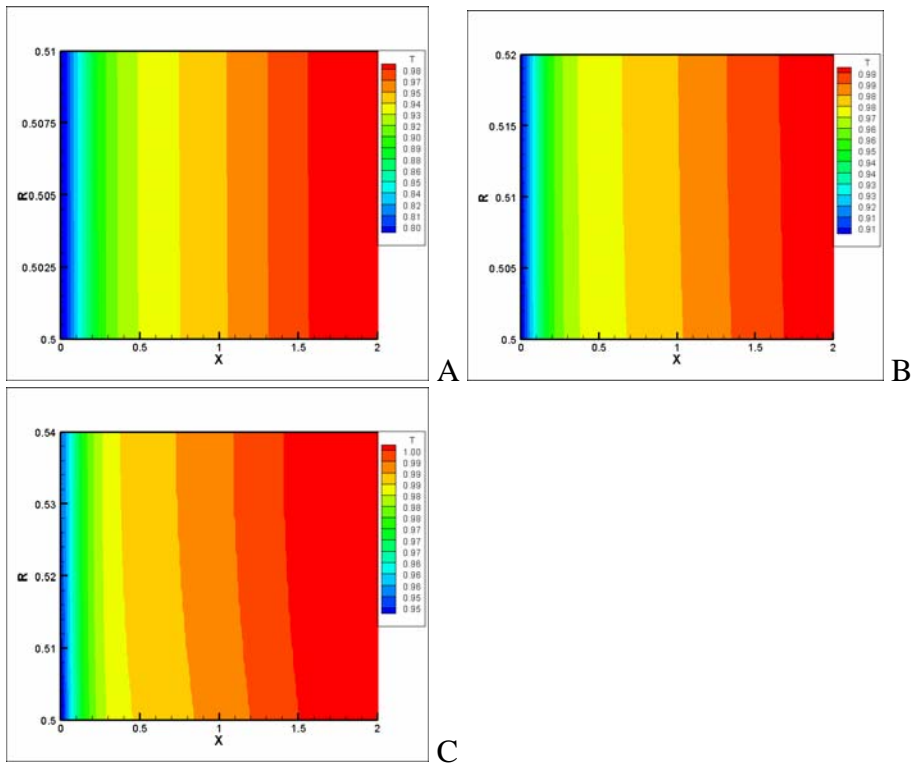


Figure 7-23. The wall temperature contours for the nitrogen case with wall chilldown at time=1.5. A) Case 1, B) Case 2, C) Case 3.

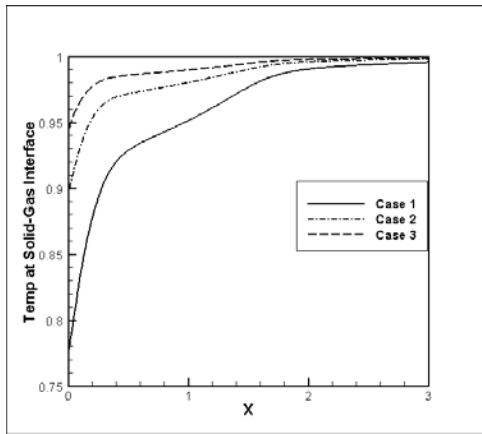


Figure 7-24. The temperature at solid-gas interface for the nitrogen case with wall chilldown at time=1.5

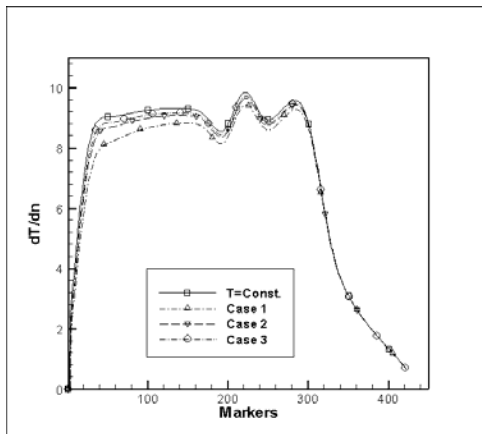


Figure 7-25. The temperature gradients along the interface of reference for the nitrogen case with wall chilldown at time=1.5

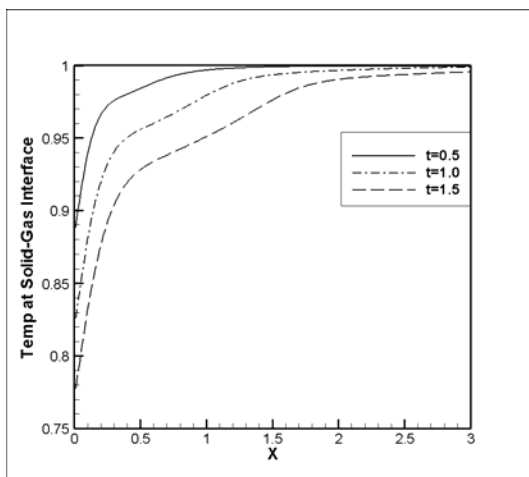


Figure 7-26. The temperature history of Case 1 in the nitrogen case with wall chilldown at time=1.5.

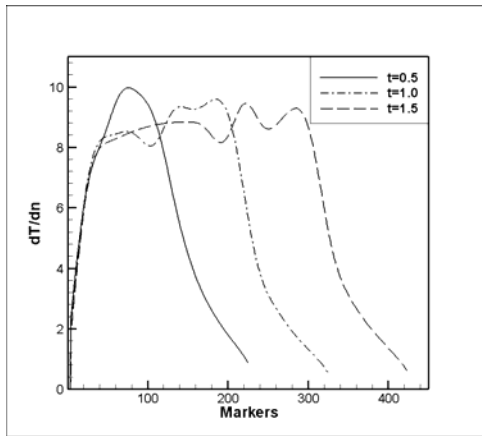


Figure 7-27. Temperature gradients along the interface of Case 1 in the nitrogen case with wall chilldown at time=1.5

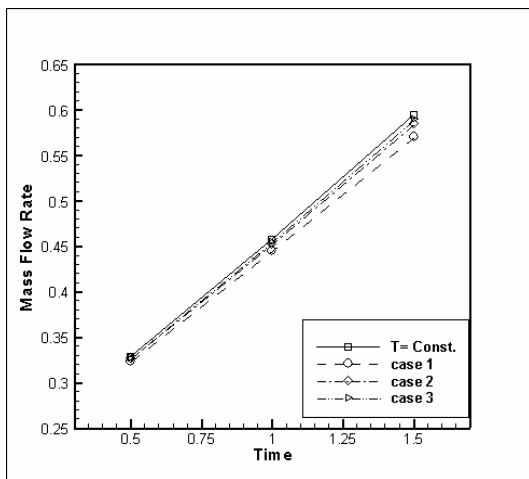


Figure 7-28. The mass flow rates for the nitrogen case with wall chilldown and reference case.

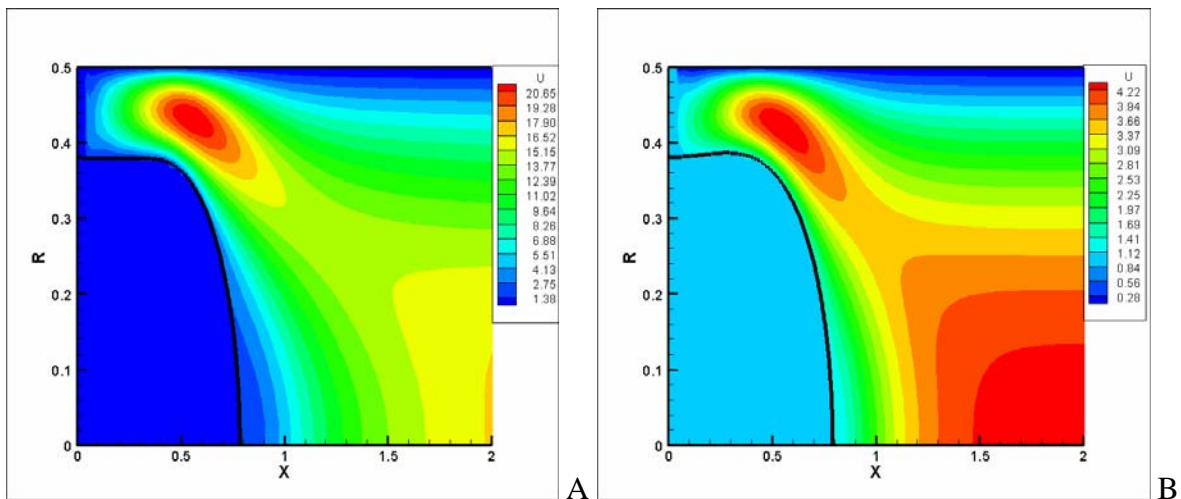


Figure 7-29. U contours of two cases at time=0.4. A) hydrogen, B) nitrogen.

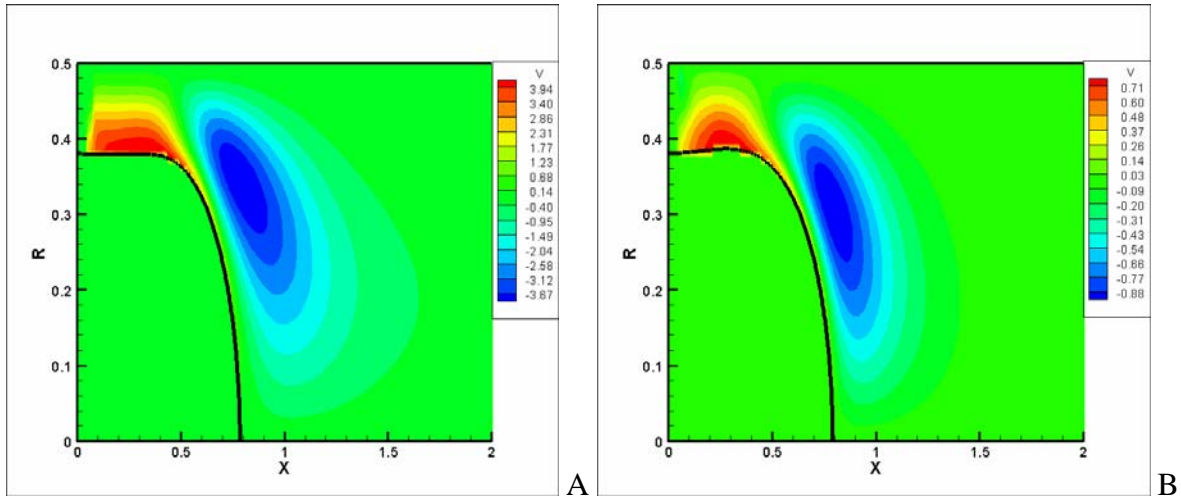


Figure 7-30. V contours of two cases at time=0.4. A) hydrogen, B) nitrogen.

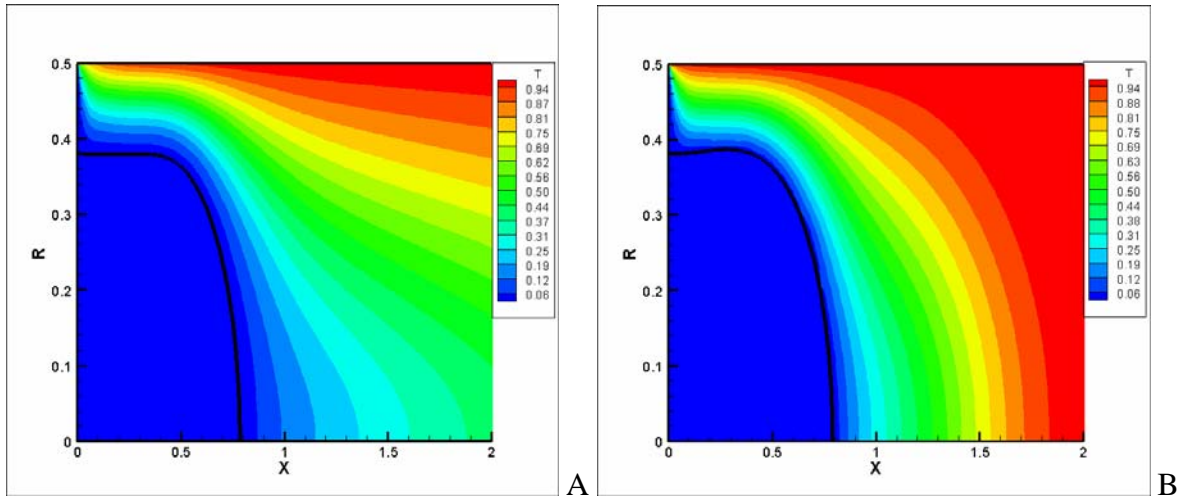


Figure 7-31. Temperature contours of two cases at time=0.4. A) hydrogen, B) nitrogen.

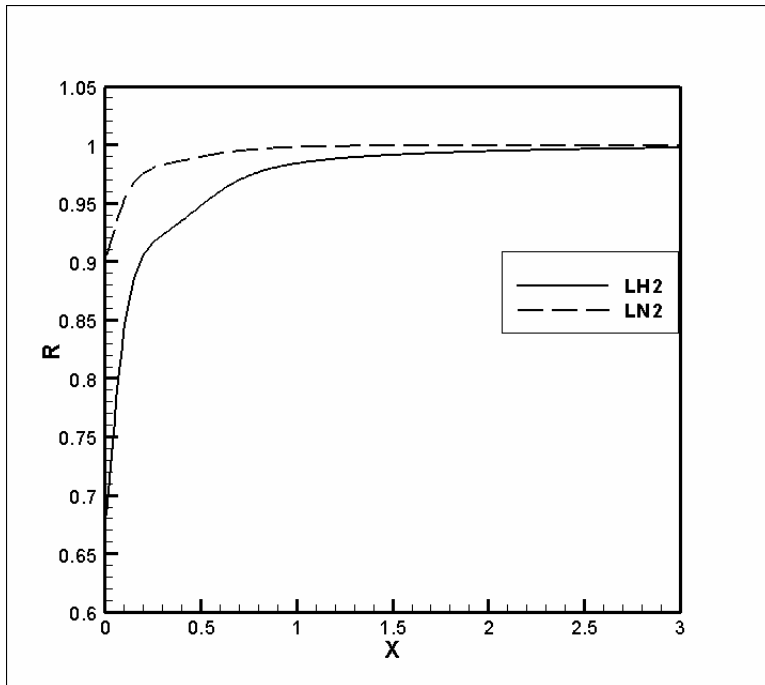


Figure 7-32. Temperature at solid-gas interface for the hydrogen and nitrogen cases at time=0.4.

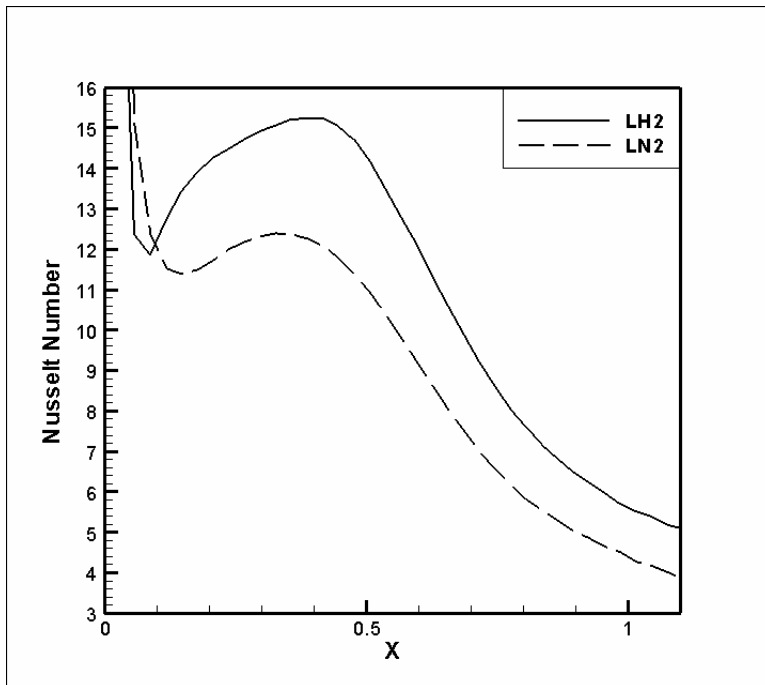


Figure 7-33. Nusselt number distributions on the pipe wall for the hydrogen and nitrogen cases for both cases at time=0.4.

CHAPTER 8 SUMMARY AND FUTURE WORK

8.1 Summary

In this research, a numerical package for handling phase change and chilldown for cryogenic two-phase flow has been developed. The major contributions are the phase change computation which includes the energy equation solver, the phase change algorithm for the liquid-gas interface, the conjugate heat transfer for solid and gas phase and the thermal radiation model.

In Chapters 1 and 2, literature review is done and the problem is defined. In Chapter 3, the governing equations, the boundary conditions and the interfacial conditions and their dimensionless forms are listed. In Chapter 4, the main numerical techniques applied in this research are introduced and explained.

All the main techniques are validated in Chapter 5 and the validation includes the solver of governing equations, the SIMCC with moving interfacial algorithm and the mass transfer computation.

Chapters 6 and 7 form the core of this research and four different cases are computed and discussed. In Chapter 6, it focuses on the cases without phase change and includes the isothermal and heat transfer two-phase flow in a pipe. In Chapter 7, the phase change is included with different condition: the constant wall temperature and the wall with finite thickness.

8.2 Future Work

In the current research, the preliminary techniques are ready for the cryogenic two-phase flow. Besides these techniques, there are still some interesting future possibilities for this research:

Three dimensional interfacial tracking technique and cut-cells: The current SIMCC code can only handle two dimensional axisymmetric computations. This limits the current research to axisymmetric flows. In recent researches, some scholars have introduced the three dimensional interfacial tracking technique and cut-cells (Cieslak et al. 2001, Singh et al. 2005). However, currently, the researches can only handle very simple geometries and this should be a good direction for the future work.

Turbulence model: The laminar flow is another limitation of the current code. The critical Reynolds number for laminar flow is about $Re = 2000 - 3000$ (White 1991). Once the Reynolds number becomes larger than 3000, the flow regime of pipe flow should be closer to turbulent flow and the turbulence model (Launder and Spalding 1974) is very important.

Compressibility and variable fluid properties: In current code, the two phases are treated as incompressible fluids. This should be safe since the temperature gradient in the temperature contour is not very strong. However, for a more general situation, the compressibility and variable fluid properties due to the large temperature difference should be considered. Recently, some researchers have extended the pressure-based solver from incompressible to compressible flow (Kamakoti 2004).

Adaptive grid or simple local grid refinement: In the current SIMCC code, the grid system is the Cartesian grid system. It can be stretched but still have to keep uniformity near the interface. This will cause the waste of time and memory. In order to solve this issue, the adaptive grid method (Uzgoren et al. 2007) or simple local grid refinement (Popescu et al. 2006) near the interface seems a good strategy.

LIST OF REFERENCES

- Adham-Khodaparast, K., Xu, J. J., and Kawaji, M. (1995). "Flow Film Boiling Collapse and Surface Rewetting in Normal and Reduced Gravity Conditions." *International Journal of Heat and Mass Transfer*, 38(15), 2749-2760.
- Al-Rawahi, N., and Tryggvason, G. (2004). "Numerical Simulation of Dendritic Solidification with Convection: Three-dimensional Flow." *Journal of Computational Physics*, 194(2), 677-696.
- Alexiades, V., and Solomon, A. D. (1993). "Mathematical Modeling of Melting and Freezing Processes." Washington, DC.
- Alipchenkov, V. M., Nigmatulin, R. I., Soloviev, S. L., Stonik, O. G., Zaichik, L. I., and Zeigarnik, Y. A. (2004). "A Three-fluid Model of Two-phase Dispersed-annular Flow." *International Journal of Heat and Mass Transfer*, 47(24), 5323-5338.
- Antar, B. N., and Collins, F. G. (1997). "Flow Boiling during Quenching in Low Gravity Environment." *International Journal of Microgravity Science and Technology*, 3, 118-128.
- Ardron, K. H. (1980). "One-dimensional Two-fluid Equations for Horizontal Stratified Two-phase Flow." *International Journal of Multiphase Flow*, 6(4), 295-304.
- Aritomi, M., Inoue, A., Aoki, S., and Hanawa, K. (1990). "Thermal-hydraulic Behavior of Inverted Annular Flow." *Nuclear Engineering and Design*, 120(2-3), 281-291.
- Badalassi, V. E., Cenicerros, H. D., and Banerjee, S. (2003). "Computation of Multiphase Systems with Phase Field Models." *Journal of Computational Physics*, 190(2), 371-397.
- Bashforth, F., and Adams, J. C. (1883). *Theories of Capillary Action*, Cambridge University Press, London.
- Bednar, H. H. (1986). *Pressure Vessel Design Handbook*, Van Nostrand Reinhold Company, New York.
- Bonacina, C., Comini, G., Fasano, A., and M. Primicerio. (1973). "Numerical Solution of Phase-change Problems." *International Journal of Heat Mass Transfer*, 16(10), 1825-1832.
- Bousman, W. S., McQuillen, J. B., and Witte, L. C. (1996). "Gas-liquid Flow Patterns in Microgravity: Effects of Tube Diameter, Liquid Viscosity and Surface Tension." *International Journal of Multiphase Flow*, 22(6), 1035-1053.
- Brackbill, J. U., Kothe, D. B., and Zemach, C. (1992). "A Continuum Method for Modeling Surface Tension." *Journal of Computational Physics*, 100(2), 335-354.

- Bronson, J. C., Edeskuty, F. J., Fretwell, J. H., Hammel, E. F., Keller, W. E., Meier, K. L., Schuch, A. F., and Willis, W. L. (1962). "Problems in Cool-down of Cryogenic Systems." *Advances in Cryogenic Engineering*, 7, 198-205.
- Burke, J. C., Byrnes, W. R., Post, A. H., and Ruccia, F. E. (1960). "Pressurized Cool-down of Cryogenic Transfer Lines." *Advances in Cryogenic Engineering*, 4, 378-394.
- Cancelli, C., Demichela, M., and Piccinini, N. (2005). "Accidental Release of Hydrogen from a Cryogenic Tank." *Cryogenics*, 45(7), 481-488.
- Carey, V. P. (1992). *Liquid-vapor Phase-change Phenomena*, Taylor & Francis, New York.
- Chapra, S. C., and Canale, R. P. (2002). *Numerical Methods for Engineers*, McGraw-Hill, New York.
- Chen, J. C. (1966). "Correlation for Boiling Heat Transfer to Saturated Fluids in Convective Flow." *Industry Engineering Chemistry Process Design and Development*, 5, 322-329.
- Chi, J. W. H. (1965). "Cooldown Temperatures and Cooldown Time During Mist Flow " *Advances in Cryogenic Engineering*, 10, 330-340.
- Chorin, A. J. (1968). "Numerical Solution of the Navier-Stokes Equations." *Mathematics of Computation*, 22(104), 745-762.
- Cieslak, S., Khelil, S. B., Choquet, I., and Merlen, A. (2001). "Cut Cell Strategy for 3-D Blast Waves Numerical Simulations." *Shock Waves*, 10, 421-429.
- Colin, C., Fabre, J. A., and Dukler, A. E. (1991). "Gas-liquid Flow at Microgravity Conditions I. Dispersed Bubble and Slug Flow." *International Journal of Multiphase Flow*, 17(4), 533-544.
- Crank, J., and Nicolson, P. (1947). "A Pratical Method for Numerical Evaluation of Solutions of Partial Differential Equations of the Heat Conduction Type." *Proceedings of the Cambridge Philosophical Society*, 43, 50-64.
- Cross, M. F., Majumdar, A. K., Bennett Jr., J. C., and Malla, R. B. (2002). "Model of Chill Down in Cryogenic Transfer Lines." *Journal of Spacecraft and Rockets*, 39(2), 284-289.
- Dandy, D. S., and Leal, L. G. (1989). "Buoyancy-driven Motion of a Deformable Drop through a Quiescent Liquid at Intermediate Reynolds Numbers." *Journal of Fluid Mechanics*, 208, 161-192.
- Dhir, V. K. (2001). "Numerical Simulations of Pool-boiling Heat Transfer." *AIChE Journal* 47(4), 813-834.
- Dukler, A. E., Fabre, J. A., McQuillen, J. B., and Vernon, R. (1988). "Gas Liquid Flow at Microgravity Conditions: Flow Patterns and their Transitions." *International Journal of Multiphase Flow*, 14(4), 389-400.

- Dziubinski, M., Fidos, H., and Sosno, M. (2004). "The Flow Pattern Map of a Two-phase Non-Newtonian Liquid Gas Flow in the Vertical Pipe." *International Journal of Multiphase Flow*, 30, 551-563.
- Epstein, M. (1965). "Prediction of Liquid Hydrogen and Oxygen Pressurant Requirements." *Advances in Cryogenic Engineering*, 10, 219-233.
- Ferziger, J. H., and Peric, M. (1996). *Computational Methods for Fluid Dynamics*, Springer-Verlag, New York.
- Filina, N. N., and Weisend, J. G. (1996). *Cryogenic Two-phase Flow*, Cambridge University Press, New York.
- Francois, M. (2002). "Computations of Drop Dynamics with Heat Transfer," Doctoral Dissertation, University of Florida, Gainesville.
- Gebhart, B., Jaluria, Y., Mahajan, R. L., and Sammakia, B. (1988). *Buoyancy-induced Flow and Transport*, Hemisphere Publishing Company, New York.
- Ghia, U., Ghia, K. N., and Shin, C. T. (1982). "High-resolutions for Incompressible Flow Using the Navier- Stokes Equations and a Multigrid Method." *Journal of Computational Physics*, 48, 387-411.
- Graham, R. W., Hendricks, R. C., Hsu, Y. Y., and Friedman, R. (1961). "Experimental Heat Transfer and Pressure Drop of Film Boiling Liquid Hydrogen Flowing through A Heated Tube." *Advances in Cryogenic Engineering*, 6, 517-524.
- Graue, R., Krisson, M., Erdmann, M., and Reutlinger, A. (2000). "Integrated Health Monitoring Approach for Reusable Cryogenic Tank Structures." *Journal of Spacecraft and Rockets*, 37(5), 580-585.
- Gungor, K. E., and Winterton, R. H. S. (1986). "A General Correlation for Flow Boiling in Tubes and Annuli." *International Journal of Heat Mass Transfer*, 29(3), 351-358.
- Hammouda, N., Groeneveld, D. C., and Cheng, S. C. (1997). "Two-fluid Modeling of Inverted Annular Film Boiling." *International Journal of Heat and Mass Transfer*, 40(11), 2655-2670.
- Hands, B. A. (1986). *Cryogenic Engineering*, Academic Press, London.
- Harvey, J. F. (1974). *Theory and Design of Modern Pressure Vessels*, Van Nostrand Reinhold Company, New York.
- Heydenreich, R. (1998). "Cryotanks in Future Vehicles." *Cryogenics*, 38(1), 125-130.
- Hirt, C. W., and Nichols, B. D. (1981). "Volume of Fluid (VOF) Method for the Dynamics of Free Boundaries." *Journal of Computational Physics*, 39(1), 201-225.

- Ishii, M. (1975). *Thermo-fluid Dynamic Theory of Two-phase Flow*, Eyrolles, Paris.
- Ishii, M., and Jarlais, G. D. (1987). "Flow Visualization Study of Inverted Annular Flow of Post Dryout Heat Transfer Region." *Nuclear Engineering and Design*, 99, 187-199.
- Ishii, M., and Mishima, K. (1984). "Two-fluid Model and Hydrodynamic Constitutive Relations." *Nuclear Engineering and Design*, 82, 107-126.
- Janicot, A. J. P. (1988). "Experimental and Theoretical Studies of Gas-liquid Two Phase Flow at Reduced Gravity Conditions," Doctoral Dissertation, University of Houston, Houston.
- Jha, A. R. (2006). *Cryogenic Technology and Applications*, Elsevier Academic Press, Amsterdam.
- Juric, D., and Tryggvason, G. (1998). "Computations of Boiling Flows." *International Journal of Multiphase Flow*, 24(3), 387-410.
- Kamakoti, R. (2004). "Computational Aeroelasticity Using a Pressure-based Solver," Doctoral Dissertation, University of Florida, Gainesville.
- Khemis, O., Bessaih, R., Ali, M. A., and Francois, M. X. (2004). "Measurement of Heat Transfers in Cryogenic Tank with Several Configurations." *Applied Thermal Engineering*, 24, 2233-2241.
- Kim, J., and Moin, P. (1985). "Application of a Fractional Step Method to Incompressible Navier-Stokes Equations." *Journal of Computational Physics*, 59(2), 308-323.
- Lai, H., Yan, Y. Y., and Gentle, C. R. (2003). "Calculation Procedure for Conjugate Viscous Flows about and inside Single Bubbles." *Numerical Heat Transfer Part B*, 43(3), 241-265.
- Lai, H., Zhang, H., and Yan, Y. (2004). "Numerical Study of Heat and Mass Transfer in Rising Inert Bubbles Using a Conjugate Flow Model." *Numerical Heat Transfer Part A*, 46(1), 79-98.
- Lauder, B. E., and Spalding, D. B. (1974). "The Numerical Computation of Turbulent Flows." *Computer Methods in Applied Mechanics and Engineering*, 3, 269-289.
- Liao, J., Mei, R., and Klausner, J. F. (2006). "A Film Boiling Model for Cryogenic Chillover at Low Mass Flux inside a Horizontal Pipeline." *Heat and Mass Transfer*, 42(10), 891-900.
- Lörstad, D., and Fuchs, L. (2004). "High-order Surface Tension VOF-model for 3D Bubble Flows with High Density Ratio." *Journal of Computational Physics*, 200(1), 153-176.
- Mackenzie, J. A., and Robertson, M. L. (2000). "The Numerical Solution of One-dimensional Phase Change Problems Using an Adaptive Moving Mesh Method." *Journal of Computational Physics*, 161(2), 537-557.

- Mills, A. F. (1995). *Basic Heat and Mass Transfer*, Richard D. Irwin, New York.
- Mishima, K., and Hibiki, T. (1996). "Some Characteristics of Air-water Two-phase Flow in Small Diameter Vertical Tubes." *International Journal of Multiphase Flow*, 22(4), 703-712.
- Momenthy, A. M. (1964). "Propellant Tank Pressurization System Analysis." *Advances in Cryogenic Engineering*, 9, 273-283.
- Morgan, N. R. (2005). "A New Liquid-vapor Phase Transition Technique for the Level Set Method," Doctoral Dissertation, Georgia Institute of Technology, Atlanta.
- Mueller, P., and Durrant, T. (1999). "Cryogenic Propellant Liquefaction and Storage for a Precursor to a Human Mars Mission." *Cryogenics*, 39(12), 1021-1028.
- Nelson, R., and Unal, C. (1992). "A Phenomenological Model of the Thermal Hydraulics of Convective Boiling during the Quenching of Hot Rod Bundles, Part I: Thermal Hydraulic Model." *Nuclear Engineering and Design* 136(3), 277-298.
- Ni, M., Abdou, M., and Komori, S. (2003). "A Variable-Density Projection Method for Interfacial Flows." *Numerical Heat Transfer: Part B*, 44(6), 553-574.
- Nichols, B. D. (1971). "Recent Extensions to the Marker-and-cell Method for Incompressible Fluid Flows " *Lecture Notes in Physics*, 8, 371-376.
- Panzarella, C. H., and Kassemi, M. (2003). "Simulations of Zero Boil-off in a Cryogenic Storage Tank." *AIAA Paper*, 2003-1159.
- Peskin, C. S. (1977). "Numerical Analysis of Blood Flow in the Heart." *Journal of Computational Physics*, 25, 220-252.
- Pilliod, J. E., and Puckett, E. G. (2004). "Second-order Accurate Volume-of-fluid Algorithms for Tracking Material Interfaces." *Journal of Computational Physics*, 199(2), 465-502.
- Plachta, D. W., Christie, R. J., Jurns, J. M., and Kittel, P. (2006). "Passive ZBO Storage of Liquid Hydrogen and Liquid Oxygen Applied to Space Science Mission Concepts." *Cryogenics*, 46(2-3), 89-97.
- Popescu, M., Tai, C. F., and Shyy, W. (2006). "Cartesian Cut-cell Method with Local Grid Refinement for Wave Computations." *AIAA Paper*, 2006-2522.
- Qian, J., Tryggvason, G., and Law, C. K. (1998). "A Front Tracking Method for the Motion of Premixed Flames." *Journal of Computational Physics*, 144(1), 52-69.
- Raymond, F., and Rosant, J. M. (2000). "A Numerical and Experimental Study of the Terminal Velocity and Shape of Bubbles in Viscous Liquids." *Chemical Engineering Science*, 55(5), 943-955.

- Rezkallah, K. S. (1996). "Weber Number Based Flow-pattern Maps for Liquid-gas Flows at Microgravity." *International Journal of Multiphase Flow*, 22(6), 1265-1270.
- Rezkallah, K. S., and Zhao, L. (1995). "A Flow Pattern Map for Two-phase Liquid-gas Flows under Reduced Gravity Conditions." *Advances in Space Research*, 16(7), 133-136.
- Riede, P. M., and Wang, D. I. J. (1960). "Characteristics and Applications of Some Super-insulations." *Advances in Cryogenic Engineering*, 5, 209-215.
- Ryskin, G., and Leal, L. G. (1984). "Numerical Solution of Free-Boundary Problems in Fluid Mechanics. Part 2. Buoyancy-Driven Motion of a Gas Bubble through a Quiescent Liquid." *Journal of Fluid Mechanics*, 148, 19-35.
- Shin, S., and Juric, D. (2002). "Modeling Three-dimensional Multiphase Flow Using a Level Contour Reconstruction Method for Front Tracking without Connectivity." *Journal of Computational Physics*, 180(2), 427-470.
- Shyy, W., and Narayanan, R. (1999). *Fluid Dynamics at Interfaces* Cambridge University Press, New York.
- Shyy, W., Udaykumar, H. S., Rao, M. M., and Smith, R. W. (1996). *Computational Fluid Dynamics with Moving Boundaries*, Taylor & Francis, Washington, DC.
- Singh, R., and Shyy, W. (2007). "Three-dimensional Adaptive Cartesian Grid Method with Conservative Interface Restructuring and Reconstruction." *Journal of Computational Physics*, 224(1), 150-167.
- Singh, R. K., N'Dri, N. N., Uzgoren, E., Shyy, W., and Garbey, M. (2005). "Three-dimensional Adaptive Cartesian Grid Method for Multiphase Flow Computations." *43rd Aerospace Sciences Meeting & Exhibit*, Paper No. 2005-1389.
- Son, G. (2001). "A Numerical Method for Bubble Motion with Phase Change." *Numerical Heat Transfer, Part B*, 39(5), 509-523.
- Son, G. (2003). "Efficient Implementation of a Coupled Level-set and Volume-of-fluid Method for Three-dimensional Incompressible Two-phase Flows." *Numerical Heat Transfer: Part B*, 43(6), 549-565.
- Son, G., and Dhir, V. K. (1998). "Numerical Simulation of Film Boiling Near Critical Pressures With a Level Set Method." *Journal of Heat Transfer*, 120(1), 183-192.
- Steiner, D. (1986). "Heat Transfer During Flow Boiling of Cryogenic Fluids in Vertical and Horizontal Tubes Cryogenics." *Cryogenics*, 26, 309-318.
- Steward, W. G., R.V., S., and Brennan, J. A. (1970). "Cooldown Transients in Cryogenic Transfer Lines." *Advances in Cryogenic Engineering*, 15, 354-363.

- Sun, Y., and Beckermann, C. (2007). "Sharp Interface Tracking Using the Phase-field Equation." *Journal of Computational Physics*, 220(2), 626-653.
- Sussman, M. (2003). "A Second Order Coupled Level Set and Volume-of-fluid Method for Computing Growth and Collapse of Vapor Bubbles." *Journal of Computational Physics*, 187(1), 110-136.
- Sussman, M., Smereka, P., and Osher, S. (1994). "A Level Set Approach for Computing Solutions to Incompressible Two-phase Flow." *Journal of Computational Physics*, 114(1), 146-159.
- Tai, C. F., and Shyy, W. (2005). "Multigrid Computations and Conservation Law Treatment of a Sharp Interface Method." *Numerical Heat Transfer: Part B*, 48(5), 405-424.
- Tanguy, S., and Berlemont, A. (2005). "Application of a Level Set Method for Simulation of Droplet Collisions." *International Journal of Multiphase Flow*, 31(9), 1015-1035.
- Udaykumar, H. S., Kan, H.-C., Shyy, W., and Tran-Son-Tay, R. (1997). "Multiphase Dynamics in Arbitrary Geometries on Fixed Cartesian Grids." *Journal of Computational Physics*, 137(2), 366-405.
- Udaykumar, H. S., Mittal, R., Rampugoon, P., and Khanna, A. (2001). "A Sharp Interface Cartesian Grid Method for Simulating Flows with Complex Moving Boundaries." *Journal of Computational Physics*, 174(1), 345-380.
- Uzgoren, E., Singh, R., Sim, J., and Shyy, W. (2007). "Computational Modeling for Multiphase Flows with Spacecraft Application." *Progress in Aerospace Sciences*, 43(4-6), 138-192.
- Versteeg, H., and Malalasekera, W. (1995). *An Introduction to Computational Fluid Dynamics: The Finite Volume Method Approach* Essex.
- Welch, S. W. J., and Wilson, J. (2002). "A Volume of Fluid Based Method for Fluid Flows with Phase Change." *Journal of Computational Physics*, 160, 662-682.
- Whitaker, S. (1972). "Forced Convection Heat Transfer Correlations for Flow in Pipes, Past Flat Plates, Single Spheres, and for Flow in Packed Beds and Tube Bundles." *AIChE Journal*, 18, 361-371.
- White, F. M. (1991). *Viscous Fluid Flow*, McGraw-Hill, New York.
- Yadigaroglu, G. (1978). "The Reflooding Phase of the LOCA in PWRs. Part I: Core Heat Transfer and Fluid Flow." *Nuclear Safety*, 19(1), 20-36.
- Ye, T., Shyy, W., and Chung, J. N. (2001). "A Fixed-grid, Sharp-interface Method for Bubble Dynamics and Phase Change." *Journal of Computational Physics*, 174, 781-815.

- Ye, T., Shyy, W., Tai, C. F., and Chung, J. (2004). "Assessment of Sharp- and Continuous-Interface Methods for Drop in Static Equilibrium." *Computers and Fluids*, 33(7), 917-926.
- Yuan, K., Ji, Y., and Chung, J. N. (2007). "Cryogenic Chillover Process under Low Flow Rates." *International Journal of Heat and Mass Transfer*, 50, 4011-4022.
- Zang, Y., Street, R. L., and Koseff, J. R. (1994). "A Non-staggered Grid, Fractional Step Method for Time-dependent Incompressible Navier-Stokes Equations in Curvilinear Coordinates." *Journal of Computational Physics*, 114(1), 18-33.
- Zhang, J., Eckmann, D. M., and Ayyaswamy, P. S. (2006). "A Front Tracking Method for a Deformable Intravascular Bubble in a Tube with Soluble Surfactant Transport." *Journal of Computational Physics*, 214(1), 366-396.
- Zhao, L., and Rezkallah, K. S. (1993). "Gas-liquid flow Patterns at Microgravity." *International Journal of Multiphase Flow*, 19(5), 751-763.
- Zhao, L., and Rezkallah, K. S. (1995). "Pressure Drop in Gas-liquid Flow at Microgravity Conditions." *International Journal of Multiphase Flow*, 21(5), 837-849.

BIOGRAPHICAL SKETCH

Cheng-feng Tai was born in Changhua, Taiwan, in 1972. After receiving his Bachelor of Engineering degree in mechanical engineering from National Sun Yat-Sen University in 1995, he received the Master of Engineering degree from in aerospace engineering from National Cheng Kung University in 1997. From 2001 he has been pursuing his Ph.D. degree in aerospace engineering at the University of Florida. His current research interests lie in computational fluid dynamics of multiphase flows and heat transfer.